ABSTRACT

Title of Dissertation: RELATING VEHICLE SKID FRICTION TO PEDESTRIAN SLIP RESISTANCE ON PAVEMENTS WITH MACHINE LEARNING INTEGRATION AND MASTER CURVE DEVELOPMENT FOR DISTRESS PREDICTION

Osama Ali Barakat Aljarrah
Doctor of Philosophy, 2025

Dissertation Directed by: Associate Professor, Dimitrios Goulias
Department of Civil and Environmental Engineering

This dissertation addresses one of the main concerns in pavement engineering in regard to safety. Agencies need to relate vehicular skid resistance with pedestrian slip resistance on the pavement surfaces located at critical locations such as crosswalks. Thus, there was a critical need to examine and relate such parameters on typical marking materials by: conducting an extensive assessment at both lab and field conditions under alternative environmental and surface conditions; developing prediction models linking such parameters; and identifying friction specification revisions for acceptance, as well as routine condition evaluation recommendations.

To achieve these objectives, the research was organized into the following steps: lab and field experimentation; an extensive statistical analysis assessment between various parameters and testing conditions; an attempt to relate friction evaluation measurements to "ground-truth" conditions by incorporating image-based microtexture analysis; and development of machine

learning modeling.

The first study phase explored the friction assessment of widely used pavement marking materials in Maryland under various surface conditions, including dry (D), wet (W), and icy (I) surfaces. The British Pendulum Tester (BPT) was used to assess both laboratory and field performance in in-service conditions. Material-dependent variability and consistent trends between field and laboratory data were obtained, paving the way for the use of laboratory testing as an alternative to field inspection, which traditionally requires costly traffic control and is associated with significant safety concerns.

The second phase addresses the repeatability and reproducibility of BPT measurements across different devices and operators. Results confirmed that BPT provides consistent measurements for both tire skid and pedestrian slip resistance. Microscopic imaging and Fast Fourier Transform (FFT) analysis demonstrated how microtexture and macrotexture are affected by surface wear and material composition, and how these significantly influence friction levels.

The third phase considered the use of the Aggregate Image Measurement System (AIMS) to analyze pavement marking surface texture characteristics. Using asphalt cores with and without markings, surface condition texture parameters, such as root mean square (RMS), mean profile depth (MPD), and mean texture depth (MTD), were quantified across four scan directions. Directional sensitivity, regression among indices, quartile classification, and texture distribution analyses were performed. Results confirmed that AIMS-derived texture metrics align with BPN friction values and distinguish material performance.

The next phase considered the use of supervised machine learning to predict British Pendulum Numbers (BPN) based on a dataset of 1,092 laboratory and field data. Comparison of five ML models was examined, including Random Forest, XGBoost, Support Vector Regression,

Gaussian Process Regression, and Multilayer Perceptron. XGBoost yielded the best predictive performance with a coefficient of determination (R^2) of 0.951. Analysis of feature importance identified surface condition, material type, and test environment as the dominant predictors.

Since highway agencies have a multiyear set of data related to distress, the final portion of the study was focused beyond friction, in an effort to develop distress prediction models using the master Curve approach. Since the primary distresses governing pavement performance were identified to be fatigue cracking and permanent deformation (i.e., rutting), as documented by many Balanced Mix Design (BMD) studies currently under development in the US, data from the Long-Term Pavement Performance (LTPP) database were used with the "master curve" approach in developing such prediction models. Such modeling provided highly precise predictions and thus provided the means to identify future patterns of deterioration with reduced need for time-consuming and costly field surveys.

Finally, it is worth mentioning that the importance and value of relating vehicular skid friction to pedestrian slip resistance, and important findings, contributions, and value of this study in this area, addressing systematically and linking such critical parameters for safety, were recognized nationally with the AASHTO 2025 Sweet 16 High-Value Research Award.

RELATING VEHICLE SKID FRICTION TO PEDESTRIAN SLIP RESISTANCE ON PAVEMENTS WITH MACHINE LEARNING INTEGRATION AND MASTER CURVE DEVELOPMENT FOR DISTRESS PREDICTION

by

Osama Ali Barakat Aljarrah

Dissertation submitted to the Faculty of the Graduate School of the
University of Maryland, College Park in partial fulfillment
of the requirements for the degree of
Doctor of Philosophy
2025

Advisory Committee:
Professor Dimitrios G. Goulias, Chair/Advisor
Professor Ahmet H. Aydilek
Professor M. Sherif Aggour
Professor Paul Schonfeld
Professor Sung Lee, Dean's Representative

Preface

This dissertation is the original work of Osama Aljarrah. It was produced while pursuing a doctoral study at the University of Maryland from 2023 to 2026 under the supervision of Dr. Dimitrios Goulias.

The research focuses on the study *"Evaluating the Correlation between Slip Resistance and Skid Resistance of Pavement Markings at Crosswalks"*, supported by the Maryland Department of Transportation State Highway Administration (MDOT SHA). This experimental research included an assessment of alternative materials and testing conditions for pavement markings through lab and field testing. In conjunction with this, the research expanded into the development of *"Distress-Based Performance Prediction of Pavements and the Master Curve Approach"*, using data from the Long-Term Pavement Performance (LTPP) of the FHWA InfoPave database.

All endeavors are in accordance with the standards required in research within academic institutions. Collaborator contributions and source data acknowledgments are given throughout the dissertation.

Dedication

I dedicate this dissertation to my family, friends, and all who supported me, whether near or far, through physical presence or emotional support.

To my parents, whose love and encouragement gave me strength.

To everyone who stood by me with patience and belief throughout this journey.

Thank you for your support.

Acknowledgments

I would like to take this opportunity to thank my committee chair and advisor, Professor Dimitrios G. Goulias, for his invaluable guidance, support, and encouragement throughout my doctoral studies. His mentorship, technical insight, and dedication have had a tremendous impact on the direction and quality of this work.

I would like to express my gratitude to members of my advisory committee, Professor Ahmet H. Aydilek, Professor M. Sherif Aggour, Professor Paul Schonfeld, and Professor Sung Lee, for their time, helpful feedback, and support throughout the research journey.

I sincerely acknowledge the Maryland Department of Transportation State Highway Administration (MDOT SHA) for their generous support, both technical and financial, which made this research possible. I also appreciate the Federal Highway Administration (FHWA) and the Long-Term Pavement Performance (LTPP) program for allowing access to the InfoPave database.

Special thanks go to my research colleagues, lab members, and collaborators who provided technical assistance and helpful discussions in this work. I would particularly like to highlight the work of those who assisted in laboratory testing, data processing, and analysis.

I express my sincerest appreciation to my family for their unwavering support and understanding. I am especially grateful to my sister, Dr. Imteyaz Aljarrah, for her encouragement, inspiration, and constant support in this process. Her guidance and influence have been a source of strength.

Finally, I acknowledge all the individuals who have assisted this work in any manner, directly or indirectly. Your contributions are sincerely appreciated.

Table of Contents

List of Tables

List of Figures

List of Abbreviations

A	Asphalt
AC	Asphalt Thicknesses (mm)
AL	Alabama
A/M	ANOVA/MANOVA
APM	All Pavement Markings and Surface Conditions
AV%	Asphalt Air Voids (%)
AZ	Arizona
BPN	British Pendulum Number
BPN*	Average British Pendulum Number
BPN 1	British Pendulum Number for Unit 1
BPN 2	British Pendulum Number for Unit 2
BPN(TSR)	British Pendulum Number – Tire Slip Resistance
BT	Base Thicknesses (mm)
C	Concrete
Cg	Categorical
Cl	Clean
COND.	Surface Conditions
COF	Dynamic Friction Coefficient
CS1, P	Preformed Thermoplastic on Concrete Sample 1
CV%	Coefficient of Variability
CUM	Cumulative
Dates	Test Dates
DD	Aggregate Dry Density (kg/m^3)
Dev.	Testing Devices
Di	Dirt
D	Dry
DMA	Dense-Mix Asphalt
DIP	Digital Image Processing
Estar	Dynamic Modulus of Asphalt (MPa)

F	Field Testing
FC	Fatigue Cracking (m^2)
FFT	Fast Fourier Transform
FTIR	Fourier-Transform Infrared Spectroscopy
HC	Hydraulic Conductivity (cm/s)
I	Icy
L	Lab Testing
Loc.	Locations
MDD	Maximum Laboratory Dry Density (kg/m^3)
MC%	Moisture Content (%)
MR	Resilient Modulus (MPa)
N	Numerical
N200P%	No. 200 Sieve Passing (%)
NS	Not Statistically Significant
OTM%	Optimum Laboratory Moisture (%)
P	Preformed Thermoplastic
PA	Porous Asphalt
P0–P5	Slip resistance classifications based on AS 4586:2013
PC	Pervious Concrete
PCC	Portland Cement Concrete
PI%	Plasticity Index (%)
PSR	Pedestrian Slip Rubber
PT	Paired T-Test
PTV	Pendulum Test Value
Pt	Paint
RD	Average Rut Depth (mm)
Rep.	Replicates
RF	Random Forest
S	Sample Size (n)
SD	Standard Deviation
SG	Specific Gravity (unitless)

SN	Structural Number (unitless)
SS	Statistically Significant
T	High-Performance Tape
T/A/C	High-Performance Tape on Asphalt or Concrete
T, AS1	High-Performance Tape on Asphalt Sample 1
TC	Transverse Cracking (m)
Th	Thermoplastic
Th/A/C	Thermoplastic on Asphalt or Concrete
TSR	Tire Slip Rubber
TS, AS1	Thermoplastic on Asphalt Sample 1
W	Wet
WP	Wheel Path Length Cracked (m)
XRCT	X-ray Computed Tomography

Chapter 1: Introduction

1.1 Motivation and Background

The safety and functionality of transportation infrastructure, particularly roadways, depend heavily on the performance of pavement markings under a range of environmental and operational conditions [1]. Pavement markings play a critical role in friction-enhancing, thus traffic safety at crossings and reducing the likelihood of incidents with pedestrians as well as vehicle crashes [2, 3].

The frictional performance of pavement markings—especially under wet conditions—is a key factor influencing both vehicular skid friction and pedestrian slip resistance. Reduced surface friction can significantly increase the potential for accidents, particularly in areas where stopping distance is critical, such as pedestrian crossings. Harlow [4] emphasized that low skid resistance in wet conditions remains a persistent safety concern. To address this, state highway agencies have adopted in their specification and evaluation methods such as the British Pendulum Tester (BPT) to quantify surface friction. The BPT provides the British Pendulum Number (BPN), a standardized index used to assess the frictional characteristics of pavement surfaces [5].

Establishing appropriate minimum BPN thresholds is essential for ensuring safe pavement conditions. Nassiri [6] and others have recommended BPN-based acceptance criteria tailored to different roadway types. These recommendations, adapted from Asi [7], classify roadway sites into three categories based on geometry, traffic volume, and potential hazard level. Table 1.1

summarizes the recommended minimum BPN values for each category under wet conditions.

Table 1.1: Recommended Minimum BPN Values in Wet Testing Conditions [7].

Category	**Site Description**	**Minimum BPN**
A	Difficult sites including roundabouts, sharp bends (radius $\leq$ 150 m), steep gradients ($\geq$ 1 in 20 over 100 m), and approaches to traffic signals on unrestricted roads	65
B	Motorways, trunk roads, Class 1 roads, and heavily trafficked urban roads (more than 200 vehicles/day)	55
C	All other sites, including low-traffic and lower-risk areas	45

These guidelines emphasize the need for specifications that reflect the unique conditions and safety demands of each roadway category. However, despite widespread BPN testing, limited research exists on directly linking pedestrian slip resistance to vehicular skid friction across marking materials, surface types, and environmental conditions. There remains a need to evaluate and enhance pavement marking friction in real-world conditions, including wet, dry, and icy surfaces, and to ensure consistency between laboratory and field measurements. This gap forms one of the central motivations of this dissertation.

Beyond surface friction, a second major focus of this research involves the long-term performance prediction of asphalt pavements in terms of distress progression. Fatigue cracking and permanent deformation (i.e., rutting) are two of the key and most common distresses affecting asphalt roads. As pavement sections deteriorate over time, the ability to predict distress evolution becomes critical for effective maintenance planning and asset management. This dissertation explored the development of master curve models based on Long-Term Pavement Performance (LTPP) data to predict these distresses for similar pavement types. The models aim to improve prediction accuracy by incorporating material and climatic properties, thereby offering state high-

way agencies a practical tool for forecasting pavement condition with reduced dependence on frequent field surveys.

Together, these two focus areas—(1) enhancing understanding of pavement marking friction in regards to vehicles and pedestrians, and (2) modeling asphalt pavement distress predictions through master curves—form the foundation for this dissertation.

1.2 Research Objectives

This dissertation is structured around two primary research objectives, each one addressing a critical aspect of pavement safety and/or performance prediction:

1. **Evaluation of Pavement Markings Friction:** To assess the frictional performance of alternative pavement marking materials under diverse surface and environmental conditions, with an emphasis on both vehicular skid friction and pedestrian slip resistance. The achieve this objective, the following tasks were considered:

    - Laboratory and field testing using the British Pendulum Tester (BPT) to measure British Pendulum Number (BPN).
    - Investigation of the repeatability and reproducibility of BPT measurements across different operators, materials, and conditions.
    - Comparative analysis of marking materials (e.g., preformed thermoplastic, thermoplastic, tape, paint) across asphalt and concrete samples.
    - Integration of microscopic imaging such as the Aggregate Image Measurement System (AIMS) and frequency-domain surface analysis (FFT) to understand micro- and macrotexture contributions to friction.

- Development of predictive models using supervised machine learning techniques to estimate frictional performance based on material, environmental, and surface parameters.

2. **Master Curve Modeling for Pavement Distress Prediction:** To develop a systematic modeling approach for developing pavement distress prediction models using the national Long-Term Pavement Performance (LTPP) database. To achieve this objective the following steps were considered:

   - Modeling of the distress-based "master curves" function for different distress data types, (i.e., fatigue cracking and permanent deformation).
   - Development of transfer shift functions with key pavement material and structural design parameters for curve fitting of alternative pavement sections and distresses.

1.3 Organization of the Dissertation

This dissertation is structured into the following chapters to address the overall research objectives.

Chapter 1 introduces the study by outlining the motivation behind the work, the background context related to pavement markings and friction, the research objectives, and the overall structure of the dissertation. It frames the research problem in terms of safety concerns for both pedestrians and vehicles, friction, and highlights the need for improved assessment methods as well as predictive tools.

Chapter 2 presents a detailed investigation into the relationship between vehicular skid and pedestrian slip resistance on pavement markings. Using the British Pendulum Tester (BPT), both

laboratory and field evaluations are described on multiple marking types and surface conditions. The results present how various factors, such as moisture, surface type, and material, affect friction. Suggested correlations between pedestrian and vehicular measurements are described as well.

Chapter 3 focuses on a round robin assessment of BPT repeatability and reproducibility. Alternative BPT units and operators were examined to evaluate measurement consistency across devices used by contractors and agencies. In addition to mechanical testing, microscopic imaging and frequency-based texture analyses used to investigate surface texture and bead loss are described. These tests offered insights into long-term performance and wear, contributing to reliability assessments of BPT in real-world scenarios.

Chapter 4 introduces the Aggregate Image Measurement System (AIMS) analysis for pavement markings. In detail, the imaging setup and signal processing used to quantify microtexture on asphalt cores with and without markings, defined RMS, MPD, and MTD metrics, and texture comparison across materials (AS#2, TS#2, ThS#2, and PS#2) are presented. The chapter presents directional sensitivity results and links AIMS-derived texture to BPN friction trends. Statistical comparisons among texture indices are presented.

Chapter 5 presents the supervised machine learning modeling techniques used to predict the friction performance of pavement markings. The results of the five models developed and tested on a large dataset (n=1,092) are presented, incorporating marking types, surface conditions, temperature, and test environments. Feature importance, model accuracy, and distributional diagnostics were conducted. The findings confirmed that machine learning can reliably predict BPN values and help optimize material selection and safety outcomes.

Chapter 6 presents the performance modeling approach for developing master curve func-

tions for predicting pavement distress progression using the LTPP field data. Two primary distresses were studied—fatigue cracking and permanent deformation—using sections from Alabama and Arizona. Master curve development and the use of shift factors allowing generalizable predictions across similar pavement types and climatic conditions are presented.

Chapter 7 provides a summary of the study conclusions with a synthesis of key findings, practical implications, and recommendations. Emphasis is placed on improving material specifications, enhancing monitoring protocols, and expanding friction research using both experimental and predictive approaches. Suggestions for future work are included in regards to further model development, integration with traffic simulation, and broader field implementation.

A chart of the dissertation's chapters and tasks are presented in Figure 1.1.

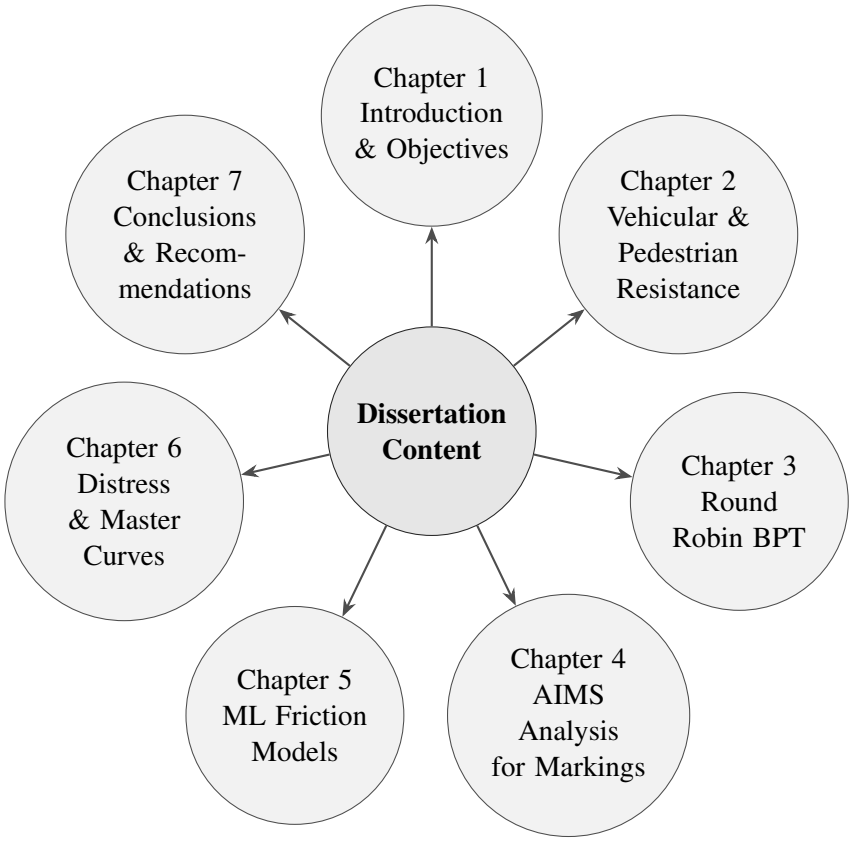

Figure 1.1: Radial Flowchart Depicting the Organization of Dissertation Content

Chapter 2: Relating Vehicular Skid and Pedestrian Slip Resistance at Pavement Crossings

2.1 Overview

Pavement friction at crossings in regard to safety involves interaction between pedestrians and vehicles [8]. Past studies have primarily focused on vehicular friction of pavements at crossings, and thus there is a need to fill the gaps in relating to pedestrian slip resistance [9, 10]. This study aimed to assess friction at pavements with crosswalk markings for both pedestrians and vehicles. While vehicular skid resistance is a very well-researched area, pedestrian slip resistance at crossings, and in particular as influenced by pavement marking materials, is understudied. There are very limited studies that have systematically examined such friction relationships for various pavement surfaces with marking materials and diverse environmental conditions. Furthermore, previous research often narrowly focuses on individual aspects, leaving critical gaps in understanding the collective impact of various pavement materials, pedestrian footwear, versus vehicular tire friction.

The motivation for this research lies in the absence of comprehensive test requirements or routines that consider pedestrian as well as vehicle friction at crosswalks at the same time. Current specifications typically address vehicular skid resistance only through BPN thresholds. By evaluating the simultaneous performance of pedestrian slip as well as vehicular skid resistance the same pavement markings, this work introduces a more integral approach to crosswalk safety

evaluation.

While several devices exist to quantify slip and skid resistance, including the Dynamic Friction Tester (DFT), Sideway-force Coefficient Routine Investigation Machine (SCRIM), and the T2GO skiddometer, such devices are often constrained by operational complexity, speed limitations, or lack of suitability for small test areas such as pedestrian crossings. A comparative summary of their weaknesses and strengths is outlined in Table 2.1 to put into perspective the selection of the most appropriate tool for this study. From this comparison and considering current field practice, the BPT was selected on the basis of low cost, portability, ease of use, and broad acceptance in agency specifications. The BPT has seen historical use in laboratory and field applications and thus is a viable choice for the measurement of friction in crosswalk applications. The BPT also coincidentally is the current standard for pavement marking acceptance in Maryland, which further validates the selection. Since most of the current acceptance specifications for pavement marking are based on the BPT, and this is the case for Maryland, the study was focused on such evaluation methods at both laboratory and field conditions.

In order to address the identified research gap, the current study introduces the following contributions: (i) a dual evaluation of skid and slip resistance on three pavement marking types; (ii) accounting for freeze–thaw testing protocols to mimic ice, which is rarely implemented in BPT studies; (iii) analysis of traffic wear effects based on comparison of wheel path and non-wheel path regions; and (iv) construction of a correlation model between laboratory and field tests results to support cost savings in safety evaluations.

In addition to friction, pavement markings at crosswalks have a broader role in safety [11]. This includes, among others, a vital role in enhancing visibility and providing clear guidance for both pedestrians' and drivers' behavior [12]. Nevertheless, road accidents have been linked

to a great extent to skid resistance [13]. The importance of slip and skid resistance becomes especially critical in adverse meteorological conditions, where wet or icy surfaces heighten the risk of accidents [14]. Thus, the primary aim of this experimental study was to assess the friction of pavement markings at crosswalks with regard to:

1. Quantifying pedestrian slips at crosswalks on specific pavement markings used in Maryland;

2. Evaluating vehicle friction on crosswalk pavement markings of interest and at the same locations as the pedestrian slip assessment;

3. Assessing the impact of varying environmental conditions on pedestrian and vehicle friction at crosswalk markings. This aspect takes into account factors such as dry, wet, and icy surfaces, aiming to provide a link between friction with such diverse meteorological conditions;

4. Relating laboratory and field-testing results to minimize the need for periodic field assessment thus reducing field exploration costs and minimizing monitoring crew's exposure to traffic;

5. Identifying potential recommendations on revising acceptance specifications for such crossing materials by considering both pedestrian and vehicle friction.

Table 2.1: Summary of Slip and Skid Resistance Testers.

Device	Test Principle	Advantages and Limitations	Typical Use Cases and References
BPT	Measures energy loss of a pendulum with rubber slider across dry/wet surfaces; outputs British Pendulum Number (BPN)	Portable, low-cost, no power needed, widely used (ASTM E303); Capable of measuring directional friction; suitable for lab/field since the 1950s. Stationary; low-speed test; Not suitable for network-level skid resistance monitoring.	Skid resistance, aggregate polishing, *microtexture*, COF estimate. [15]
DFT	Measures dynamic friction via decelerating of three rubber sliders from 80–0 km/h on wetted surface using a rotating disk system; outputs friction vs. speed curve (ASTM E1911)	Simulates high-speed skid behavior; accounts for water film; good for speed-dependent analysis. Requires power and setup; sensitive to surface texture and wetting; complex structure and cost.	Speed-based friction profiling; surface–water sensitivity; FE & tribology modeling; 3D texture data integration. [16]
SFC (SCRIM device)	Measures lateral force at 20° slip angle using a smooth tire on a wetted surface while vehicle moves at 30–80 km/h; outputs lateral Force Coefficient	Continuous testing at traffic speeds; strong link to crash risk; widely used for network level surveys. Requires test vehicle; Results sensitive to vehicle speed, tire brand and wear, water film thickness, and driving trajectory; requires tire calibration and replacement after 3 mm wear.	Field evaluation of anti-skid performance and friction variability under operational conditions. [17]
T2GO	Hand-pushed *skiddometer* that measures longitudinal friction at a fixed 20% slip ratio using dual wheels and a belt system; operates at walking speeds (∼2.5–4.0 km/h) on dry and wet surfaces	Portable; immediate measurement start; no run-up distance needed; usable in confined or unsafe areas; GPS, temp, and humidity sensors integrated. Limited to walking speed; not suitable for network-level surveys; friction readings influenced by surface roughness and V-belt tension.	Evaluation of longitudinal skid resistance; friction testing in inaccessible or accident zones. [18]

Note: BPT = British Pendulum Tester; DFT = Dynamic Friction Tester; SFC = Side-Way Force Coefficient; SCRIM = Sideway-force Coefficient Routine Investigation Machine; T2GO = Portable low-speed *skiddometer*; COF = Coefficient of Friction; FE = Finite Element.

2.2 Literature Review

2.2.1 Pavement Friction and Alternative Materials

Several studies on pavement friction have predominantly focused on conventional pavement materials like concrete and asphalt and to a lesser degree on pavement markings such as

high-friction coatings, thermoplastic markings, and paint materials. Early investigations have looked at slip resistance predominantly centered on laboratory-based testing and employing devices such as the BPT and the portable skid resistance tester, PSRT, [19, 20]. While these studies focused on surface texture, microtexture, and macrotexture in determining slip resistance, were limited in assessing alternative pavement materials such as pavement markings. Purohit et al. [21] and Nassiri [6] examined the slip resistance of thermoplastic markings, comparing them to traditional road materials. Results indicated that, despite compositional differences, well-designed and maintained thermoplastic materials could furnish adequate slip resistance. A more recent study assessed floor slip resistance using the BPT [22]. Another study simulated pedestrian gait on various surfaces and assessed the surface friction properties [23]. Recent studies have also explored factors impacting slip resistance, such as driving conditions and asphalt pavement types. Fan [24] demonstrated that the type of asphalt pavement and driving patterns significantly influence the road surface's ability to resist slipping.

2.2.2 Skid Resistance Testing and Applications

Over time, several studies have used the BPT for the assessment of skid resistance [25, 26]. The importance of alternative pavement markings such as high-friction coatings, thermoplastics, and composite materials on road safety has been recognized in Europe as well [10]. The correlation between the BPN and pavement friction has been a focal point of friction studies. Research by Brassard et al. [27] provided a good relationship between BPN values and the coefficient of friction. Thus, with an interest in alternative pavement markings, researchers have focused on assessing their impact on skid resistance. A study by Bao et al. [10] reviewed the skid resistance

of diverse alternative pavement marking materials, revealing that certain materials can furnish satisfactory skid resistance. However, judicious selection and regular maintenance emerge as pivotal factors in ensuring pedestrian safety. Environmental variables and surface conditions, including moisture and the presence of debris, yielded a substantial influence on skid resistance. Kumar and Gupta [28] evaluated factors affecting skid resistance at the tire-pavement interface under varying conditions, emphasizing the imperative of continual maintenance to uphold skid resistance amidst changing environmental conditions.

2.2.3 Specifications for Pedestrian and Vehicular Safety

Recent studies incorporate a synergistic blend of field evaluations and laboratory testing to gauge skid resistance. Instruments such as the BPT and the dynamic friction tester, DFT, have been deployed for field measurements [29], while laboratory experimentation involves tribometer measurements and assessments of material properties [30]. Effects of routine maintenance, including cleaning and retexturing have been looked at as well [31].

As mentioned previously, the majority of state acceptance specifications for pavement markings focus on a minimum BPN concerning vehicle skid resistance. Thus the aim is to consider a minimum slip resistance in regards to pedestrian safety at crossings. The Maryland State Highway Administration (SHA) Manual of Standard Specifications for Construction and Materials [32] delineates guidelines for materials and surfaces. Notably, crosswalks are recommended to possess a minimum initial BPN of 45.

Numerous U.S. state DOTs have formulated their unique specifications regarding slip resistance at pedestrian crossings. For instance, while Caltrans does not prescribe BPN in its spec-

ifications, the practice of acknowledging a BPN of 45 as the minimum for all mixture types is widely accepted. Furthermore, Caltrans considers BPN above 55 as adequate and above 65 as exemplary [33], while the New York State Department of Transportation (NYSDOT) underscores the use of high-friction surface treatments (HFST) to augment pedestrian safety [34].

Internationally, various countries have revised their standards for slip resistance at pedestrian crossings. In the United Kingdom, the independent authority provides guidance on slip resistance standards, emphasizing a minimum pendulum test value, PTV, of 36 units [35]. In Italy, skid resistance tester (SRT) measurements of pavement markings were found to vary between 41 and 55 [10].

2.2.4 Technologies for Measuring Slip Resistance

In terms of the most common approach for prescribing friction evaluation for slip resistance at pedestrian crossings, a minimum BPN threshold value of 45 has been suggested. Nevertheless, in recent years alternative methodologies for measuring slip resistance have been proposed. These include:

1. **Tribometers:** Devices directly assessing the frictional properties of a surface, such as the Tortus and Portable Skid Resistance Tester, PSRT. Marletta [36] study attests to the accuracy of tribometers in evaluating floor slipperiness and gauging the pedestrian's risk of sliding;

2. **Texture Depth Measurement:** This method evaluates the microtexture of a surface, integral to slip resistance, using instruments like the Circular Track Meter (CTM).

3. **Dynamic Friction Tester, DFT:** Simulating a vehicle tire's interaction with the road. It

measures the friction coefficient of a pavement surface.

4. **3D Surface Profilometry:** This technology furnishes detailed 3D surface maps, enabling a comprehensive assessment of surface texture and potential slipperiness.

5. **The Portable Slip Simulator:** A research endeavor determined the utility of a portable slip simulator in assessing sidewalk slipperiness under diverse weather conditions and evaluating various types of footwear for resistance to slippage [37].

2.2.5 Pavement Marking Materials

Thermoplastic pavement marking materials have been used to a great extent in highways in the United States due to their service life of three to five years, which is long and cost-effective, besides being durable. These materials provide superior visibility, retroreflectivity, and adaptability to all-weather conditions when applied in liquid form using spraying or extrusion techniques. Extrusion is slower but can accommodate thicker markings while spraying is quicker but only works with thinner layers. Thermoplastics, through thermal bonding, are strongly adhered to HMA. Thermoplastics have only a mechanical bond with PCC. Thermoplastic is less appropriate for PCC compared with HMA because this mechanical bonding is rather weak. Due to these setbacks, thermoplastics, though resilient and able to work in most environments, remain a reliable choice for traffic delineation [38–40].

Preformed thermoplastic markings are durable, anti-skid, retroreflective materials used for several applications: roadways, intersections, bike paths, and airports. They consist of thermoplastic with glass beads and other abrasives embedded in them that make them resistant to fuels, oils, and lubricants. The material deforms to conform to pavement contours and reseals upon

reheating, allowing an efficient application by the use of a propane torch, and there are no temperature restrictions against the use. The material meets AASHTO M249 and has a minimum of 30% intermixed glass beads for high retroreflectivity. Adequate surface preparation is required to achieve good bonding. In concrete, a primer coat is desirable. The preformed thermoplastic markings are manufactured in several thicknesses, colors, and configurations; have excellent retroreflectivity; and show long service life, even under high traffic volumes [41].

Preformed tape refers to a urethane or pliable polymer film embedded with glass beads for an enhancement of retroreflectivity and skid resistance. This product comes in continuous roll material that can also be cut into a wide variety of shapes and symbols. It is easy to handle, flexible, and does not require expensive equipment or skilled labor. Since the material used here is very durable, marking has to be done very frequently in places that have heavy traffic, making it moderately expensive. Its application, however, is slower and more expensive compared to other methods. The pre-fabricated tapes are of two types: permanent and temporary. Bonding and surface cleanliness are very important. The specification number and material differ. Application methods differ, too, such as overlay on an existing asphalt surface or inlay of new asphalt. Although more expensive, tapes perform well under adverse conditions and require less equipment, they can be used for a minimal number of markings. Temperature limitations and minimum thickness determined by state-specific application rules further emphasize proper installation for optimal performance [38, 42, 43].

2.2.6 Mechanistic Insights into Tire-Pavement Friction

Pavement friction is largely determined by two primary mechanisms: adhesion (A) and hysteresis (H). Adhesion results from molecular bonding at high-pressure contact points due to surface irregularities, while hysteresis involves energy loss as tire rubber adapts to features such as ridges and depressions [44, 45]. Therefore, friction can be considered as the combination of adhesion, F_A, and hysteresis, F_H, forces (all in newtons, N), Equation 2.1. Additionally, minor contributors to friction include effects from rubber wear and micro-hysteresis, as distinct from bulk hysteresis. Research over the past decade has confirmed that rubber wear can contribute to cohesion loss as part of the overall frictional force [44].

$$F = F_A + F_H \tag{2.1}$$

In transport engineering, the concept of friction specifically relates to tire-pavement interaction. This friction arises from two distinct surface texture characteristics: microtexture and macrotexture. These terms are traditionally classified based on texture wavelength (λ_w) and vertical dimension (A), both typically measured in millimeters (mm), as shown in Table 2.2 [46]. Different fields approach texture and friction with varying focuses; for instance, mechanical engineering often examines friction with machinery and lubricants, whereas transportation infrastructure engineering centers on the tire-pavement interface and traffic safety considerations.

Pavement friction is described as "the force that resists the relative motion between a vehicle tire and a pavement surface" [45]. This resistance is typically measured using a dimensionless value called the coefficient of friction (μ), which characterizes tire-pavement friction.

The friction coefficient is calculated as the ratio between the tangential friction force, F (N), at the tire-pavement contact point and the normal force, F_w (N), acting on the wheel. The friction coefficient (μ) is dimensionless (unitless) and can be expressed as follows [29]:

$$\mu = \frac{F}{F_w} \tag{2.2}$$

Table 2.2: Texture scales [46].

Scale	**Limits**
Microtexture	$\lambda_w < 0.5$ mm $\quad (A < 0.5$ mm)
Macrotexture	$0.5 < \lambda_w < 50$ mm $\quad (0.1 < A < 20$ mm)
Megatexture	$50 < \lambda_w < 500$ mm $\quad (0.1 < A < 50$ mm)
Unevenness	$500 < \lambda_w < 50$ m

2.2.7 Energy Absorption and Dynamic Surface Friction

The British Pendulum Tester (BPT) measures the dynamic surface friction by assessing the pendulum's energy loss in its swing, that is, the work done by the pendulum against friction produced between the slider and test surface. This energy loss indicates the kinetic energy that is dissipated because of frictional forces [47]. Work done against friction is given as:

$$WD = \mu PD \tag{2.3}$$

Where: WD is the work done against friction (J), μ is the effective coefficient of friction between the slider and the surface (unitless), P is the average normal load between the slider and surface (N), and D is the sliding distance over the test surface (m).

At the same time, the loss in energy of the pendulum arm during its interaction with the surface can be expressed as:

$$EL = W(H - h) \tag{2.4}$$

Where: EL is the loss in energy of the pendulum arm (J), W represents the effective weight of the swinging arm (N), H is the initial height of the center of gravity of the pendulum in its release position (m), and h is the height of the center of gravity at the highest point reached after the slider has contacted the test surface (m).

By equating the energy loss in the pendulum arm to the work against friction, the effective friction coefficient μ is expressed as:

$$BPN = 100\mu_e = 100 \cdot \frac{W(H - h)}{DP} \tag{2.5}$$

Therefore, the coefficient of friction μ can be calculated based on the mechanical properties of the pendulum and testing parameters, along with the height difference $H - h$ reflecting the energy absorbed by the surface friction. In this context, μ_e is the friction coefficient. The value of P depends on the unique force-deflection curve of each BPT slider, which means different BPT devices may yield different measurements for identical surfaces. The slider's rubber is characterized as hyperelastic, with its elastic modulus calculated based on hardness, as presented in Equation 2.6 [47]:

$$\log_{10} E = 0.0198H_r - 0.5432 \tag{2.6}$$

Where: E is measured in MPa, and H_r represents the International Rubber Hardness (IRHD, unitless) of the slider rubber.

According to [47, 48], the IRHD for BPT rubber sliders used in pedestrian slip resistance testing typically ranges from 94 to 98 and 55 to 61 for skid pads (see Table 2.3).

The IRHD difference is required to distinguish between the material properties of shoe soles and tire rubber, with Slider 96 (94–98 IRHD) simulating the harder shoe soles and Slider 57 (55–61 IRHD) simulating the softer, more deformable tire rubber. Slider 57 and Slider 96 are selected based on rubber hardness. Resilience is measured by using the Lüpke Rebound Hammer in accordance with ISO 4662 [49], which measures rebound resilience by comparing the energy of a pendulum before and after striking a flat rubber surface.

The hardness of the rubber pad itself is prescribed by IRHD according to ISO 48 [50] through four methods: Normal (N), High-hardness (H), Low-hardness (L), and Microtest (M). Method N is applied to test pieces thicker than 4 mm, and Method M to those thinner than 4 mm; both cover a preferred IRHD range of 35 to 85, extendable to 30 to 95. Additional hardness testing is to ISO 48-5 (IRHD pocket meter method) [51], but this is for control purposes only, not for specification. It requires test specimens with at least 6 mm thickness or layers of a flat surface with at least 12 mm separation from edges. The hardness of the complete slider, including rubber bonded on aluminum, is defined by the Shore hardness method by SR ISO 48-4 [52], generally using the A scale for standard rubber. The test pieces should have a minimum thickness of 6 mm for the A, D, and AO types and a minimum of 1.5 mm for scale AM, with flat surfaces and a suitable size so that edge effects are not created.

Table 2.3: Properties of Sliders 57 and 96 Across Temperatures [48].

Temperature (°C)	**Resilience (%)** Slider 57	**Resilience (%)** Slider 96	**Hardness (IRHD)** Slider 57	**Hardness (IRHD)** Slider 96
0	43 to 49	–	55 to 61	94 to 98
5	–	19 to 23		
10	58 to 65	–		
23	66 to 73	21 to 26		
30	71 to 77	–		
40	74 to 79	26 to 30		

2.3 Experimental Testing and Analysis

To achieve the objectives of this study, the steps in Figure 2.1 were undertaken and described next. During the scoping phase, the need to incorporate both laboratory and field testing was identified to assess the impact of the various conditions (i.e., dry, wet, icy) on pavement markings friction as well as relate the results. In the process of identifying the specifics of testing, a thorough literature review was conducted of skid and slip resistance, particularly focused on pavement markings.

Next, based on the most common pavement markings used at crosswalks in the state, the specific materials and types were selected for inclusion in the study. Based on guidance from state engineers and since the Maryland acceptance specification is based on the BPT, this was selected as the testing protocol for both laboratory and field testing.

The extent of the laboratory and field testing was then identified to include typical pavement marking materials used in Maryland, and include testing conditions of interest representing both environmental-related parameters (dry, wet, and/or icy) for the lab assessment. Specific field sites were included in the study to assess the effect of concentrated traffic on wheel paths versus

adjacent locations and/or shoulders experiencing lower traffic levels and thus wear and tear.

The testing results were then analyzed both numerically and statistically to assess slip and skid resistance at specific pavement markings, testing conditions, and field locations, determine testing repeatability in regard to Quality Assurance and acceptance, and document the significance of the observed effects. Based on the results and analysis, the findings were used to provide recommendations pertinent to pavement marking materials, slip and skid friction testing, and the potential inclusion of slip resistance requirements in the state acceptance specification for these materials. Further details of some of these steps are described next and in the analysis section.

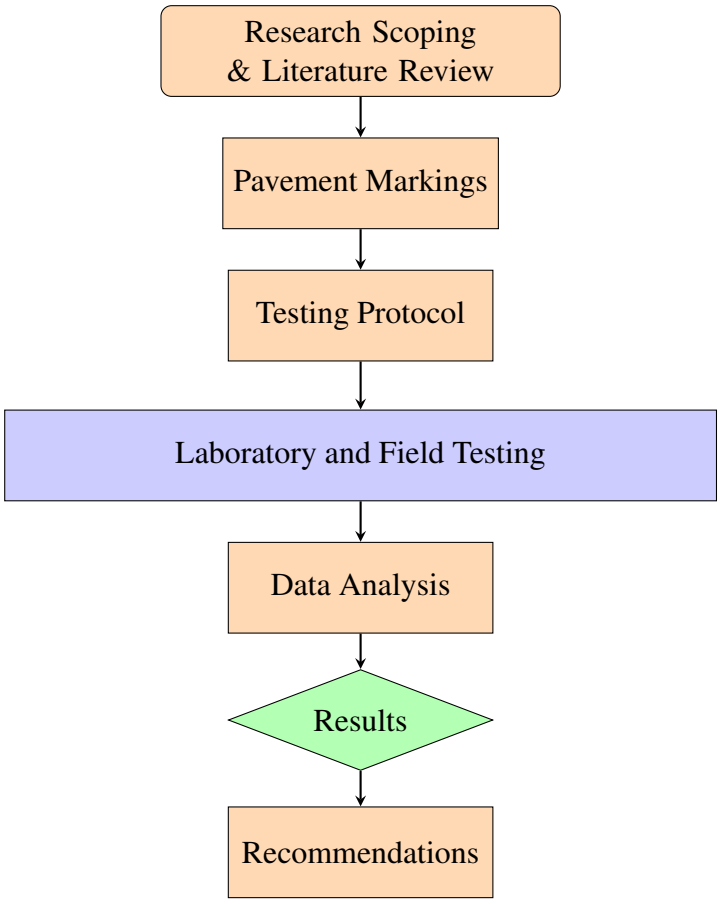

Figure 2.1: Methodological Framework of Testing and Analysis

2.3.1 Selection of Pavement Markings and Specimen Preparation

As mentioned earlier, it was the objective of this study to select representative pavement markings for inclusion in the study from those typical types used in Maryland. The agency is transitioning to the exclusive use of preformed thermoplastic (P) pavement markings for all state projects; however, it is pertinent to incorporate an evaluation of all other significant types utilized so far, including high-performance tape (T) and thermoplastic (Th), in both laboratory and field testing.

The field testing sites were chosen in collaboration with state engineers, necessitating traffic control and safety considerations during testing. In contrast, the laboratory experiments focused on samples of pavement marking materials applied to both concrete and asphalt surfaces to draw pertinent conclusions. Consequently, this research employed both concrete and asphalt samples that represent the mixtures applied in the state.

The concrete samples were beams of 53.3×15.2×15.2 cm (21×6×6 in), while the asphalt samples were gyratory compacted samples of 15.2×6.2 cm (6×2.4 in). Each marking type was assigned to a different beam. The 6-inch depth ensured proper alignment with the BPT resting beam for testing. Concrete cylinders (6×6×12 inches) were not used since their height exceeded the BPT adjustment range. In the case of cylindrical asphalt samples, particular care was taken to position and stabilize the BPT slider to provide adequate contact with the small surface area.

The application of P marking requires the use of a propane torch to be applied on asphalt samples, following the supplier's recommendations (see Figure 2.2). Figure 2.3 presents the three types of pavement markings considered in the study (Th, P, and T) and applied on both asphalt and concrete surfaces as per supplier recommendations.

Figure 2.2: Application of Preformed Thermoplastic on asphalt surfaces

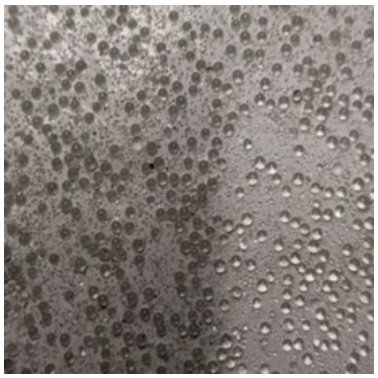

(a) Preformed Thermoplastic

(b) Thermoplastic

(c) High-Performance Tape

(d) BPT Instrumentation

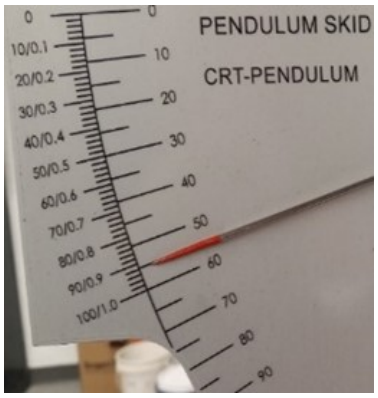

(e) BPN Value Illustration

Figure 2.3: Pavement Marking Types and British Pendulum Tester (BPT) Setup. Subfigures (a)–(c) show the tested materials, and (d)–(e) illustrate the BPT instrumentation and output.

2.3.2 BPT Testing Protocol

The BPT was used for the laboratory and field testing. Both pedestrian slip and vehicle skid resistance were evaluated using the specific pads provided by the BPT manufacturer. In the first case, the pad is made of representative material reflecting pedestrian shoe rubber sole (i.e., pedestrian slip rubber, PSR), while in the latter case represents tire rubber (tire slip rubber, TSR). In the lab, the friction was measured in dry (D), wet (W), and icy (I) surface conditions on all samples, while the field testing included dry and wet conditions for safety concerns.

The assessment of the frictional properties of each specimen adhered to the guidelines set forth by ASTM E303, employing the BPT as shown in Figure 2.3. The resulting values represent the frictional resistance BPN (British Pendulum Number) as recorded by BPT and depicted in Figure 2.3(d). The BPT apparatus includes a pendulum arm characterized by a swinging motion that interfaces with the surface of the specimen. The contact of the pad with the sample surface during the oscillation of the pendulum arm yields a quantifiable BPN value, related to the surface's inherent resistance to friction. The alternative pads are positioned at the nadir of the pendulum arm with the rubber slider (PSR or TSR) securely affixed.

In terms of environmental conditions (i.e., surface wet, dry, icy), the dry conditions reflect the specification requirement for testing. Before experimentation under dry conditions, the laboratory specimens, along with the field sites, were allowed to stay in completely dry conditions for 24 hours. In the wet (W) surface conditions, the specimens and/or field site location underwent spraying of water to emulate the presence of moisture on the surface. The degree of moisture exposure followed the state engineer's recommendation and past studies' practice [6]. To simulate the icy (I) conditions in the lab, past studies' recommendations were used as well [6]. In

this regard, a freeze-thaw chamber was employed. The specimens with the pavement markings were placed in a water reservoir at a temperature of 14°F ($-10\,^{\circ}$C) for two hours. Following this exposure, specimens were submerged in water at room temperature for five minutes before being carefully extracted from the water tank. The thaw interval was included to simulate in-service freeze-thaw cycles, which impact ice crystal formation and surface performance. A subsequent 30-minute interval within the chamber facilitated the intentional formation of ice crystals on specimen surfaces. At this juncture, the surfaces of the specimens underwent testing with the BPT apparatus.

2.3.3 Analysis Methods

In addition to the numerical assessment of the results, statistical analysis was used to assess the impact and significance of the various parameters on slip and skid resistance as well as to develop statistically meaningful relationships between them. In this regard, Analysis of Variance (ANOVA) and Multivariate Analysis of Variance (MANOVA) were used along with paired t-tests.

2.4 Factors Included In The Skid And Slip Resistance Experimentation

In this study, a variety of parameters and conditions affecting skid and slip resistance were considered and presented in Figure 2.4. In summary, these included the combined effects of the following:

- Marking Materials (P, Th, and T)
- Surface Conditions (D, W, and I)

- Vehicular Traffic Impact (in-wheel path, WP, versus off-the-wheel path, NWP)
- Laboratory versus Field Testing
- Marking Materials on Asphalt versus Concrete Surfaces

In regard to the presence of higher vehicular traffic on pavement markings, it is anticipated that increased wear and tear will lead to greater degradation of slip and skid resistance over time. Such an aspect was of interest to the research to assess meaningful conclusions on the longevity of these materials in terms of surface friction with traffic. Laboratory testing provides an assessment of the performance (i.e., surface friction) of these materials under controlled conditions, while field testing involves additional uncontrolled factors such as environmental factors and traffic dynamics.

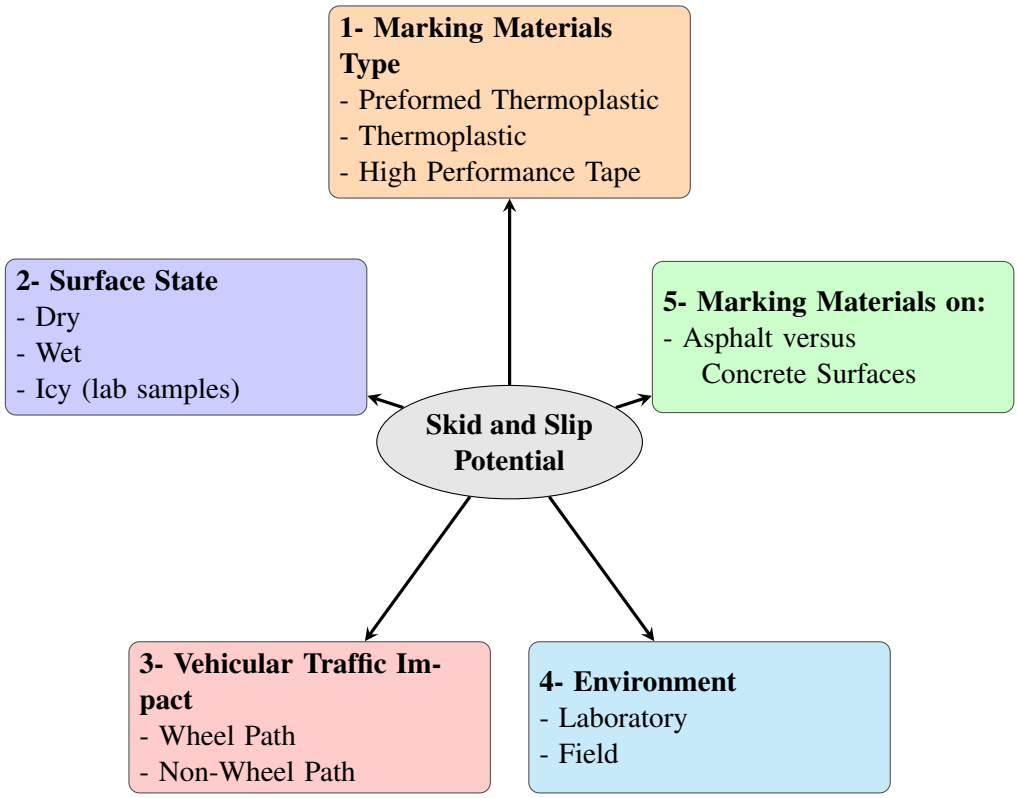

Figure 2.4: Factors Considered in Skid and Slip Friction Experimentation

2.5 Results And Analysis

2.5.1 Laboratory Analysis of Pavement Markings: TSR and PSR in Various Conditions

Figure 2.5 presents a sample of the laboratory results for the various pavement marking materials included in the study using the average BPN* values for TSR and PSR. These were calculated based on 108 measurements obtained from 18 distinct samples with six repetitive measurements. Laboratory and field tests showed that the BPN measurements were consistent in dry, wet, and icy conditions for both TSR and PSR, with a coefficient of variation ranging from 3% to 5%. The results presented herein are based on pavement markings applied to 12 concrete samples and 6 asphalt samples. For all the marking types, the same distribution was followed, that is, 4 concrete samples and 2 asphalt samples for each marking type. As expected, overall, the BPN* values for the TSR and PSR decrease from dry to wet and icy conditions. The high-performance tape, T, marking provided the highest BPN values under dry (D) conditions for both TSR and PSR, reflecting thus a higher level of friction. As expected, in wet (W) and icy (I) conditions, a decrease in BPN is observed. Preformed thermoplastic (P) and Thermoplastic (Th) materials follow a similar trend but with a lower baseline in D conditions, reflecting the lower inherent surface textural properties impacting the slip and skid resistance mechanisms.

2.5.2 Influence of Pavement Surface Type (Concrete versus Asphalt) on BPT Measurements

Following the overall assessment and trends in BPN on alternate pavement marking and surface conditions, Figure 2.6, it was of interest to examine whether the pavement surface type that these pavement markings were applied had any influence on skid and slip resistance. An example of such a comparison is shown in Figure 2.6 for the high-performance tape, T applied on asphalt and concrete surfaces. As can be observed, the trends of both TSR and PSR are consistent for both mixture types (i.e., asphalt and concrete) and throughout the three alternative surface conditions (D, W, I). The same result was observed for the remaining pavement markings, concluding thus that pavement type does not influence the surface friction of pavement markings.

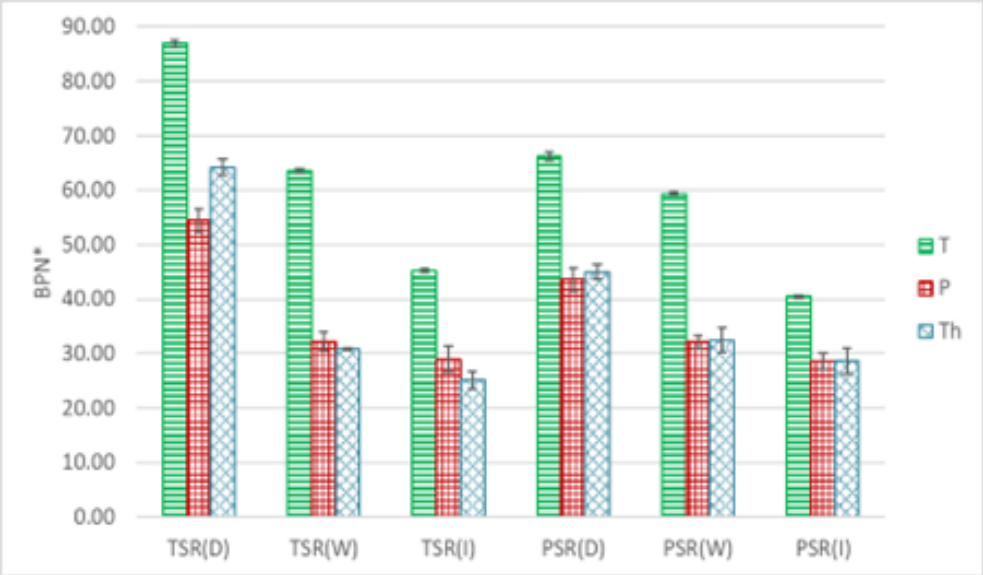

Figure 2.5: TSR and PSR on Pavement Markings under Laboratory Conditions
Note: BPN average values from 18 samples and $n = 6$ replicate measurements. Standard deviation (repeatability) bars shown on top of each case.*

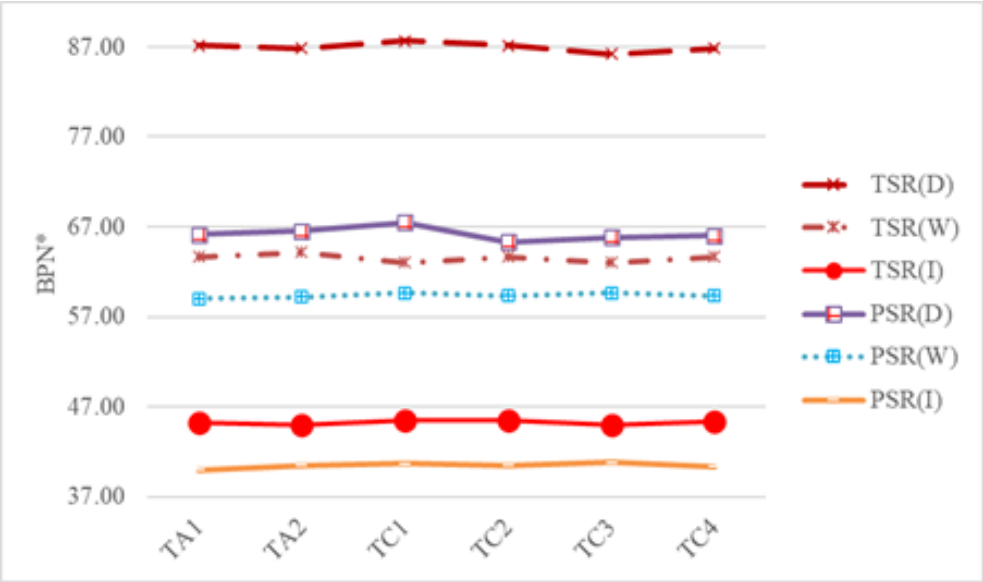

Figure 2.6: Example of Effects of Pavement Surface (Asphalt vs Concrete) on TSR and PSR for Tape Marking
Note: Average BPN values based on $n = 6$ repetitions. TA1, TA2: tape markings on asphalt; TC1 to TC4: tape markings on concrete.*

2.5.3 Slip and Skid Resistance Across Alternative Field Pavement Markings with Preformed Thermoplastic

As indicated earlier, the current direction of the state is to move primarily towards the use of preformed thermoplastic (P) materials. Thus, the majority of the field sites (13 out of 18 sites), included locations where P was installed. These represent sites where P was applied at different times and experienced variable traffic levels, thus representing variable wear and tear from each other. Figure 2.7 presents such a comparison of TSR and PSR under both the D and W conditions. While both TSR and PSR display variability across locations for the reasons mentioned above, the TSR values in D conditions overall maintain a higher threshold (except in one location, #10, perhaps reflecting testing variability in this specific case). The presence of water on the surface demonstrates a notable decrease in BPN values, reflecting the pavement

marking's reduced surface friction under W conditions.

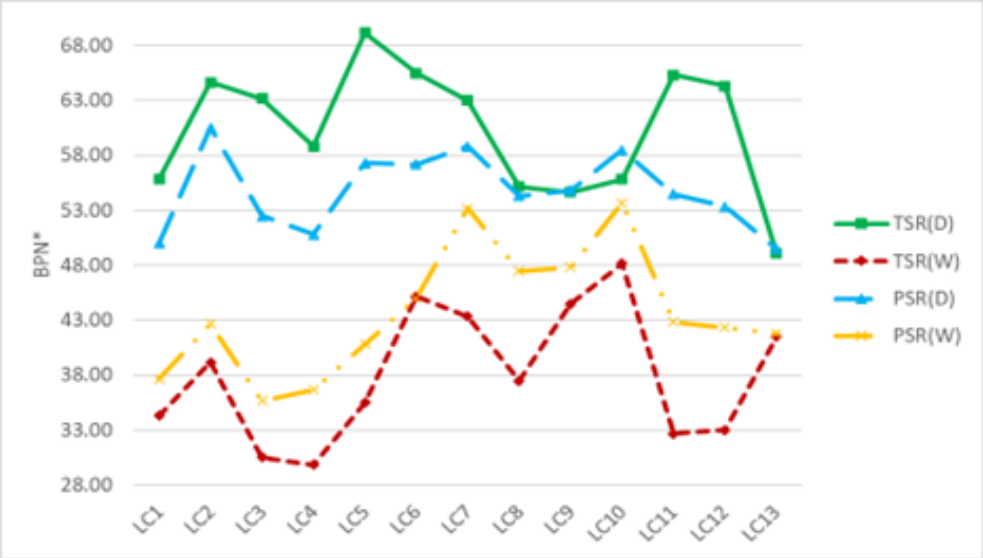

Figure 2.7: Field Evaluation of Preformed Thermoplastic: TSR and PSR Measurements in Dry and Wet Conditions
Note: Average BPN values based on* $n = 6$ *repetitions.*

2.5.4 Impact of Lane Location (Wheel Path vs Non-Wheel Path) on BPT Measurements

Since the degree of wear and tear from higher or lower traffic levels is expected to alter surface friction characteristics of pavement markings, it was of interest to assess such cases. Figure 2.8 shows an example of preformed thermoplastic markings for the wheel path versus the off-wheel path, illustrating the visual distinction between the two locations. Figure 2.9 presents an example comparison between slip and skid resistance on preformed thermoplastic, P, at two side-by-side locations where one is right on the tire marks of the vehicle's wheel path, while the second is off the wheel path, at the same marking location and lane. As can be seen from this figure, both TSR and PSR at the wheel path are consistently lower for both dry and wet

conditions. The small one standard deviation shown at the top of each bar calculated from the repeated measurements ($n = 6$) provided further confidence that BPN can account for such a difference between such cases. Further testing is currently being conducted to further reinforce such findings and statistically assess the significance.

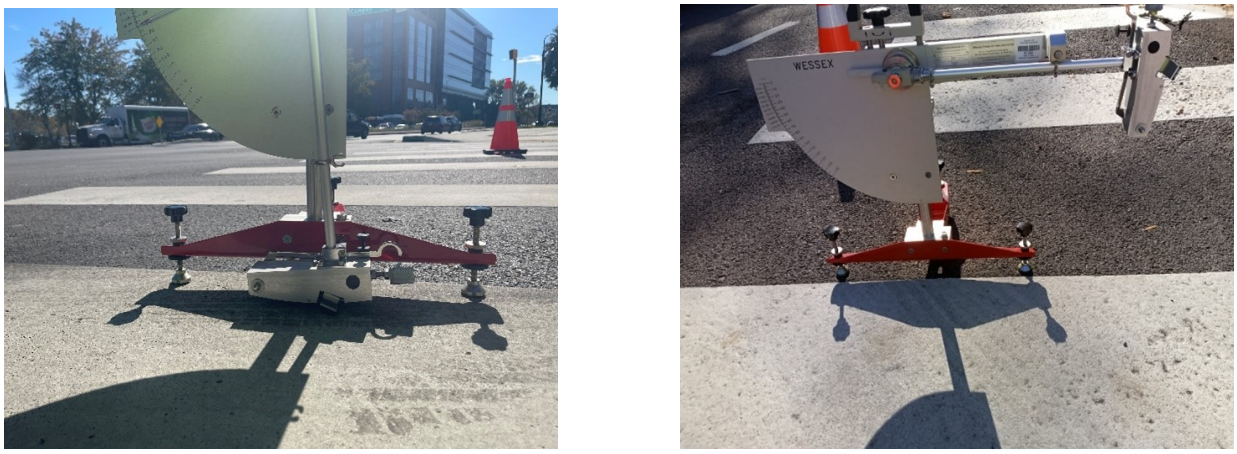

(a) (b)

Figure 2.8: Preformed Thermoplastic Markings for (a) Wheel Path, and (b) Off Wheel Path

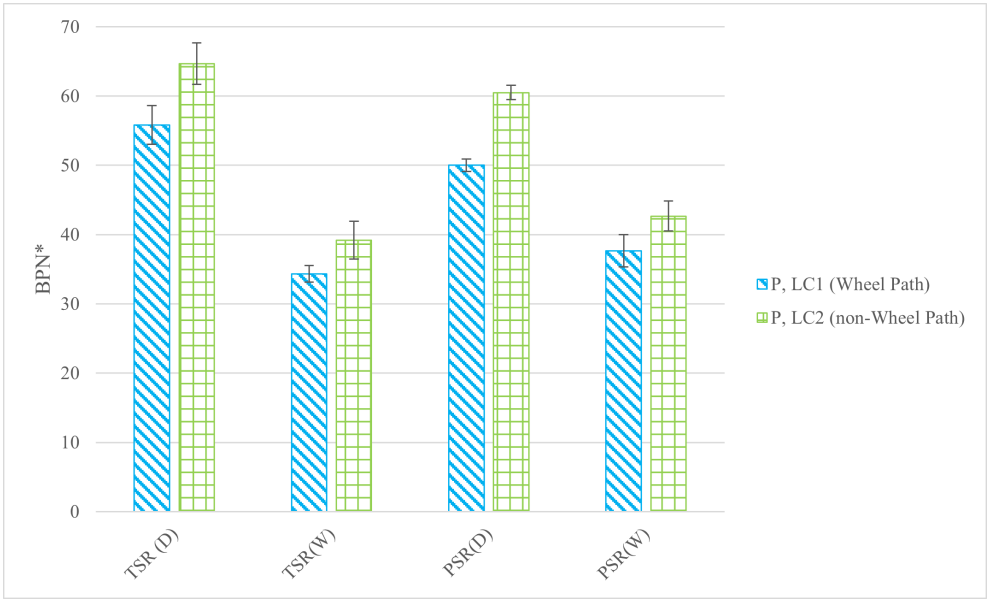

Figure 2.9: Effect of Traffic (i.e., Tire Marks) on BPN (D, W) with PSR & TSR

2.5.5 Statistical Significance

The laboratory and field data were then analyzed using ANOVA/MANOVA and paired t-test. Table 2.4 provides comparative results between ANOVA/MANOVA and paired t-tests on the laboratory data for evaluating the slip and skid resistance of the alternative pavement markings from the BPN measurements. The objective of these analyses was to assess, at the aggregate level (i.e., independently whether they represent TSR and/or PSR measurements), if (i) the difference between D, W, and I are statistically significant, and (ii) to confirm whether the effects of alternative pavement markings on PSR were significant. The analysis dataset was based on a total of 216 observations, which were obtained from laboratory data, from 18 different samples with six replicates each. The samples included the three pavement marking materials, P, Th, and T, and included samples on both asphalt and concrete surfaces. As can be seen from the summary results of TABLE 4, statistically, D, W, and I, are always significant with both analyses (i.e., ANOVA/MANOVA and t-test). Also, the measurements on the alternative pavement marking (P, Th, T) are statistically significant at the 95% confidence level. As was observed from the data in Figure 9, the statistical analysis confirmed that measurements on the pavement markings applied on concrete (C) and asphalt (A) are not statistically different.

Table 2.4: Assessment of Statistical Significance of Variables in BPN Measurements

T-test Variables	**Ho**	**ANOVA/MANOVA Variables**	**AS**
BPN(D) vs BPN(W)	SS	BPN(D) vs BPN(W)	SS
BPN(D) vs BPN(I)	SS	BPN(D) vs BPN(I)	SS
BPN(W) vs BPN(I)	SS	BPN(W) vs BPN(I)	SS
BPN(P) vs BPN(T)	SS	BPN(P) vs BPN(T)	SS
BPN(P) vs BPN(Th)	SS	BPN(P) vs BPN(Th)	SS
BPN(Th) vs BPN(T)	SS	BPN(Th) vs BPN(T)	SS
BPN(A) vs BPN(C)	NS	BPN(A) vs BPN(C)	NS

Note: SS = statistically significant at the 95% confidence level; NS = not statistically significant; Ho = null hypothesis, average values of paired tests are equal; AS = association between variables.

2.6 Predictive relationships

The next step of the analysis was to assess predictive relationships between PSR and TSR, and/or their relationship to D, W, and I conditions. While alternative models were searched to fit the data the the standardized linear model provided the best fit:

$$\mathrm{BPN}_{\mathrm{Response}} = \alpha + \beta \cdot \mathrm{BPN}_{\mathrm{Predictor}} \tag{2.7}$$

where $BPN_{Response}$ is the response variable representing the British Pendulum Number under each test condition of interest, α is the model intercept (set to zero for all cases), and β is the slope coefficient relating the predictor variable $BPN_{Predictor}$. So many correlations were obtained to comprehensively assess the relationships of TSR and PSR under varied surface conditions, test environments, and marking types. This approach provides a comprehensive understanding of the performance of these models in various scenarios and helps validate them. A 95% confidence

interval was considered, and the R^2 and root mean square error (RMSE) were calculated to assess how well the selected model fits the observations. The 95% confidence level ensures that the correlations are reliable and that any results will be less affected by random variation. α was set equal to zero because it is assumed that the relationship should go through the origin, as there would be no response in BPN if there were no predictor variables present. The correlations are presented in Tables 2.5–2.7, and Figure 2.10 illustrates the comparison among these correlations.

In terms of the PSR measurements from the laboratory experimentation a total of 1,296 observations were obtained from 18 samples (six samples with P, six with Th, and six with T) with six replicate measurements for each determination, three surface conditions (D, W, I), two BPT testing devices, and using two pads (one for TSR and another for PSR). Example relationships between TSR and PSR for each condition (D, W, I), are presented in Table 2.5 for the preformed thermoplastic, P, case. As can be observed, this model fits the data very well (i.e., high R^2 and low Root Mean Square Error, RMSE) and thus provides the ability to relate well measurements between vehicle skid and pedestrian slip at the various surface conditions (D, W, I). Also, good models relating TSR to alternative surface conditions were obtained, Table 2.5. Similar results were obtained for PSR, as well as for the remaining two pavement markings (Th and T). An example relationship between TSR and PSR in dry conditions on the preformed thermoplastic with laboratory measurements is shown in Figure 2.11.

Similarly, the field data were used for assessing potential predictive relationships between PSR and TSR, and/or the ability to relate D and W measurements. A total of 984 field observations were considered obtained from 18 field sites, monitored either two or three times, with six repetitions in each case, at two surface conditions (D, W) and using the two pads for TSR and PSR on three types of pavement markings (P, Th, T). The field data provided as well good

model relating PSR and TSR for each surface condition (D, W), as well as relating TSR to alternative surface conditions. Selected results for the preformed thermoplastic, P, case are presented in Table 2.6. Similar results were obtained for PSR, as well as for the remaining two pavement markings (Th and T).

The next step in the analysis was pertinent to eventually relate laboratory (L) and field (F) BPN observations. This included 1,848 observations by combining the lab and field data obtained from the tire slip rubber (TSR) and pedestrian slip rubber (PSR) measurements across different settings described previously. Examples of such relationships for the preformed thermoplastic (P) measurements are presented in Table 2.7. As can be observed good relationship between field and Lab measurements was obtained for TSR and PSR at both D and W conditions. Similar results were obtained for the remaining two pavement markings (Th and T).

Table 2.5: Example Models Relating BPN for Various Conditions Based on Lab Testing for Preformed Thermoplastic, P

Marking Type	**Data Comparison**	β	R^2	**RMSE**
P	D: (TSR & PSR)	1.25221	0.99	0.587
	W: (TSR & PSR)	1.00972	0.99	0.542
	I: (TSR & PSR)	0.99861	0.99	1.178
	D vs W (TSR)	1.65898	0.99	1.866
	D to I: (TSR)	1.89010	0.99	2.613
	W to I: (TSR)	1.14224	0.99	0.756

Note: 95% significance level; RMSE = Root Mean Square Error.

Table 2.6: Example Models Relating BPN for Various Conditions Based on Field Testing for Preformed Thermoplastic, P

Marking Type	**Data Comparison**	β	R^2	**RMSE**
P	D: (TSR & PSR)	1.10847	0.99	1.931
	W: (TSR & PSR)	0.87087	0.99	1.229
	D to W: (TSR)	1.59439	0.99	4.073
	D to W: (PSR)	1.25283	0.99	3.560

Note: 95% significance level; RMSE = Root Mean Square Error.

Table 2.7: Example Models Relating Field and Lab BPN Measurements for Various Conditions on Preformed Thermoplastic, P

Marking Type	**Data Comparison**	β	R^2	**RMSE**
P	TSR: F to L (D)	0.98724	0.9994	1.376
	TSR: F to L (W)	0.96307	0.9994	0.802
	PSR: F to L (D)	1.15429	0.9998	0.780
	PSR: F to L (W)	1.15302	0.9994	0.945

Note: 95% significance level; RMSE = Root Mean Square Error.

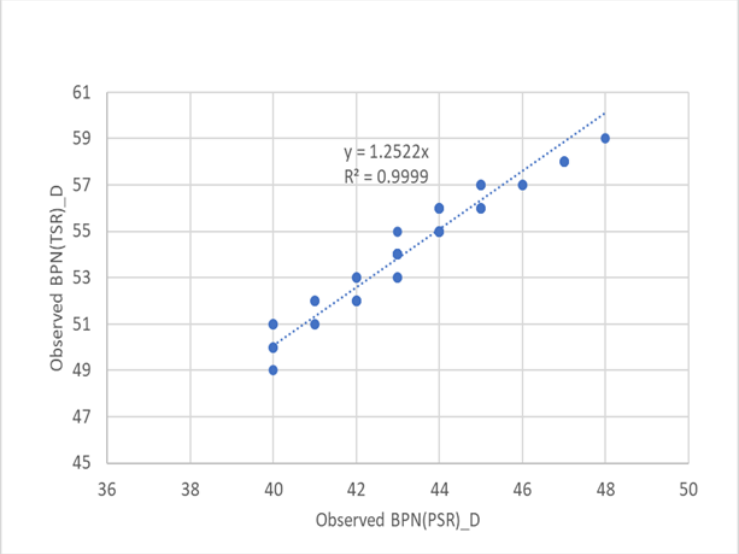

Figure 2.10: Comparison of Laboratory and Field BPN Measurements and Correlations Across Various Conditions for Preformed Thermoplastic (P)

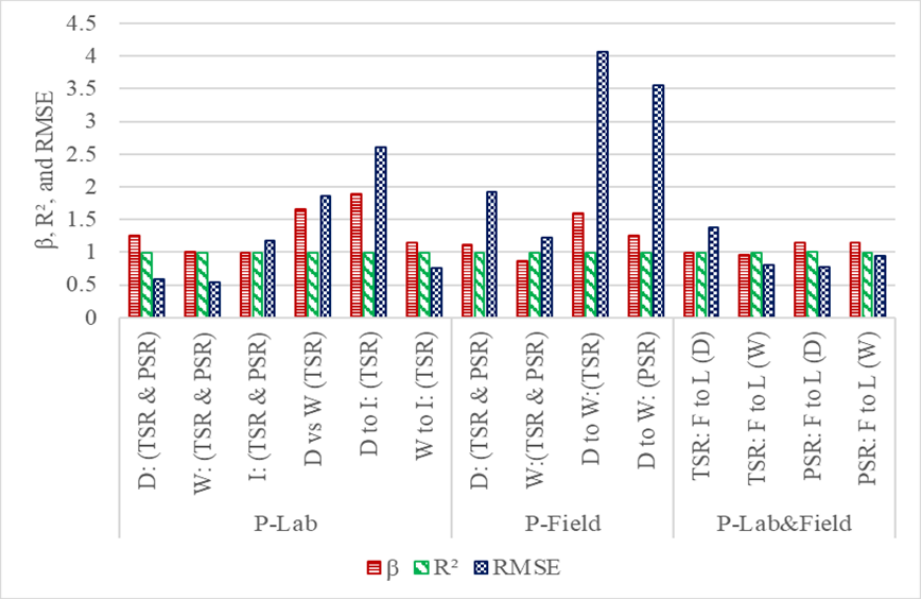

Figure 2.11: Predictive Relationships Between TSR and PSR for Preformed Thermoplastic in Dry Conditions with Lab Measurements
Note: Average BPN values*

2.7 Conclusions & Recommendations

This study examined the friction properties of pavements with markings in crosswalks. Based on the current friction acceptance specification in the state, the BPT was used for such evaluation. Both laboratory and field testing were included in the experimental study for the most prevailing pavement surface marking types used in the state. BPT testing repeatability was relatively low, and the results indicated that surface conditions (such as wet, dry, and icy conditions) affected vehicular and pedestrian friction. Differences in friction level for both TSR and PSR were observed for the three main types of pavement markings (Th, P, and T). However, the pavement surfaces (asphalt vs concrete) on these markings were applied on had no impact on the friction measurements.

The field results were consistent with the laboratory findings, in terms of the impact of materials and surface conditions, thus permitting the potential link between friction evaluated

in the lab and the field. This is particularly important since field measurements can be linked to laboratory evaluation for these materials, thus minimizing the need for field testing. This is beneficial since field testing requires traffic control with potential implications on cost and safety. The impact of traffic wear and tear on pavement marking friction within a traffic lane was found to be relevant.

Good predictive relationships between PSR and TSR were obtained, and their influence on D, W, and I conditions. This was the case for all three pavement marking material types included in the study. The same was observed from both the laboratory and field data, providing the ability to estimate BPN measurements and thus minimize future testing. The ability to relate lab and field measurements in terms of TSR and PSR is particularly beneficial in terms of process control and Quality Assurance since it minimizes the need for testing, particularly in the field.

Finally, the link between PSR and TSR provides the possibility to revise current acceptance specifications for pavement marking materials to incorporate requirements regarding pedestrian slip resistance along with vehicular skid resistance by additional threshold values for BPN. It is expected that such a revision will enhance the safety of pavements at crossings. Overall, this extensive study has provided additional insights into crosswalk pavement friction and represents one of only very few studies relating vehicular friction and pedestrian slip resistance for such a range of conditions and materials.

Due to the study's importance in regard to pavement safety and findings, the AASHTO Research Advisory Committee (RAC) recently voted for such research study for the 2025 "Sweet 16 High-Value Research Award." Thus, several states are expected to adopt the study findings and recommendations for potential transferability to their pavement conditions and materials, and for enhancing their pavement friction specifications.

Chapter 3: Round Robin Assessment of BPTs for Pavement Marking QA

3.1 Overview

The global concern for road safety has led to an increased emphasis on better understanding the factors that contribute to pedestrian and vehicular safety [53]. In this context, the assessment of vehicular skid and pedestrian slip resistance is a crucial aspect of road condition evaluation and safety [9,54,55]. The use of BPT for skid resistance evaluation by various agencies has generated significant attention [56]. However, the relationship between vehicular skid resistance (i.e., tire slip resistance, TSR) and pedestrian slip resistance (PSR) has been examined to a lesser degree [56]. The effects of various conditions and pavement surfaces and marking materials on the British Pendulum Number, BPN, in regards to primarily vehicular friction have been examined in various studies [57–59]. However, only limited attempts have been explored for relating vehicle and pedestrian friction interaction [60] for variable environmental conditions, such as dry (D), wet (W), and/or icy (I) surface conditions, and to a much lesser degree on pavement markings at crossings.

Thus, while the overall objective of this study was to relate vehicle skid friction, TSR, to pedestrian slip resistance, PSR, for pavement sections with crossing markings using the British Pendulum Tester (BPT), it was imperative to assess and compare the response of alternative BPT units regarding their ability to provide reproducible and comparable evaluation of both vehicle skid friction and pedestrian slip resistance on these pavement surfaces and materials. Such assess-

ment was particularly critical since the current acceptance specification for the state of Maryland, as well as several other states, is based on the pavement surface friction of vehicles using the BPT device, with contractors and the state using their own testing units. Thus, for the comparative friction assessment, two BPT units were used for side-by-side lab and field comparison on alternative pavement surface materials at crosswalks used regularly in Maryland. Furthermore, to better understand the response of the BPT devices and the mechanics of pavement surface friction on alternative markings, microscopic surface imaging on alternative material and Fourier transform analysis on consecutive measurements were conducted.

3.2 Literature Review

3.2.1 BPT Calibration and Friction Specifications

Since some state specifications of pavement friction evaluation at crossings are based on the BPT, previous studies have suggested calibration procedures that are simple and practical [61]. With the introduction of the redesigned pendulum arm, user-friendly calibration before each daily use is possible. Strautins [62] had further stressed the role of calibration for consistent measurements, outlining two approaches: direct calibration (i.e., examining specifications like arm mass and center of gravity), and indirect calibration via reference material comparison. Collaborative international efforts [62] have yielded bias correction and pertinent sensitivity coefficients in regard to the determination of a PTV used elsewhere.

Various factors affect road surface friction. Included are road surface texture, tire characteristics, and potential contaminants. Other factors contributing to this include tread pattern, rubber hardness, inflation pressure, and sliding velocity, along with road properties such as microtex-

ture, macrotexture, and surface temperature. Contaminants like water or oil can influence friction depending on their viscosity, film thickness, and chemical structure [63–66]. These variables interact to determine overall friction performance. Various levels of BPN for vehicle skid resistance have been proposed with alternative pavement surface treatments [67], with suggested skid numbers close to 40. Alternative values have been proposed based on a state-of-the-art review of skid resistance measurement in asphalt and pervious pavement mixtures [20, 25, 69]. Similarly, the potential for slip is based on floor material, environmental conditions, level of contamination, footwear properties, and human behaviors, all of which influence the dynamic interactions that in turn influence slip resistance [70].

Finally, a recent study [6] investigated the slip resistance of thermoplastic markings and compared it with that of traditional road materials. It was found that well-designed and maintained thermoplastic materials, though different in composition, could provide adequate slip resistance. Tables 3.1 and 3.2 provide a detailed summary of some illustrative skid and slip resistance thresholds and observations. It provides classifications according to standards such as ANSI B101.3 and UK guidelines, and also includes observed BPN ranges for various materials and treatments.

Table 3.1: Illustrative Skid and Slip Resistance Thresholds and Observations (Part 1) [27, 47]

Standard/Reference	**Assessment**	**Condition/Threshold**	**Classification/Observations**
[71]	Wet COF (Slip)	$\mu \geq 0.42^*$	Lower probability of slipping
		$0.3 \leq \mu < 0.42^*$	Increased probability of slipping
		$\mu < 0.3^*$	Higher probability of slipping
[71]	Wet COF (Slip)	$\mu \geq 0.42^*$	–
[70]	COF (Slip)	0–0.24*	High slip potential
		0.25–0.36*	Moderate slip potential
		$> 0.36^*$	Low slip potential
	PTV (Slip)	0–24*	High slip potential
		25–35*	Moderate slip potential
		$\geq 35^*$	Low slip potential
[72]	BPN (Skid & Slip)	$> 54^*$, $> 44^\dagger$	Class: P5
		$45–54^*$, $40–44^\dagger$	Class: P4
		$35–44^*$, $35–39^\dagger$	Class: P3
		$25–34^*$, $20–34^\dagger$	Class: P2
		$12–24^*$, $< 20^\dagger$	Class: P1
		$< 12^*$, –	Class: P0
[73]	PTV (Slip)	$\geq 40^*$	–
[74]	BPT (Skid)	BPN (D) = $70^\dagger$	Rough-superhydrophobic coating on coarse surface
		BPN (W) = $60^\dagger$	
		BPN (I) = $48^\dagger$	

Table 3.2: Illustrative Skid and Slip Resistance Thresholds and Observations (Part 2) [27, 47]

Standard/Reference	Assessment	Condition/Threshold	Classification/Observations
[75]	BPT (Skid & Slip)	BPN (D) = 100† BPN (W) = 87.5† BPN (I) = 28†	PA
		BPN (D) = 100† BPN (W) = 72.5† BPN (I) = 28.5†	DMA
		BPN (D) = 96† BPN (W) = 74.5† BPN (I) = 29†	PC
[60]		BPN (D) = 72*, 84† BPN (W) = 64*, 72† BPN (I) = 22*, 31†	PCC
		BPN (D) = 89*, 104† BPN (W) = 79*, 94† BPN (I) = 45*, 59†	PC
[76]		BPN (Wet w/o de-icer) = 90.4† BPN (Wet w/ de-icer) = 60†	PCC, Solution: 23.3% Brine + 27.7% Maltitol
[6]		BPN (D) = 78*, 87† BPN (W) = 65*, 64† BPN (I) = 42*, 42†	Preformed tape
		BPN (D) = 64*, 100† BPN (W) = 50*, 50† BPN (I) = 33*, 33†	Paint with beads
		BPN (D) = 55*, 62† BPN (W) = 43*, 42† BPN (I) = 30*, 30†	Thermoplastic with beads

Note: BPN = British Pendulum Number; COF = Coefficient of Friction; PTV = Pendulum Test Value; D = Dry; W = Wet; I = Icy; PCC = Portland Cement Concrete; PC = Pervious Concrete; DMA = Dense Modified Asphalt; PA = Porous Asphalt.
* indicates **slip** resistance thresholds; † indicates **skid** resistance thresholds.

3.2.2 Skid and Slip Resistance

Vehicle tire skid resistance on pavement road surfaces has been examined to a great extent [77]. Past studies have considered assessment of alternative methods and measurements, potential influence of roadway conditions, such as surface roughness, in friction, and so on [78]. The impact of skid resistance on operational costs, traffic accidents, and fatalities has been reviewed as well, particularly in wet conditions. A review of alternative skid resistance measurement techniques and innovative road sensors has been presented as well [13].

While the use of BPT has been in some cases characterized as empirical in nature, the fundamental work by Chu et al. [15] asserted the theoretical underpinnings of BPN. Through a physics-based simulation model, the study established a mechanistic link between the measured BPN and friction coefficient, debunking the belief that BPN is solely an empirical index. Thus, such a study highlighted the BPT's theoretical foundation and its implications for accurate pavement friction assessment.

Further reviews have compared the strengths and weaknesses of alternative pavement surface frictional measurement methods [63], with suggestions for the development of refined measurement techniques to advance the assessment of skid resistance.

Table 3.3 classifies the requirements for skid resistance into four zones, each with a recommended minimum testing approach, ranging from routine monitoring in low skid resistance zones to comprehensive network evaluations in high skid resistance zones. This framework emphasizes how testing approaches should be tailored according to the particular requirements of a zone.

While most studies focus on traditional pavement materials (i.e., asphalt and concrete), the importance of surface friction on pavement markings has received less attention. The in-

dispensable role of these markings in road behavior and safety has been presented in recent studies [68, 79].

Similarly, Table 3.4 categorizes slip risk levels and their common applications, ranging from very low (PTV $>$ 55) to very high (PTV $\leq$ 24), based on the Pendulum Test Value (PTV) measured using the BPT and related to the friction coefficient μ by Equation 3.1, which provides an essential classification for assessing safety in different conditions [80].

$$\text{PTV} \approx \frac{330\mu}{3+\mu} \tag{3.1}$$

Table 3.3: Categories of Skid Resistance Requirements [5, 81]

Zone Type	**Recommended Minimum Testing Approach**
Low skid resistance zone	Routine monitoring (e.g., network laser texture surveys or basic visual inspections).
Medium skid resistance zone	Specific testing (e.g., portable or towed devices such as the British Pendulum, GripTester, or ROAR).
High skid resistance zone	Comprehensive network evaluations (e.g., SCRIM, or towed/portable devices where feasible).
High-density urban zone	SCRIM or GripTester for sites with restricted access.

Table 3.4: Categories of Slip Resistance Risk Levels [80, 82]

Slip Risk	**PTV Range**	**Common Applications**
Very Low	$>$55	Outdoor areas, ramps
Low	45–54	Exterior walkways, poolside areas, outdoor stairs
Medium	35–44	Shopping centers, hotel lobbies, public changing rooms, indoor stairs
High	24–34	Bathrooms, storage rooms, laundry spaces
Very High	$<$24	Shopping malls

3.2.3 Mechanistic Interpretation of Tire-Pavement Friction

Pavement friction is largely determined by two primary mechanisms: adhesion (A) and hysteresis (H), as illustrated in Figure 3.1. Adhesion results from molecular bonding at high-pressure contact points due to surface irregularities, while hysteresis involves energy loss as tire rubber adapts to features such as ridges and depressions [83]. Therefore, friction can be considered as the combination of adhesion and hysteresis forces (both in Newtons, N), as expressed in Equation 3.2 [84].

$$F = F_A + F_H \tag{3.2}$$

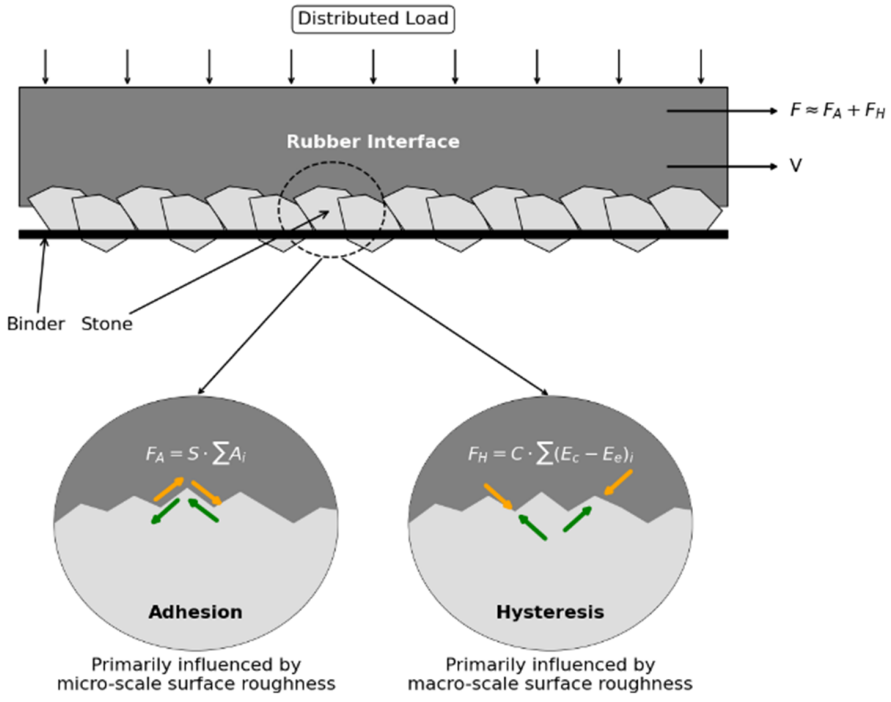

Figure 3.1: Key components of rubber-tire friction. Reproduced from [63], [85], and [86].

Additionally, minor contributors to friction include effects from rubber wear and micro-

hysteresis, as distinct from bulk hysteresis. Research over the past decade has confirmed that rubber wear can contribute to cohesion loss as part of the overall frictional force [87, 88].

In transport engineering, the concept of friction specifically relates to tire-pavement interaction. This friction arises from two distinct surface texture characteristics: microtexture and macrotexture. These terms are traditionally classified based on the texture wavelength (λ_w) and spatial frequency. Different fields approach texture and friction with varying focuses; for instance, mechanical engineering often examines friction with machinery and lubricants, whereas transportation infrastructure engineering centers on the tire-pavement interface and traffic safety considerations.

Pavement friction is described as "the force that resists the relative motion between a vehicle tire and a pavement surface" [84]. This resistance is typically measured using a dimensionless value called the coefficient of friction (μ), which characterizes tire-pavement friction. The friction coefficient is calculated as the ratio between the tangential force (F_T) at the tire-pavement contact point and the longitudinal force (F_w) acting on the wheel (all in Newtons, N). The friction coefficient (μ) is unitless and can be expressed as shown in Equation 3.3 [89]:

$$\mu = \frac{F_T}{F_w} \tag{3.3}$$

3.2.4 Energy Absorption and Dynamic Surface Friction

The BPT measures dynamic surface friction by assessing the pendulum's energy loss in its swing, that is, the work done by the pendulum against friction produced between the slider and the test surface. This energy loss indicates the kinetic energy that is dissipated because of

frictional forces [47, 90]. Work done against friction is given as:

$$WF = \mu PD \tag{3.4}$$

Where: WF is work done against friction (J); μ is the effective coefficient of friction between the slider and the surface (unitless); P is the average normal load between the slider and surface (N); and D is the sliding distance over the test surface (m).

At the same time, the loss in energy of the pendulum arm during its interaction with the surface can be expressed as:

$$\Delta E = W(H - h) \tag{3.5}$$

Where: ΔE is the loss in energy of the pendulum arm (J); W represents the effective weight of the swinging arm (N); H is the initial height of the center of gravity of the pendulum in its release position (m); and h is the height of the center of gravity at the highest point reached after the slider has contacted the test surface (m).

By equating the energy lost in the pendulum arm to the work done against friction, we derive the effective friction coefficient μ as:

$$BPN = 100\mu_e = 100\left(\frac{W(H-h)}{DP}\right) \tag{3.6}$$

Therefore, the coefficient of friction μ can thus be calculated based on the mechanical properties of the pendulum and test parameters, with the height difference $H - h$ reflecting the energy absorbed by the surface friction.

In this context, μ_e is the friction coefficient. The value of P depends on the unique force-deflection curve of each BPT slider, which means different BPT devices may yield varied measurements for identical surfaces. The slider's rubber is characterized as hyperelastic, with its elastic modulus calculated based on hardness, as shown in Equation 3.7 [90]:

$$\log_{10} E = 0.0198 H_r - 0.5432 \tag{3.7}$$

Where: E is measured in MPa; and H_r represents the International Rubber Hardness Degrees (IRHD) of the slider rubber.

According to BS EN 13034 standards [48], the IRHD for BPT rubber sliders used in pedestrian slip resistance testing typically ranges from 94 to 98 and 55 to 61 for skid pads.

3.2.5 Fourier Transform for Texture Analysis

The Fourier Transform (FT) can be used in an attempt to analyze pavement surface texture by decomposing the surface height profile into its frequency components. The advantage of FT is that it makes the underlying patterns more visible in the frequency domain, that is, what frequencies are present in a signal and their relative amplitudes [91, 92]. This provides further insight into the structure of the profile and characteristics valuable for understanding friction [93]. Fourier theory represents a signal as a summation of all sinusoidal waves running with different frequencies and amplitudes to determine the contribution of each constituent component of the signal itself [94]. Fourier analysis involves i) Fourier series on periodic functions, and ii) Fourier Transform for non-periodic functions [95]. The surface height profile can be decomposed into frequency components through FT, enabling the differentiation between macrotexture—low-

frequency components mainly influencing hysteresis—and microtexture—high-frequency components enhancing adhesion in this study. Decomposition like this supports understanding for potentially enhancing frictional performance in pavement surfaces and marking materials.

To analyze a non-periodic signal $x_T(t)$, it will be repeated over an arbitrary period T_0, creating a periodic signal $x_{T_0}(t)$ where $\lim_{T_0 \to \infty} x_{T_0}(t) = x(t)$. The FT representation that may be used is:

$$x_{T_0}(t) = \sum_{k=-\infty}^{\infty} C_k e^{i2\pi k/Tt} \tag{3.8}$$

Where: $x_{T_0}(t)$ is the periodic representation of the signal; C_k are the Fourier coefficients representing the amplitude of each frequency component; T_0 is the period of the repeated signal; k is an integer representing each harmonic frequency; i is the imaginary unit; t is the spatial variable.

The Fourier coefficients C_k, capturing the amplitude of each frequency, will be calculated as follows:

$$C_k = \frac{1}{T_0} \int_{-T_0/2}^{T_0/2} x(t) e^{-2\pi i (k/T_0)t} \, dt \tag{3.9}$$

For non-periodic signals where $x(t)$ is zero outside $(-T_1, T_1)$, this simplifies to:

$$C_k = \frac{1}{T_0} \int_{-\infty}^{\infty} x(t) e^{-2\pi i (k/T_0)t} \, dt \tag{3.10}$$

FT will allow the separation of the surface height profile into frequency components, whereby microtexture corresponds to high-frequency components that enhance adhesion while macrotexture corresponds to the low-frequency components that will mainly affect hysteresis.

3.3 Experimental Design & Scoping

The experimental design in this study is presented in Figure 3.2. The first series of steps involved the selection of the British Pendulum Tester (BPT) devices. The first BPT unit was the one currently used routinely by the Maryland highway agency for assessment and acceptance of pavement surfaces and marking materials at crosswalks. Since contractors purchase and use their own units, for comparison, reproducibility, and repeatability assessment, a second BPT unit was bought identical in specification to that of the agency's unit (see Figure 3.3). While only two units were studied, this was sufficient since any unit to be purchased and used by the contractors had to meet the strict manufacturing specifications and requirements, meeting those of the state agency BPT unit. Thus, these units were compared side by side on alternative materials and conditions. Moreover, operators with different levels of experience were included in testing to assess possible variability from operator to operator.

The next step for the study was to identify the most commonly used pavement marking types for crosswalks in Maryland. These included three types of pavement markings, Figure 3.4, preformed thermoplastic (P), high-performance tape (T), and thermoplastic (Th).

Next, the study incorporated three testing conditions to simulate environmental parameters: dry (D), wet (W), and icy (I). The wet conditions reflected the specification requirements for testing. For the wet (W) conditions, specimens were sprayed with water to simulate moisture on the surface, following state engineers' recommendations and prior studies [47]. This approach ensured realistic testing under common environmental conditions.

To simulate icy (I) conditions in the laboratory, recommendations from prior studies were followed [6]. A freeze-thaw chamber was employed for this process. The specimens with pave-

ment markings were submerged in a water reservoir at room temperature to ensure full immersion. This reservoir, containing the specimens, was then placed inside the freeze-thaw chamber, and the temperature inside the chamber was gradually lowered to 14°F (-10°C). Eventually, this controlled cooling caused the water in the reservoir to freeze around the specimens, thus simulating in-service freezing conditions. The specimens remained this way for two hours. After this period of freezing, the specimens were submerged in room-temperature water for five minutes to simulate thawing and were then carefully removed from the water tank. Thereafter, the specimens were placed back in the chamber for a further 30 minutes to allow the formation of ice crystals intentionally on their surfaces. At the end of this ice formation process, the specimens were removed from the chamber, and their surfaces were tested using the BPT apparatus.

Testing involved the assessment of both pedestrian slip and vehicle skid resistance using the specific rubber pads provided by the BPT manufacturer. The pad in the first instance is made of pedestrian slip rubber (PSR), also known as Four-S (Slider 96 pad), which has an IRHD hardness of 96 ± 2, and represents a pad equivalent to the heel of an ordinary shoe [96]. The second pad used is of tire rubber (tire slip rubber, or TSR), sometimes referred to as TRRL (Slider 55 pad), and it has an IRHD hardness of 55 ± 5. This pad has properties similar to those of an average road tire [96], aligning with the specifications outlined in ASTM E501.

The British Pendulum Tester is an apparatus to measure friction by simulating the dynamic contact of a rubber slider with the surface of the tested specimen, as shown in Figure 3.5. The device consists of a pendulum arm that pivots to swing free with a slider at its nadir. The friction characteristics of each specimen were measured according to the specification of ASTM E303 using the British Pendulum Tester (BPT) as illustrated in Figure 3.5. The values obtained provide the frictional resistance BPN (British Pendulum Number) recorded by BPT and shown in

Figure 3.5b.

The pendulum arm swings downwards, and at its lowest point, the rubber slider strikes the surface to simulate the action of a shoe sole or tire on the pavement surface. This oscillating pendulum arm causes the pad to strike the sample surface, thus providing a BPN output value proportional to the intrinsic frictional resistance of the surface. The target pads are mounted at the bottom of the pendulum arm with the rubber slider (PSR or TSR) attached firmly.

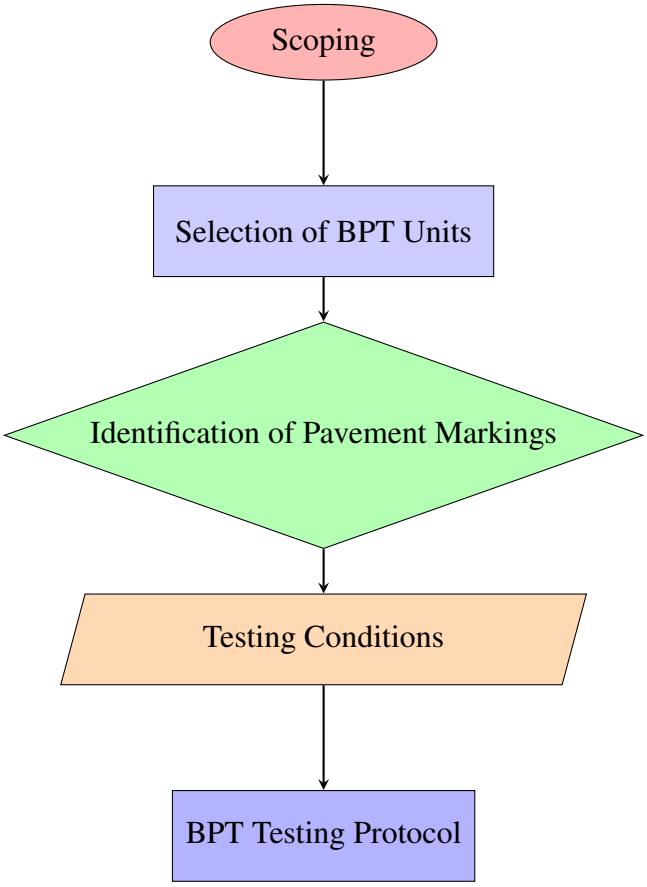

Figure 3.2: Experimental Design & Scoping

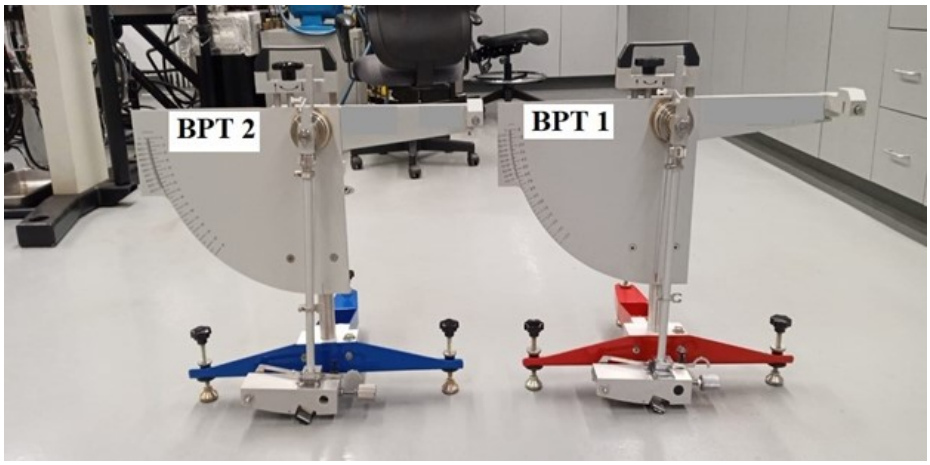

Figure 3.3: Selected British Pendulum Testers

Figure 3.4: Pavement Markings: (a) Preformed Thermoplastic, (b) High-Performance Tape, (c) Thermoplastic

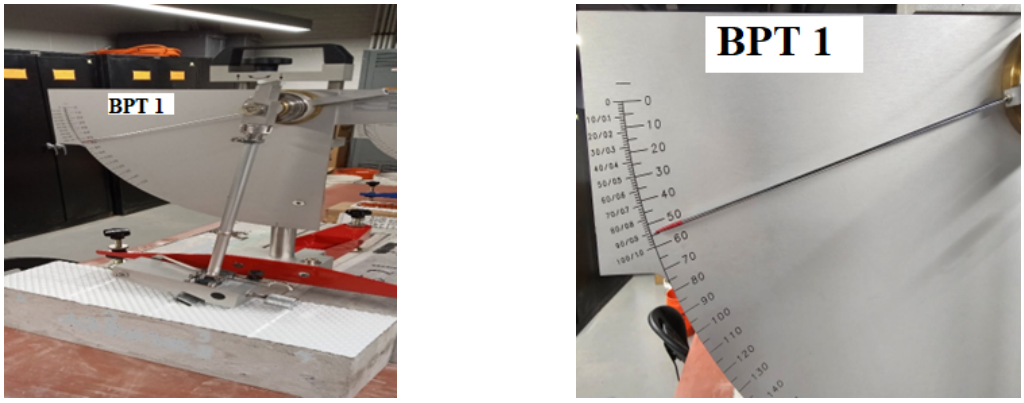

(a) (b)

Figure 3.5: British Pendulum Tester: (a) Instrumentation and (b) BPN Value Illustration

3.4 Experimental Testing and Analysis

The steps of the experimental testing and analysis are presented in Figure 3.6. The lab samples were prepared based on the environmental conditions, D, W, I, and pavement marking material types (P, T, Th), identified in the scoping session. Samples of concrete and asphalt were prepared to represent the mixtures used in the state. Lab concrete samples were beams of 53.3x15.2x15.2 cm (21x6x6 in) and asphalt gyratory compacted samples (i.e., "pills") of 15.2x6.2 cm (6x2.4 in).

Routine calibration of both BPT units followed the procedures identified in BS EN 13036 and ASTM E303, and the manufacturer's recommendations. The calibration process was verified to align with the standard practices used by the Maryland State Highway Administration (SHA). The TSR and PSR measurements were obtained with the two units on each sample and considering 6 repetitions for every measurement. For the test sequence, the two BPT units were executed successively on the same samples. The samples of icy specimens were refrozen and retested to ensure consistency across the measurements.

Statistical analyses were then used to assess the repeatability and reproducibility of the two BPT units and compare their results across various conditions. Analysis of Variance (ANOVA) and Multivariate Analysis of Variance (MANOVA) were used along with paired t-tests. Based on these analyses, results were obtained regarding the comparison of the measurements obtained by the two BPTs under various conditions and pavement marking materials.

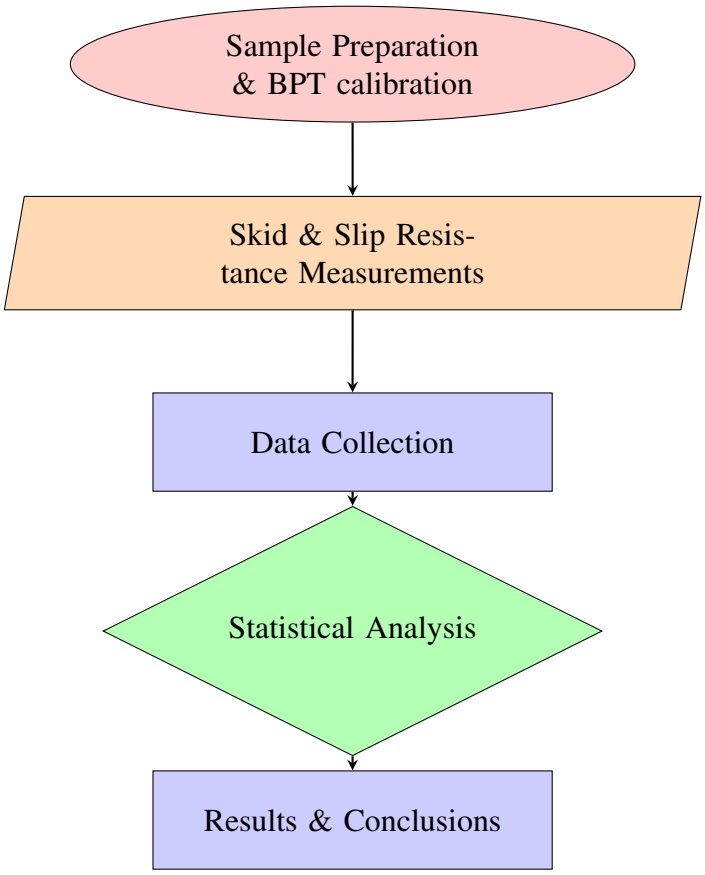

Figure 3.6: Experimental Testing and Analysis

3.5 Analysis and Results

3.5.1 Evaluation of BPT Devices for TSR and PSR

For the comparison of the two BPT units, a total of 216 BPN measurements were used produced from 18 asphalt and concrete samples with the three pavement marking types (P, T, Th), tested at three surface conditions (D, W, I), and with six replicate measurements in each case. Table 3.5 presents an example of the comparison of the BPN measurements obtained from the two devices on the high-performance tape, T, at dry (D), wet (W), and/or icy (I) conditions for both the tire slip resistance, (TSR), and pedestrian slip resistance (PSR). Along with the average

values of the BPN measurements on the asphalt (T, A) and concrete samples (T, C) and the 6 replicates, the standard deviation (SD) and coefficient of variation (CV%) are presented. As can be observed from Table 3.5, the average TSR values on asphalt samples (T, A) between the two units at each of the three surface conditions (D, W, and I) were very close. Furthermore, in terms of testing variability, a significantly low CV% was observed, in the range of 0.6% to 1.67%. Similar results were obtained for the PSR values on the asphalt samples as well as in concrete (T, C). The same effects were observed for the remaining two pavement marking materials (P, Th). Furthermore, the statistical analysis with both ANOVA/MANOVA and paired t-test confirmed that measurements on the pavement markings applied on concrete (C) and asphalt (A) were not statistically different.

Table 3.5: Example Results of TSR and PSR on High Performance Tape, T.

Pavement Marking	**BPN**	**Statistic**	**BPN1** (Dry) Unit 1	**BPN2** (Dry) Unit 2	**BPN1** (Wet) Unit 1	**BPN2** (Wet) Unit 2	**BPN1** (Icy) Unit 1	**BPN2** (Icy) Unit 2
T, A	TSR	SD	0.55	0.75	0.52	0.52	0.52	0.75
		Mean	86.5	87.17	63.67	63.67	45.33	45.17
		CV%	0.63	0.86	0.81	0.81	1.14	1.67
	PSR	SD	0.52	0.41	0.98	0.89	0.52	0.63
		Mean	66.33	66.17	58.83	59.00	40.33	40.00
		CV%	0.78	0.62	1.67	1.52	1.28	1.58
T, C	TSR	SD	0.52	0.52	0.98	0.00	0.41	0.55
		Mean	87.67	87.67	62.83	63.00	44.83	45.5
		CV%	0.59	0.59	1.56	0.00	0.91	1.20
	PSR	SD	0.75	0.55	0.75	0.52	0.52	0.52
		Mean	67.17	67.5	58.83	59.67	40.33	40.67
		CV%	1.12	0.81	1.28	0.87	1.28	1.27

Figure 3.7 compares the average TSR values under D conditions for the high-performance tape T applied to both asphalt and concrete samples using data obtained from two BPN units.

The figure represents, in total, the average of 6 samples: 4 concrete samples (T, C) and 2 asphalt samples (T, A). For each sample, 6 replicates were obtained ($n = 6$), and the average value from those replicates was calculated and plotted. It can be seen from this figure that the results reflect consistent values for each surface type and the 90th percentile boundaries. The same trend was observed for the other surface conditions and pavement marking materials.

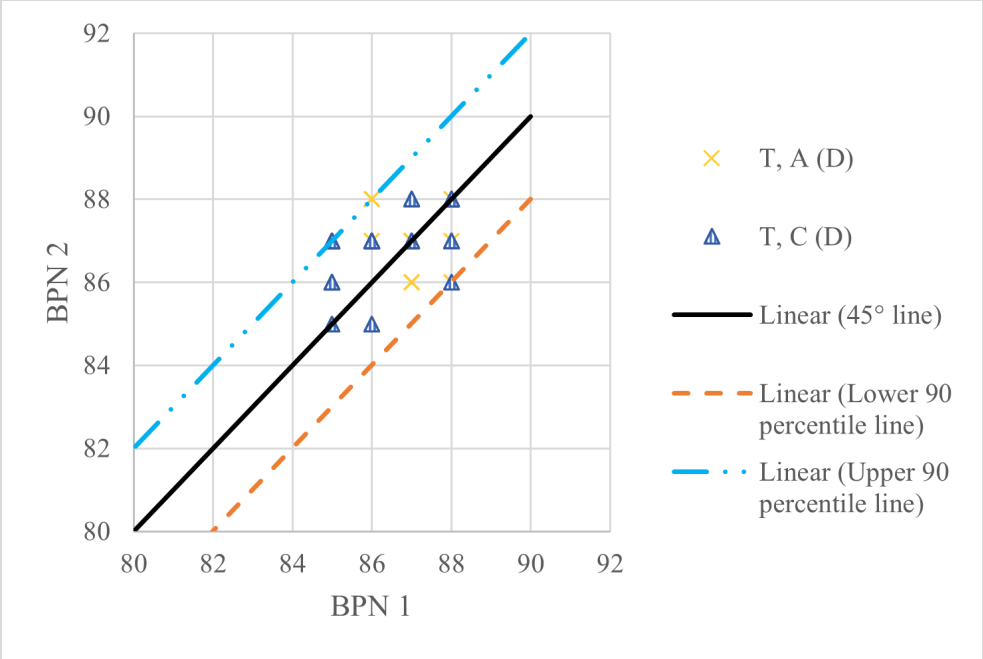

Figure 3.7: Example comparison of BPN values for High Performance Tape (T) in dry (D) conditions using TSR. Note: BPN average values, $n = 6$ replicates.

A comparison of the average PSR and TSR values for T for all three surface conditions (D, W, I) for the two units on an asphalt sample is shown in Figure 3.8. As can be observed from the results, the two units provide consistent values in all cases. The interval lines at the top of the bars in the graph represent the one standard deviation for each case, reflecting a low variability between repeated measurements, and at comparable levels for both units.

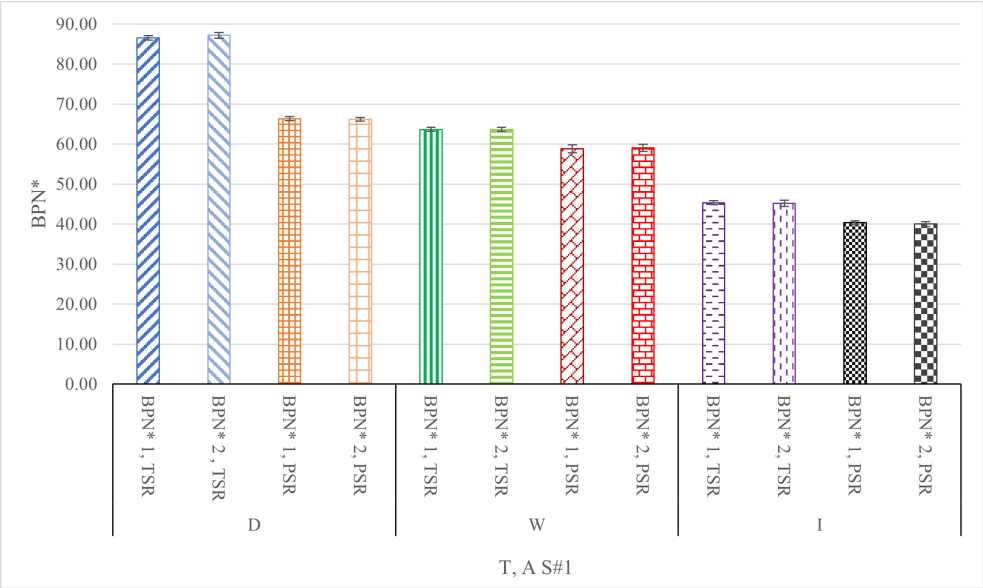

Figure 3.8: Effect of the testing device on TSR & PSR on T(A) based on average values. Note: T, AS1 = High-Performance Tape on Asphalt Sample 1; BPN* = average values with $n = 6$ replicates; BPN*1 = average values for BPT unit 1.

Table 3.6 presents the results of the statistical analysis using paired t-test, Analysis of Variance (ANOVA), and Multivariate Analysis of Variance (MANOVA) on all 216 BPN observations. The measurements obtained between the two BPT units were first paired for each pavement marking material for paired t-test analysis. Both asphalt and concrete samples were used in the analysis. As can be observed from Table 3.6, there was no statistical difference in either the TSR and/or PSR measurements obtained between the two BPN units on measurements obtained on each of the three pavement markings (P, Th, T). Similarly, when the measurements in each of the surface conditions (D, W, I) were paired for the two BPT units, no significant difference between them was statistically observed. This was the case for each of the TSR and PSR measurements at the corresponding surface conditions (D, W, I). Thus, based on the t-test analysis, the two BPT units statistically provide the same measurements.

In the ANOVA/MANOVA analysis, all 216 BPN observations were used. In these anal-

yses, the TSR values for both units at any pavement marking material and surface condition were compared. Similarly, the PSR values between the two units were examined as well. The ANOVA/MANOVA statistical analysis confirmed as well that both BPT units provide statistically the same response, for each of the three pavement markings (P, Th, T) and at each surface condition (D, W, I). Thus, the use of alternative BPT units with the same design specifications provides consistent measurements at any of the pavement marking materials examined in this study and surface conditions.

Table 3.6: Statistical Results of BPN Measurements Between Two BPT Units on Pavement Marking and Surface Conditions

Analysis	**Pavement Markings**	**Variables**	**Observations**	**Outcome**
Paired t-test	P/A/C Th/A/C T/A/C	TSR PSR BPN 1(D) vs BPN 2(D) BPN 1(W) vs BPN 2(W) BPN 1(I) vs BPN 2(I)	72	NS
ANOVA/MANOVA	APM	BPN 1(TSR) vs BPN 2(TSR) BPN 1(PSR) vs BPN 2(PSR)	216	NS

Note: Th/A/C = Thermoplastic on Asphalt and Concrete; T/A/C = High-Performance Tape on Asphalt and Concrete; P/A/C = Preformed Thermoplastic on Asphalt and Concrete; APM = All Pavement Markings with All Surface Conditions; NS = Differences not Statistically Significant.

3.5.2 Operator Effects on BPT Measurements

The effects of using a different operator with the BPT were examined next. Figure 3.9 provides an example of the TSR and PSR readings measured by two operators on preformed thermoplastic markings applied to asphalt and concrete surfaces. The first operator had extensive experience with BPT testing, whereas the second one was newly trained with limited experience. Figure 3.9 shows that the BPN values of TSR and PSR are very close for the two operators, with little variation in all samples. The error bars, as a representation of testing variability, are very small, indicating that there is little operator bias on the BPT measurements. This consistency over asphalt and concrete samples reflects the reliability of the skid and slip resistance measurements process since it is significantly influenced by operators.

The statistical comparison of the operator's influence using a paired t-test analysis is presented in Table 3.7. The p-values from all the comparisons are well above the level of significance ($\alpha = 0.05$), confirming the fact that no statistically significant differences exist between the measurements from Operator 1 and Operator 2 for both TSR and PSR. That consistency across surface type and measures of skid and slip resistance underlines the reliability of BPN measurements, irrespective of operator experience.

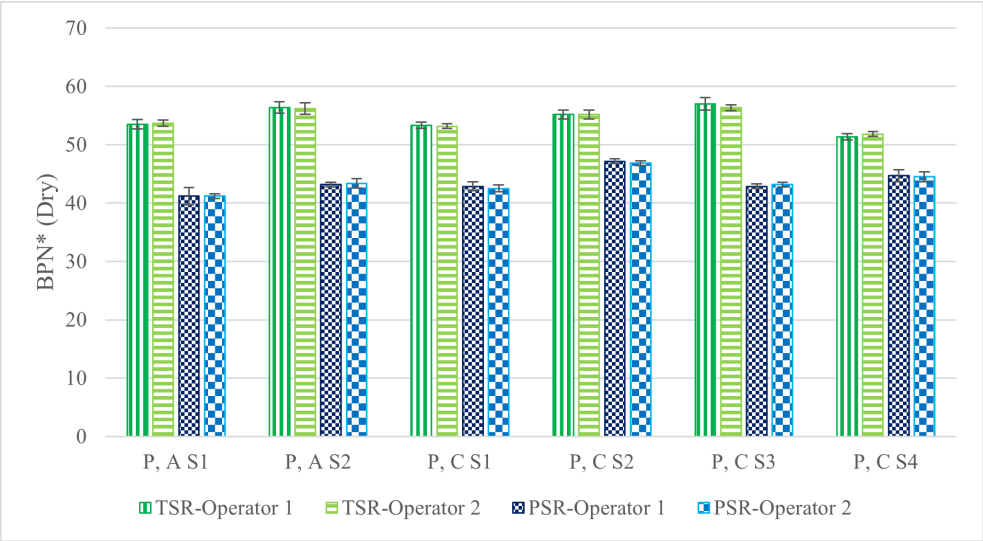

Figure 3.9: Impact of the Operator on TSR and PSR Measurements for Preformed Thermoplastic. *Note: BPN*2 = Average British Pendulum Number (Unit 2), with $n = 6$ replicates; Variability bars represent $\pm s$; Sample details: 2 preformed thermoplastic samples on asphalt and 4 on concrete.*

Table 3.7: Paired t-Test Assessing Operator Impact on TSR and PSR for Preformed Thermoplastic

Surface Type and Location	**TSR-BPN 2 (Dry) Operator 1 vs 2: p-Value**	**PSR-BPN 2 (Dry) Operator 1 vs 2: p-Value**
P, A S1	0.695	1.000
P, A S2	0.611	0.695
P, C S1	0.363	0.363
P, C S2	1.000	0.175
P, C S3	0.175	0.175
P, C S4	0.203	0.771

Note: Confidence level = 95% ($\alpha = 0.05$); Individual sample values are analyzed; Each sample includes 6 replicates per operator ($n = 6$); H_0: $\mu_{\text{difference}} = 0$; H_1: $\mu_{\text{difference}} \neq 0$; Samples: 2 preformed thermoplastics on asphalt, and 4 on concrete.

3.5.3 Pavement Surface Materials Characteristics & Fourier Transform Analysis

In an effort to better understand the pavement surface materials' friction response for the selected markings, microscopic imaging on new and used P, T, and Th markings, along with Fourier Transform analysis on consecutive measurements, was performed.

3.5.3.1 Microscopic Assessment of Pavement Markings

The surface microscopic characteristics of P, T, and Th markings were examined in an effort to gain an understanding of their surface features that eventually may affect and contribute to slip and skid resistance (see Figure 3.10). It was also of interest to eventually attest and/or document the reasons for skid and slip resistance reduction because of the use (i.e., wear and tear) of the pavement marking materials.

The microscopic investigation has provided adequate information about wear mechanisms and functional properties in these markings, as observed at 50x magnification (a–c, g–i) and 250x magnification (d–f, j–l). New samples of P pavement marking display a uniform distribution of embedded glass beads that are not only important to the initial reflectivity but also to the frictional properties [97, 98]. The worn samples g and j show significant detachment of beads and wear of the surface, producing a fast reduction in properties (i.e., reflectivity and friction resistance), hence identifying limitations in regards to their durability and surface wearing characteristics. P pavement markings generally use larger glass beads that are usually of Type 4 (the largest specified beads per TT-B-1325C, sized 0.84–1.68 mm for Type A and 0.59–1.19 mm for Type

B, best suited for use in high-build acrylic binder with at least 25–30 mils wet film thickness; performance is poor if under-embedded in thinner films), which could also explain the reason for its bead detachment and thus fast loss of surface characteristics. It therefore explains the rapid loss in BPT values of P marking observed with the fast wear and tear with their use [99, 100].

On the other hand, T markings show higher friction performance over time by retaining high amounts of glass beads even in used samples (h, k). This corresponds to higher BPT values, providing better long-term performance in regards to surface friction. New samples show a well-distributed bead structure (b, e), and the used samples can retain their frictional properties after a certain level of wear. Unlike the P markings, T markings use smaller and thinner beads that are associated with higher durability and friction. This might be the reason for their better performance in the long term as well as wear resistance, observed in the case of T markings [99]. Most likely, special material formulations or bead bonding mechanisms proprietary to T markings are the most plausible explanations for such enhanced resistance over a longer period of time and/or traffic.

Th-type markings, without glass beads, rely on their intrinsic surface texture for friction and reflectivity (c, f). This surface texture was worn significantly in used samples (i, l) by smearing and loss of surface definition that substantially reduces their functionality over time. Limited durability without glass beads makes them not as effective as the P and T markings in many environments where consistent friction and reflectivity may be needed. This trend is further supported by the BPN values summarized in Table 3.8, which show clear reductions in both TSR and PSR values for used samples.

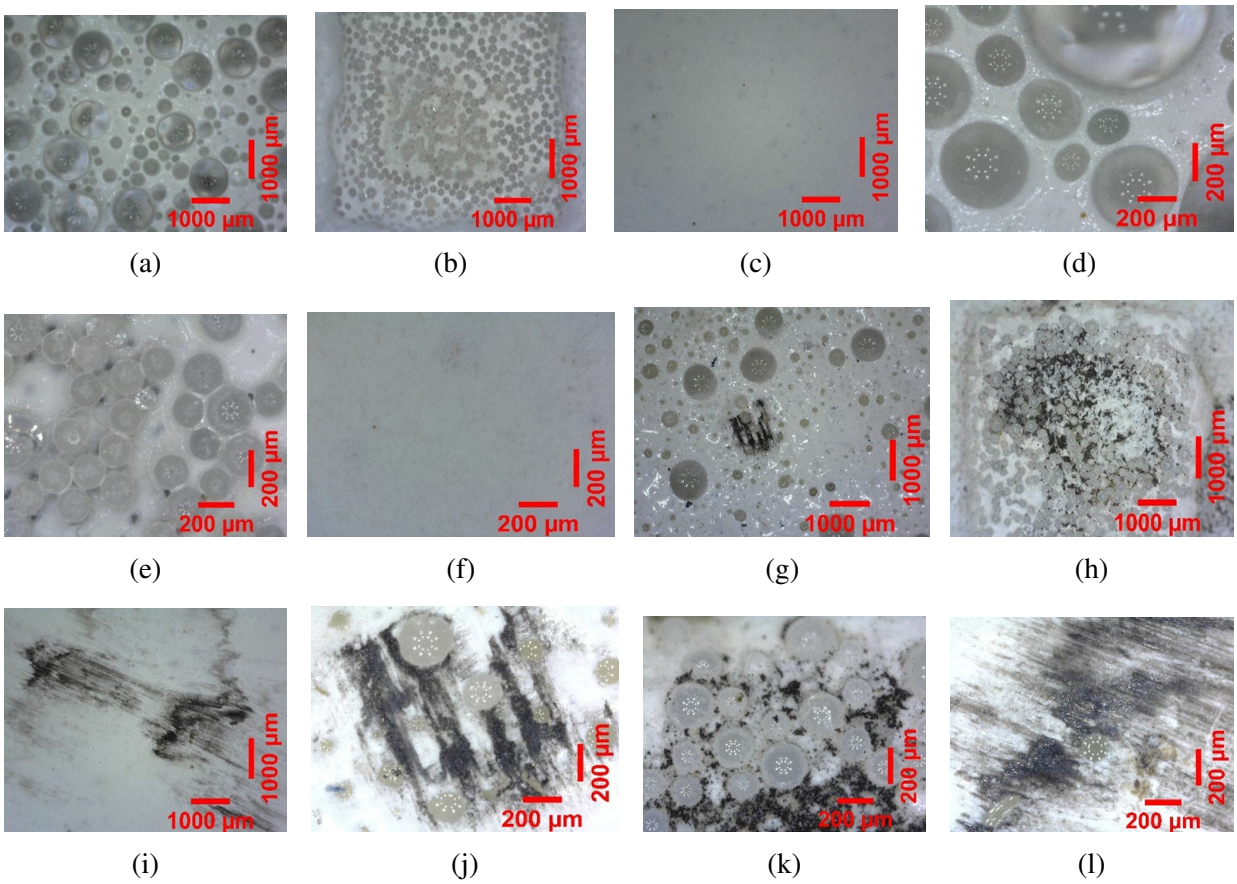

Figure 3.10: Digital Microscopic Images of New (a–f) and Used (g–l) Pavement Markings at 50x (a–c, g–i) and 250x (d–f, j–l) Magnifications for P- (a, d, g, j), T- (b, e, h, k), and Th- (c, f, i, l) Markings

Table 3.8: BPN Summary for New vs Used Pavement Markings

Pavement Marking	BPN	Statistic	New-BPN1 (D)	Used-BPN1 (D)
T, A	TSR	Mean CV%	86.5 0.63	71.000 5.194
	PSR	Mean CV%	66.33 0.78	58.000 2.438
P, A	TSR	Mean CV%	54.667 5.131	49.167 0.830
	PSR	Mean CV%	43.833 1.717	39.333 2.076
Th, A	TSR	Mean CV%	67.167 1.741	59.000 1.857
	PSR	Mean CV%	46.500 3.534	43.833 4.875

Note: BPN average values, $n = 6$ replicates; 72 tests per used sample (6 replicates × 2 devices × 3 conditions: D, W, I × 2 pads: TSR, PSR).

3.5.3.2 Fourier Transform Analysis

The aim of the FFT analysis was to eventually better understand the friction resistance of the alternative pavement markings in regard to micro and macrotexture (i.e., parallel to "adhesion" and "hysteresis" pertinent to those reported from the tire–pavement surface interaction phenomena for traditional paving mixtures and materials).

Figure 3.11 presents the amplitude spectra with FFT of TSR and PSR measurements over P, T, and Th pavement surface materials. The discussion that follows will give a feeling about those dominant frequency components that generate macrotexture due to low frequency (¡0.1Hz) as well as microtexture corresponding to high frequency (¿ 0.5Hz). In all, there are 16 consecutive measurement locations for each pavement type with three replicates in each location and two BPT pads, amounting to a total of 288 observations. All measurements of TSR and PSR values

were performed under dry conditions in order to comprehensively capture the characteristics of the surface texture.

The FFT analysis followed in this research is meant to transform signals into frequency domains for the analysis and identification of sinusoidal wave components and dominant wavelengths, which define pavement texture [93]. For accuracy, detrending was done by subtracting the mean, where detrending by mean takes off low-frequency drift—its DC component. The same is in line with suggestions by Bertocci et al [101] so as not to introduce artifacts into it by moving average removal. The FFT analysis would, therefore, give the most reliable decomposition of the surface texture profile into frequency components.

In the case of pavement surfaces type P, as seen in Figures 3.11a and 3.11b and summarized in Table 3.9, the clear low-frequency peak in both TSR and PSR spectra below 0.1 Hz with amplitudes around 1.2 mm for TSR and 0.9 mm for PSR shows macrotexture as the main cause for increased hysteresis and inferred potential for improved wet traction, as macrotexture enhances water drainage under wet conditions, which helps improve pavement skid resistance [102].

In pavement surfaces T, Figures 3.11c and 3.11d and Table 3.9 show macrotexture also appeared at somewhat lower amplitudes of low frequencies (about 0.5 mm for TSR and 0.3 mm for PSR), borderline between macro and microtexture, ensuring a more balanced performance across both hysteresis (macrotexture) and adhesion (microtexture) contributions under varying surface conditions.

In the case of Th pavement surface (Figures 3.11e and 3.11f and Table 3.9), the TSR spectra confirmed texture amplitudes ($\approx$0.15 mm) that are within the microtexture range, and they represent relatively finer scale textures supporting better adhesion in dry conditions. On the other hand, PSR spectra for Th (Figure 3.11f) show a strong low-frequency peak ($\approx$1.00 mm), re-

flecting notable macrotexture contributions supplementing the microtexture of this surface and, therefore, making it suitable for a wide range of surface conditions, such as dry and wet, with both skid and slip resistance considerations.

These results further support the distinction between adhesion-based friction mechanisms (microtexture-dominated) and hysteresis-based friction mechanisms (macrotexture-dominated), in line with phenomena typically observed in conventional tire–pavement interactions (see Table 3.9).

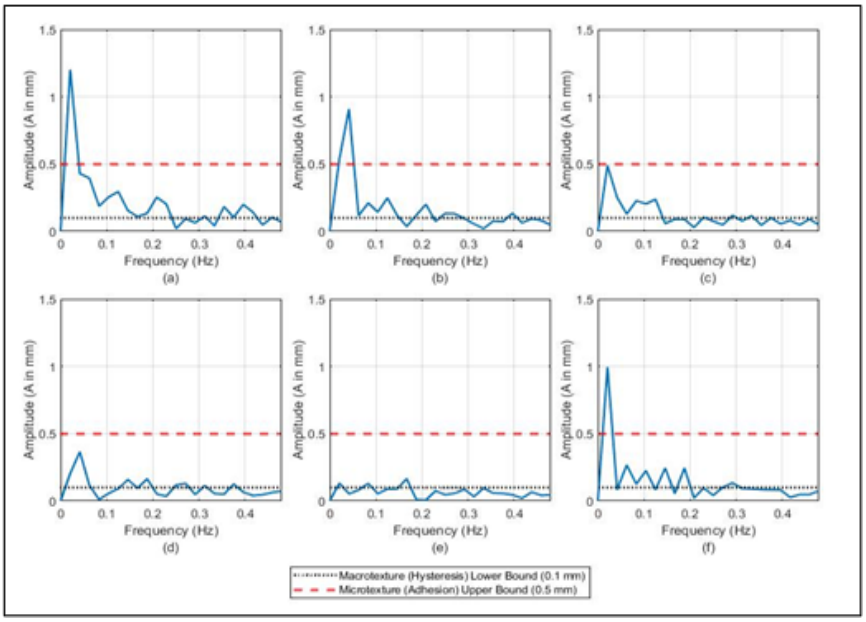

Figure 3.11: Fast Fourier Transform (FFT) Analysis for: (a) TSR-P, (b) PSR-P, (c) TSR-T, (d) PSR-T, (e) TSR-Th, and (f) PSR-Th.

Table 3.9: Pavement Texture and Friction Mechanism Classification (FFT-Based)

Pavement Type	Signal (TSR/PSR)	Fig.	Peak Amplitude (A)	Texture Type	Dominant Friction Mechanism
P	TSR	(a)	∼1.2 mm	Macrotexture	Primarily Hysteresis
	PSR	(b)	∼0.9 mm	Macrotexture	Primarily Hysteresis
T	TSR	(c)	∼0.5 mm	Micro + Macro-texture	Hysteresis + Adhesion
	PSR	(d)	∼0.3 mm	Micro + Macro-texture	Hysteresis + Adhesion
Th	TSR	(e)	∼0.15 mm	Microtexture	Primarily Adhesion
	PSR	(f)	∼1.0 mm	Macrotexture	Primarily Hysteresis

3.6 Summary & Conclusions

This study examined the response of BPT in regards to vehicle tire friction and pedestrian slip resistance. Since agencies and contractors may use their own units for surface friction evaluation, two BPT units with similar design specifications were considered. The study results indicated that the two alternative units provided comparable measurements for any pavement marking material (P, Th, T) and surface condition (D, W, I) in regard to PSR and TSR. Furthermore, testing variability was significantly low with a CV% ranging between 0.6% to 1.67%. Furthermore, based on the statistical analysis, the paired t-test analysis confirmed that the two BPT units statistically provide the same measurements for each case. Similarly, the ANOVA/MANOVA analysis confirmed as well that both BPT units provide statistically the same response, for each of the three pavement markings (P, Th, T) and at each surface condition (D, W, I).

The microscopic surface imaging and Fourier transform analysis provided valuable insights into the contribution of micro and macrotexture of the alternative pavement marking materials to

surface friction as well as the effects of "wear and tear" in relation to their use. P marking tends to rely on large beads and thus their frictional properties degrade fast due to their quick detachment from the pavement marking surface. T markings show higher friction performance over time by retaining high amounts of smaller size glass beads, corresponding to higher BPT values and better long-term performance in regards to surface friction. The Th markings rely on their intrinsic surface texture for friction and thus have lower and reduced friction over time. Finally, the FFT analysis provided a better understanding of the micro and macro contribution of these pavement markings on pavement surface friction and slip resistance.

The findings of this study provided significant insights into the evaluation of PSR and TSR on crosswalk pavement markings. The need to consider pedestrian slip resistance in conjunction to vehicle skid friction during Quality Assurance (QA), routine monitoring and/or acceptance testing and specifications, has generated a national interest in this study and the research findings with the AASHTO Research Advisory Committee (RAC) recently awarding this research project with the 2025 "Sweet 16 High Value Research Award." Due to the study's importance in regards to safety, several states are expected to adopt the recommendations for assessing such pavement markings in critical locations for safety.

Chapter 4: AIMS Analysis for Pavement Markings

4.1 Overview

The Aggregate Image Measurement System (AIMS) is an advanced imaging and analysis instrument utilized for quantifying the surface texture and shape characteristics of aggregates and pavement surfaces. Initially used for the measurement of the morphological features of aggregate particles, the AIMS instrument was later adapted for flat surface imaging, including asphalt slabs and pavement core samples. The system includes a high-resolution digital camera, programmable illumination, and automated rotation and scanning stages. By using image capture under controlled lighting, AIMS offers objective quantification of angularity, shape, and texture through the use of computerized algorithms [103–105]. Figure 4.1 shows the AIMS system setup used in this study.

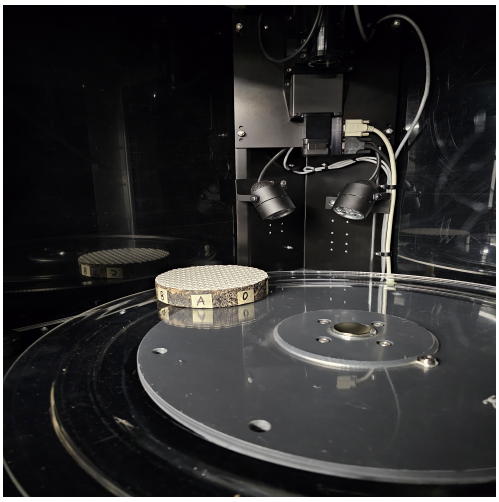

Figure 4.1: AIMS setup with asphalt core sample with tape marking on top.

In this chapter, AIMS is used to analyze the microtexture of asphalt cores which have or do not have pavement markings. The test samples are asphalt-only surfaces (AS#2), preformed thermoplastic (PS#2), tape markings (TS#2), and thermoplastic markings (ThS#2). AIMS provides high-accuracy detection of microtexture, three parameters of texture measure—Root Mean Square (RMS), Mean Profile Depth (MPD), and Mean Texture Depth (MTD)—being examined for correlation with friction values measured such as British Pendulum Number (BPN). The resolution and flexibility of AIMS are perfect for the examination of the surface quality of the pavement marking, which is very important in friction and pedestrian slip resistance.

4.2 Literature Review

The development of AIMS was a significant advance in image-based surface analysis. Masad and Fletcher [103] introduced the system as a digital alternative to traditional, aggregate tests. By analyzing particle silhouettes and grayscale surface images, AIMS computes indices of angularity, form, and texture by applying mathematical algorithms. To analyze surface texture, the system employs discrete wavelet transforms for measuring texture energy at various scales [103, 106]. The wavelet-based texture index is calculated as:

$$\text{Texture Index}_n = \frac{1}{3N} \sum_{i=1}^{3} \sum_{j=1}^{N} D_{i,j}(x,y)^2 \tag{4.1}$$

where n is the degree of decomposition, N is the number of coefficients in the texture image, i refers to the three directional detail images (horizontal, vertical, diagonal), and (x, y) refers to the coefficient position.

The form of particles is also quantified by computing the radial deviation from the particle

centroid. The form index is computed as:

$$\text{Form Index} = \sum_{\theta=0}^{360-\Delta\theta} \frac{|R_{\theta+\Delta\theta} - R_\theta|}{R_\theta} \tag{4.2}$$

where R_θ is the radius at angle θ, and $\Delta\theta$ is the angular increment, typically 4° [103].

Designed for aggregate particles, these methods have been successfully applied to the analysis of flat pavement surfaces. Mahmoud and Ortiz [107] and Aldagari [108] utilized AIMS in aggregate polishing resistance monitoring, with texture indices decreasing with mechanical wear. These alterations were strongly correlated with reductions in BPN, validating AIMS as a predictive metric for surface friction loss. Masad et al. [103, 104] extended this application to asphalt mixtures, illustrating the value of the retention of texture after polishing for extended skid resistance. The research validated that rising AIMS texture indices relate to enhanced field friction performance.

Rezaei et al. [105] advanced AIMS methodology further by applying it to flat pavement cores, utilizing height data to derive macrotexture indices such as MPD and MTD. Rezaei et al. [105] furthered this methodology with additional statistical formulations, showing that RMS depth is a more encompassing indicator of surface variation than MPD, which considers only peak values. The following equations are the formulations being used in current surface texture evaluations.

Root Mean Square (RMS) texture depth is given as:

$$\text{RMS} = \sqrt{\frac{\sum_{i=1}^{n} h_i^2}{n}} \tag{4.3}$$

where h_i is the height after slope correction for each measurement, and n is the number

of measurements in the segment. RMS uses all the data points, unlike MPD, which selects and averages peak values, providing a more complete description of surface texture [105].

As recommended by Rezaei et al. [105], for finding the Mean Profile Depth (MPD), the highest peak in the two half-segments is identified. The Mean Segment Depth is then found by averaging the two peak values. Once the mean segment depths of all eight segments are found, their average is computed to be the MPD of the complete circumferential scan line. The process is in accordance with ASTM E1845–09 standards, MPD is expressed as:

$$\text{MPD} = \frac{1}{n}\sum_{i=1}^{n}\left(\frac{h_{\text{max1}} + h_{\text{max2}}}{2} - h_i\right) \tag{4.4}$$

where h_{max1} and h_{max2} are the two maximum peak heights in two defined profile segments, and h_i is the height at each measuring point in the profile segment [109].

Mean Texture Depth (MTD), which is sometimes used as a substitute for sand patch testing, is derived from MPD or directly from elevation data through:

$$\text{MTD} = \frac{1}{n}\sum_{i=1}^{n}(h_0 - h_i) \tag{4.5}$$

where h_0 is the reference baseline, h_i is the height of position i, and n is the number of data points measured [109]. Alternatively, MTD can be estimated by a regression relation with MPD:

$$\text{MTD} = 0.79 \times \text{MPD} + 0.23 \quad \text{(mm)} \tag{4.6}$$

Although the majority of past applications of AIMS have been on aggregates and asphalt mixtures, its application to pavement markings is unexplored. Poor surface texture marking has

been shown to reduce wet friction significantly because of their smooth nature and absence of microtexture [10, 110, 111]. Pavement markings that don't have texture or wet retroreflective properties can make it hard to see at night when it's wet and under headlights, and they can also make it harder to get traction, especially on smooth marking materials. This is mostly based on BPN and doesn't include high-resolution surface profiling [110, 112, 113].

Recent studies, such as Kouchaki [114], have been concerned with the use of imaging and laser scanning to measure surface roughness and texture profiles, validating the use of AIMS as a valid laboratory-based alternative. Kováč and Čelko [115] drew attention to the need to align national pavement friction measurement practices with European standards through the adoption of standardized measures such as the International Friction Index (IFI), further consolidating the applicability of consistent and comparable skid resistance evaluation practices.

By integrating these techniques, this chapter employs AIMS to compare surface texture differences of four types of pavement markings on asphalt cores. The use of RMS, MPD, and MTD indices derived from high-resolution imaging offers a quantitative foundation for investigating slip and skid potential.

4.3 Geometry of Marking Materials Used

All specimens used in the AIMS testing are asphalt gyratory-compacted samples with a fixed diameter of 150 mm. The heights differ due to variations in the original specimen preparation, as summarized in Table 4.1.

Table 4.1: Dimensions of Pavement Markings Used in AIMS

Asphalt Cylinder	Diameter (mm)	Height (mm)
A, S#2	150	37.88
Th, S#2	150	32.20
T, S#2	150	32.40
P, S#2	150	25.80

4.4 Measurement Setup and Surface Preprocessing

To capture surface texture across various orientations, each core sample was scanned in four radial directions (AA, BB, CC, and DD), spaced 45° apart. The directional measurement setup is illustrated in Figure 4.2, reproduced from Rezaei et al. [105].

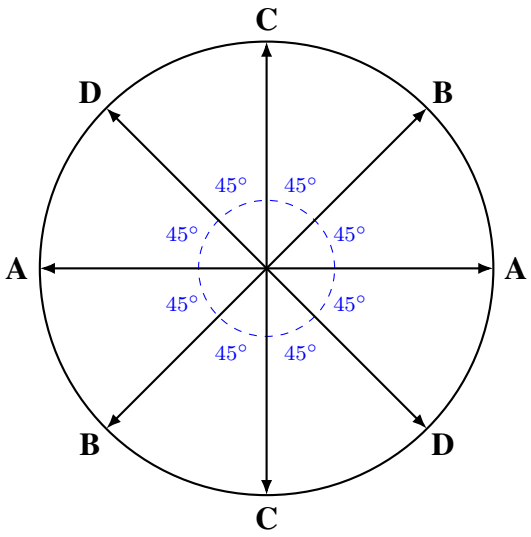

Figure 4.2: Directional scan layout at 45° intervals used in AIMS texture analysis

The surface profile data collected from each direction was preprocessed to eliminate bias caused by curvature or slope across the core height. This was achieved by fitting a linear baseline to each profile and subtracting it from the data, effectively flattening the surface for fair comparison. Figures 4.3 and 4.4 show the height profiles before and after slope correction.

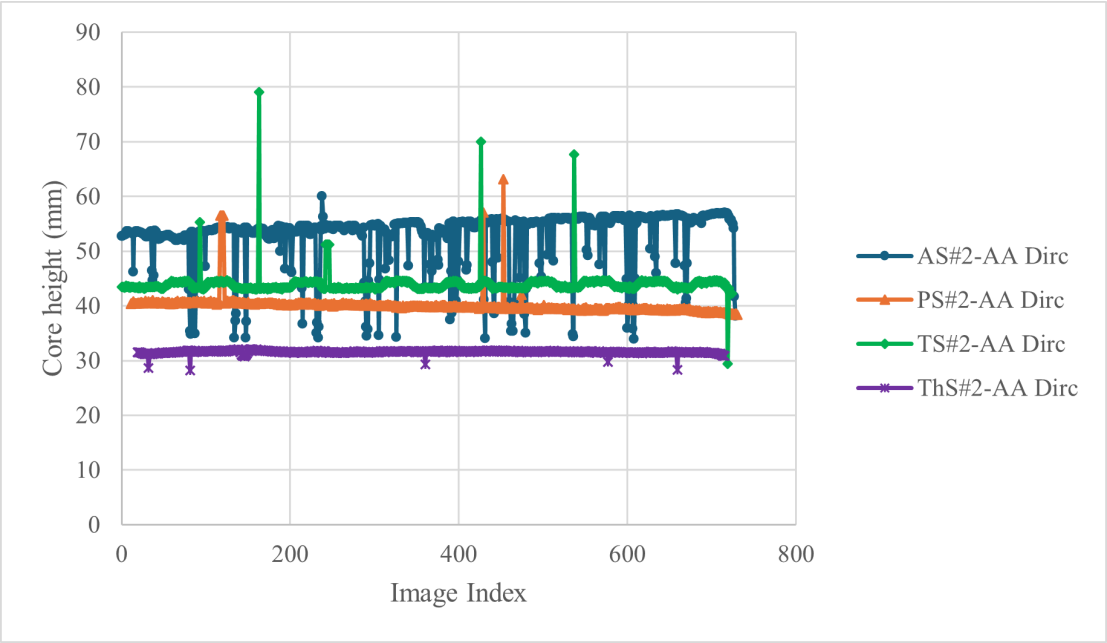

Figure 4.3: Core Height Variations of Markings.

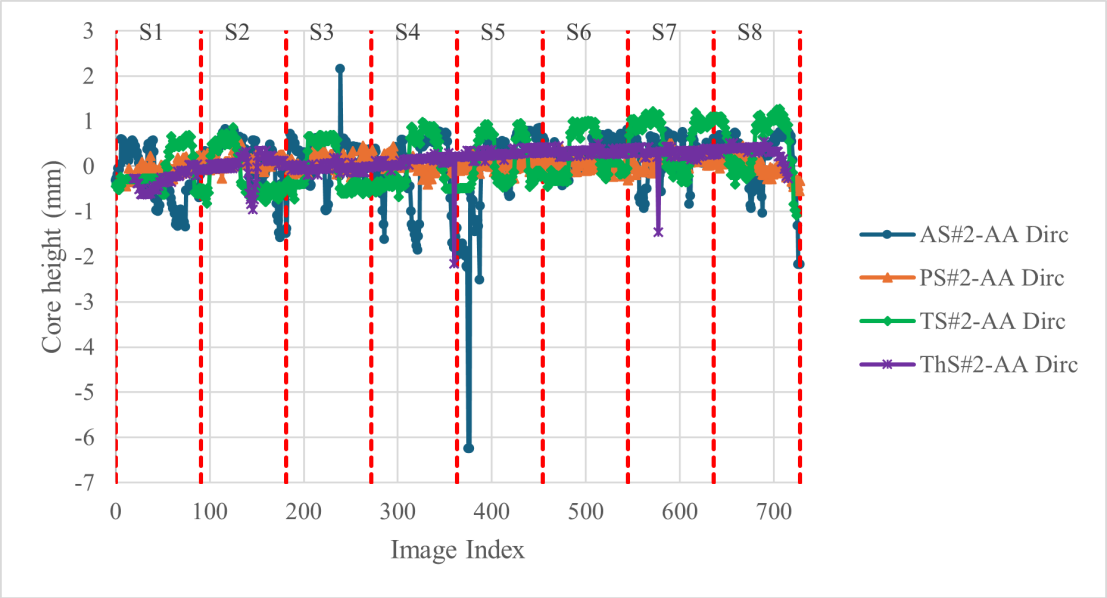

Figure 4.4: Core Height Variations Using Zero-Based Data.
Note: Zero-based data preprocessing parameters — Interval = 0.2 mm; Span Length = 150 mm; Magnification = 15.80×; Segments = S1–S8.

4.5 Texture Metric Definitions and Equations

The texture metrics used in this study include Root Mean Square (RMS), Mean Profile Depth (MPD), and Mean Texture Depth (MTD), which were previously defined in the literature review. The following equations, originally presented in Section 4.2, are used for analysis:

Table 4.2: Texture Metrics Used in This Study and Their Corresponding Equations

Metric	**Corresponding Equation**
RMS	Equation 4.3
MPD	Equation 4.4
MTD	Equation 4.5

4.6 Comparative Texture Analysis of Pavement Markings

The RMS, MPD, and MTD values for four core types (AS, PS, TS, ThS) are shown in Table 4.3. Each value represents the mean over four directional scans.

Table 4.3: RMS, MPD, and MTD Comparison for All Markings

Sample	Scan Direction	RMS	MPD	MTD
AS#2	AA	0.729	0.774	1.616
	BB	0.918	0.748	0.864
	CC	0.809	0.573	0.897
	DD	1.043	0.866	1.802
	AVG ± *SD*	0.875 ± 0.118	0.740 ± 0.106	1.295 ± 0.420
PS#2	AA	0.172	0.332	0.449
	BB	0.237	0.489	0.759
	CC	0.257	0.469	0.974
	DD	0.235	0.459	0.713
	AVG ± *SD*	0.225 ± 0.032	0.437 ± 0.062	0.724 ± 0.187
TS#2	AA	0.599	0.802	1.151
	BB	0.544	0.724	1.080
	CC	0.517	0.769	1.031
	DD	0.525	0.657	0.866
	AVG ± *SD*	0.546 ± 0.032	0.738 ± 0.054	1.032 ± 0.105
ThS#2	AA	0.298	0.310	0.410
	BB	0.243	0.304	0.315
	CC	0.340	0.263	0.678
	DD	0.469	0.549	0.542
	AVG ± *SD*	0.337 ± 0.083	0.357 ± 0.113	0.486 ± 0.137

4.7 RMS, MPD and MTD Trends

The results indicate that A-S#2 had the highest surface texture values in all the parameters with RMS at 0.875 mm, MPD at 0.740 mm, and MTD at 1.295 mm, as shown in Figure 4.5. The second was T-S#2 with relatively high and consistent values. Th-S#2 was third with RMS at 0.337 mm, which is slightly greater than that of P-S#2 at 0.225 mm. However, P-S#2 had higher MPD and MTD values (0.437 mm and 0.724 mm, respectively) than Th-S#2, whose MPD and MTD values were 0.357 mm and 0.486 mm, respectively.

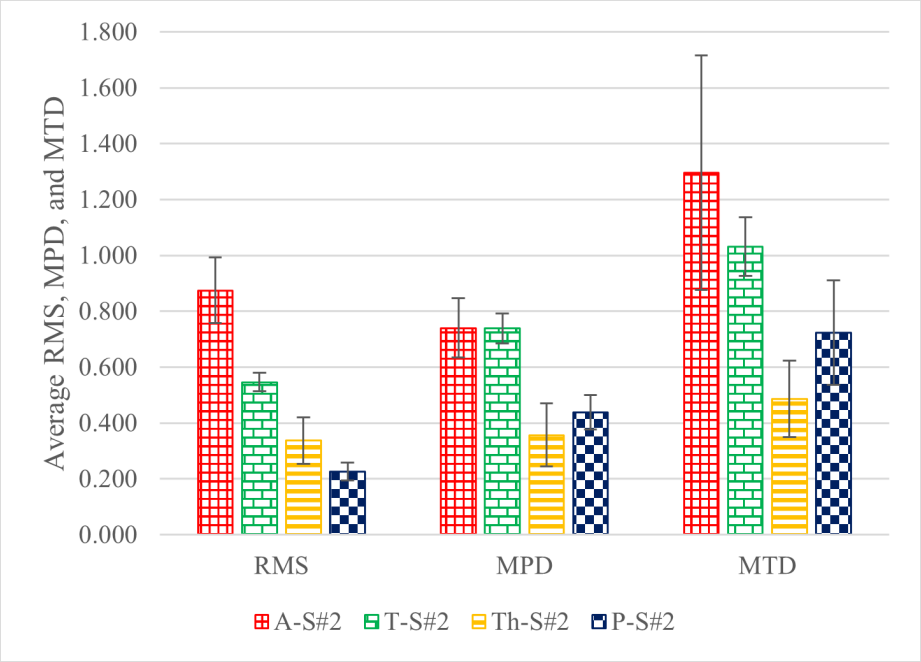

Figure 4.5: Average RMS, MPD, and MTD values for all samples with standard deviation bars.

As mentioned in Figure 4.6, A-S#2 and Th-S#2 were directionally sensitive, as RMS tended to rise from AA to DD. T-S#2 and P-S#2, on the other hand, presented uniform RMS values between directions, and therefore more uniform surface textures and less directional deviations.

The AIMS-derived texture trends generally compared with the BPT-determined friction for the materials tested in both systems (T-S#2, Th-S#2, and P-S#2), as illustrated in Figure 4.7. T-S#2, having the highest RMS, also had the highest BPN values under dry condition in BPT testing. Th-S#2 had higher RMS than P-S#2, and likewise exhibited higher BPN values. These findings confirm that the BPN values follow the same trend as the RMS measurements, supporting the agreement between microtexture and slip/skid resistance and affirming that BPT outcomes agree with the objective texture measures provided by AIMS.

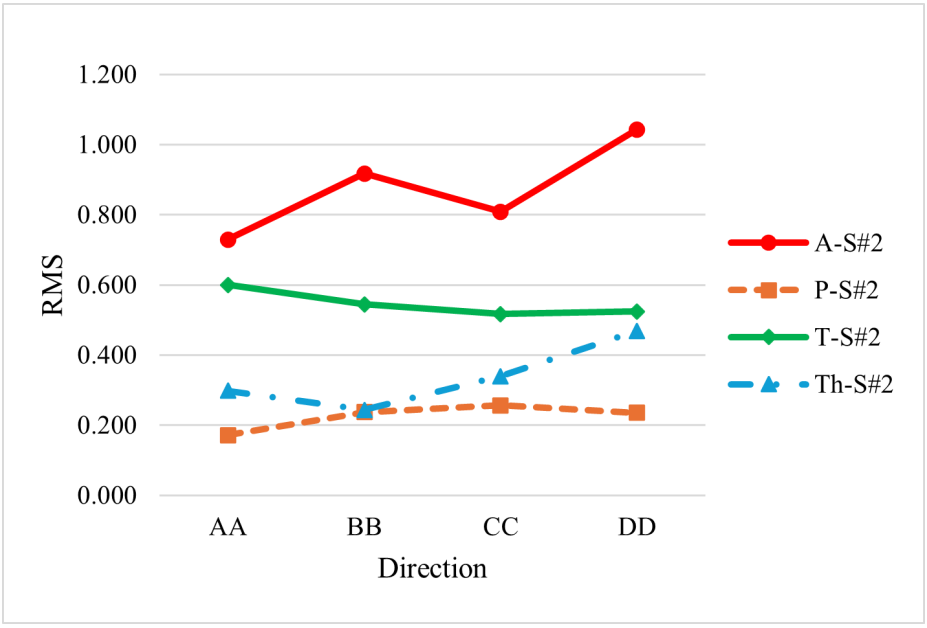

Figure 4.6: Directional variation in RMS values by AIMS scanning lines (AA to DD) for each material.

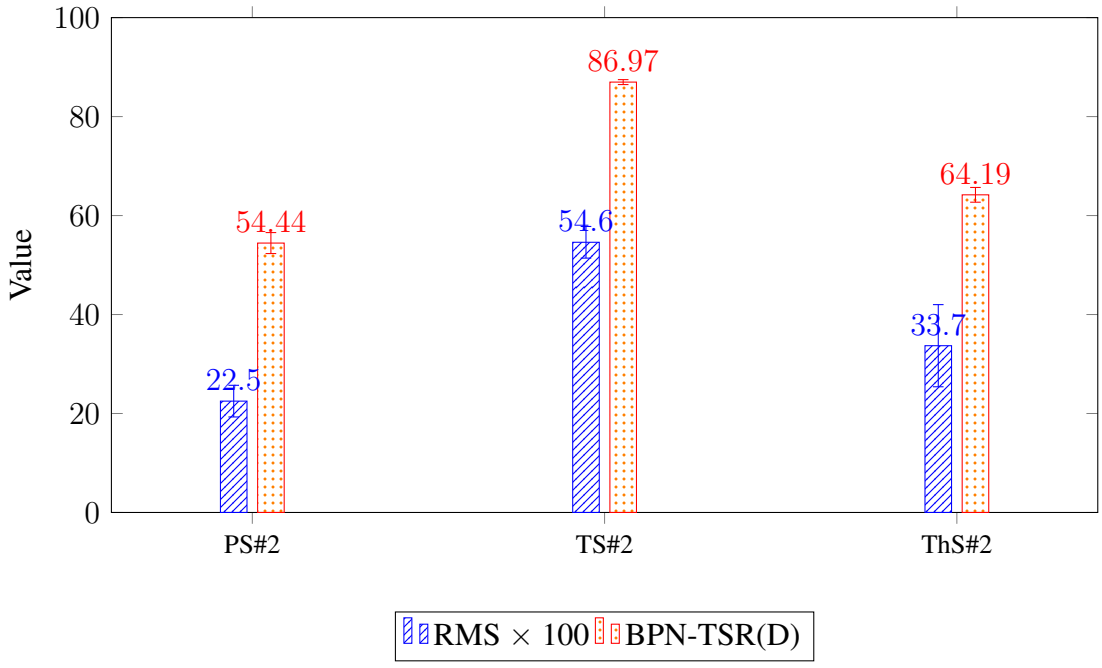

Figure 4.7: Comparison of scaled RMS ($\times 100$) and BPN-TSR(D) values with standard deviations for PS#2, TS#2, and ThS#2. *Note:* RMS average values are based on a single sample tested in four radial directions ($n = 4$; see Table 4.3), while BPN-TSR(D) averages are based on 18 samples with six replicate measurements per sample (see Figure 2.5).

4.8 Correlation Between Texture Metrics

Regression analyses revealed meaningful linear relationships between the texture parameters. As shown in Figure 4.8, RMS and MPD exhibited a strong positive correlation, with a coefficient of determination of $R^2 = 0.6379$. The data were well-fitted by a simple linear model:

$$\text{MPD} = 0.6001 \cdot \text{RMS} + 0.2706 \tag{4.7}$$

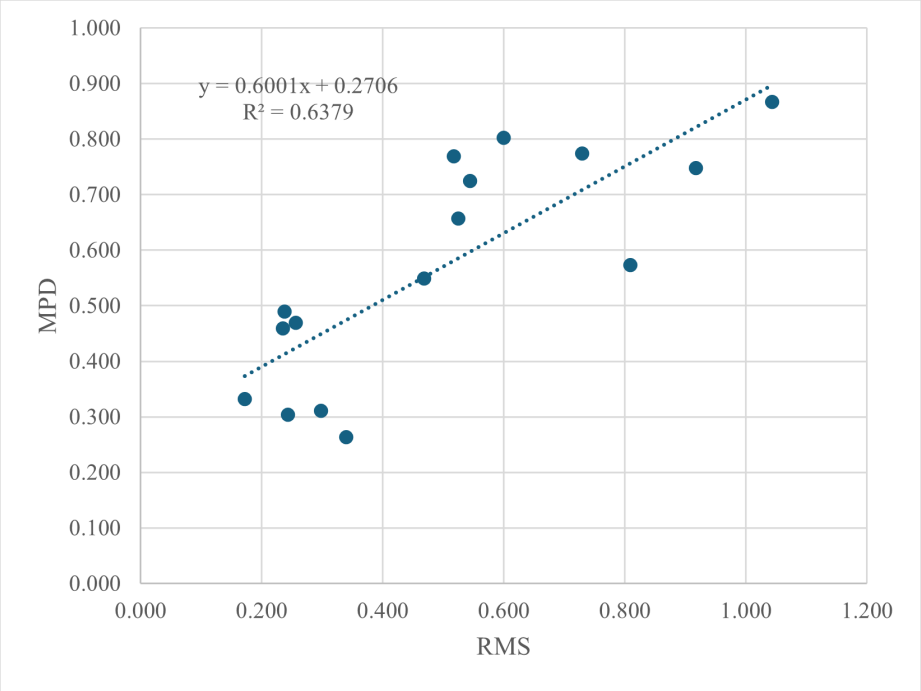

Figure 4.8: Relationship between RMS and MPD.
Note: RMS and MPD exhibit a positive linear relationship ($R^2 = 0.6379$). The fitted regression model is Equation 4.7. Each data point represents one of four scanning directions (AA, BB, CC, DD) for four surface types, totaling $N = 32$ observations.

Similarly, MPD and MTD demonstrated a comparable correlation strength, as shown in Figure 4.9, with a coefficient of determination of $R^2 = 0.6805$. The regression model for this relationship is:

$$\text{MTD} = 1.6652 \cdot \text{MPD} - 0.062 \tag{4.8}$$

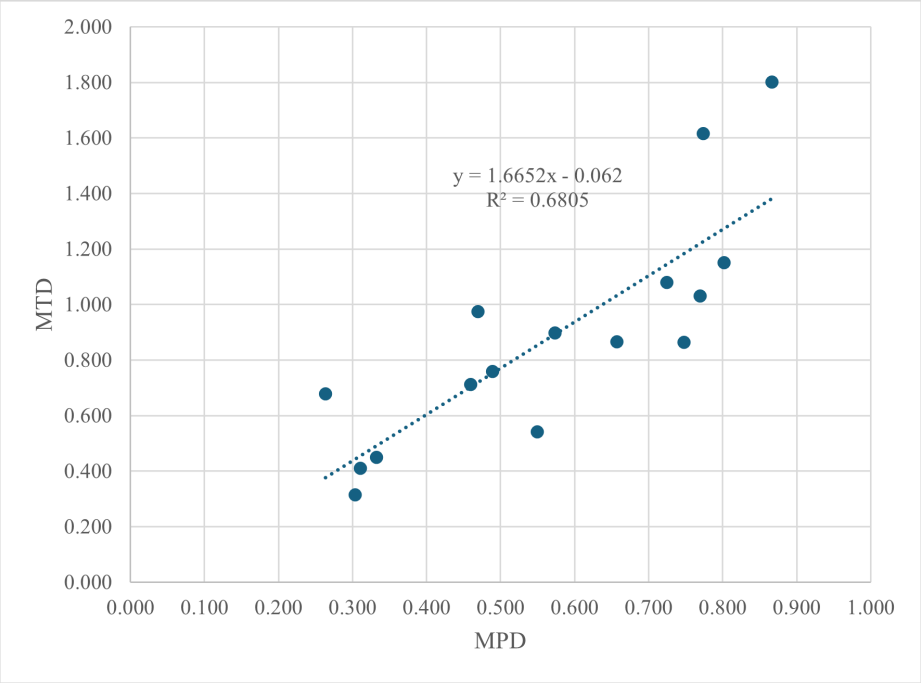

Figure 4.9: Relationship between MPD and MTD.
Note: MPD and MTD exhibit a positive linear relationship ($R^2 = 0.6805$). The fitted regression model is Equation 4.8. Each data point represents one of four scanning directions (AA, BB, CC, DD) for four surface types, totaling $N = 32$ observations.

4.9 Classification Using Quartile Analysis

Quartile-based classification, adapted from Masad et al. [116], was used to assess the surface texture distribution of individual particles within each sample along the BB scanning direction. Table 4.4 presents the 25th (Q1), 50th (Q2, median), and 75th (Q3) percentiles of the texture index values derived from AIMS.

The results show that AS#2 exhibited the highest quartile values, indicating a relatively rough and variable surface. TS#2 and ThS#2 displayed more moderate quartile ranges, reflecting

intermediate textures. PS#2 had the lowest values, suggesting a smoother texture profile. This classification reflects the categorization of particles as low, medium, or high texture based on their relative position within the quartile range.

Table 4.4: Individual Particle Texture Quartiles

Sample	**Q1**	**Q2 (Median)**	**Q3**
AS#2-BB Dirc	580.302	773.298	907.871
TS#2-BB Dirc	97.811	165.425	265.206
ThS#2-BB Dirc	76.148	162.800	270.457
PS#2-BB Dirc	72.866	101.093	129.321

Note: Texture classification is based on Q1–Q3 thresholds. Magnification = 15.80×.

Figure 4.10 presents the box plots of texture variability for each sample. AS#2 exhibited the widest variability and the highest AIMS texture index range, indicating a highly heterogeneous and rough surface. TS#2 and ThS#2 showed similar and moderate texture index values with relatively low variability. PS#2 had the lowest texture index and the narrowest spread, reflecting a smooth and uniform surface.

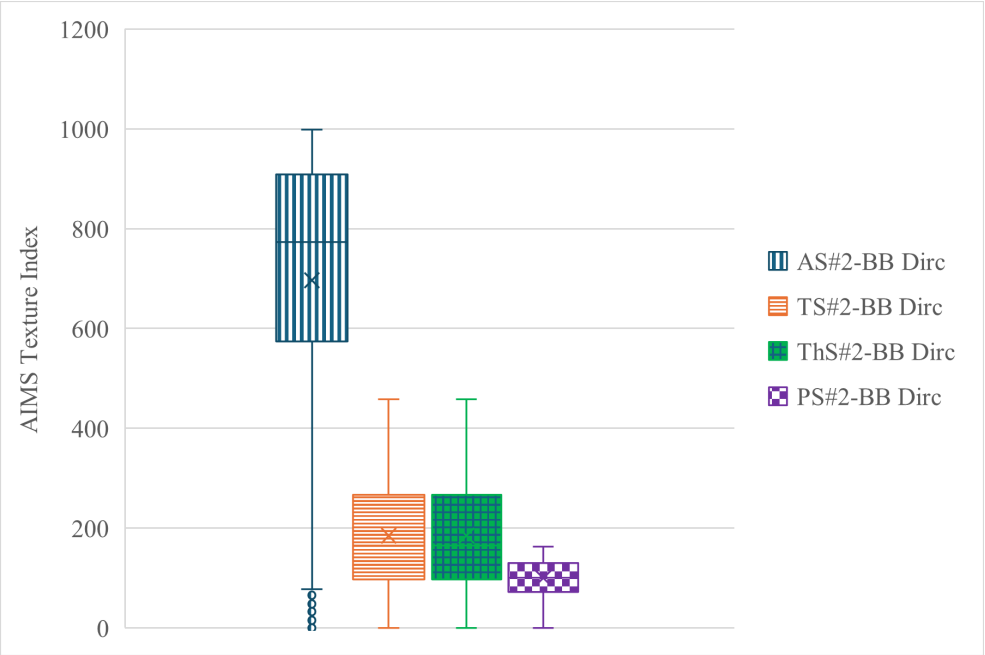

Figure 4.10: Box Plot of Pavement Marking Texture Variability.
Note: AS#2 and TS#2 exhibit high variability; PS#2 is most consistent. Magnification = 15.80×.

4.10 Classification Using Distribution of Texture

This section evaluates the distribution of AIMS texture index values across various pavement markings using the method adapted from [116, 117]. Particles were grouped into three surface roughness categories based on their texture index values: Low ($\leq$ 260), Medium (260–550), and High (550–1000).

As shown in Figure 4.11, AS#2 exhibits the highest surface roughness with a majority of its particles in the high-texture category. In contrast, PS#2, TS#2, and ThS#2 are dominated by low-texture classifications, suggesting more uniform and smoother surfaces. These trends are further supported by the percentage breakdown presented in Table 4.5 and the grouped bar chart in Figure 4.12.

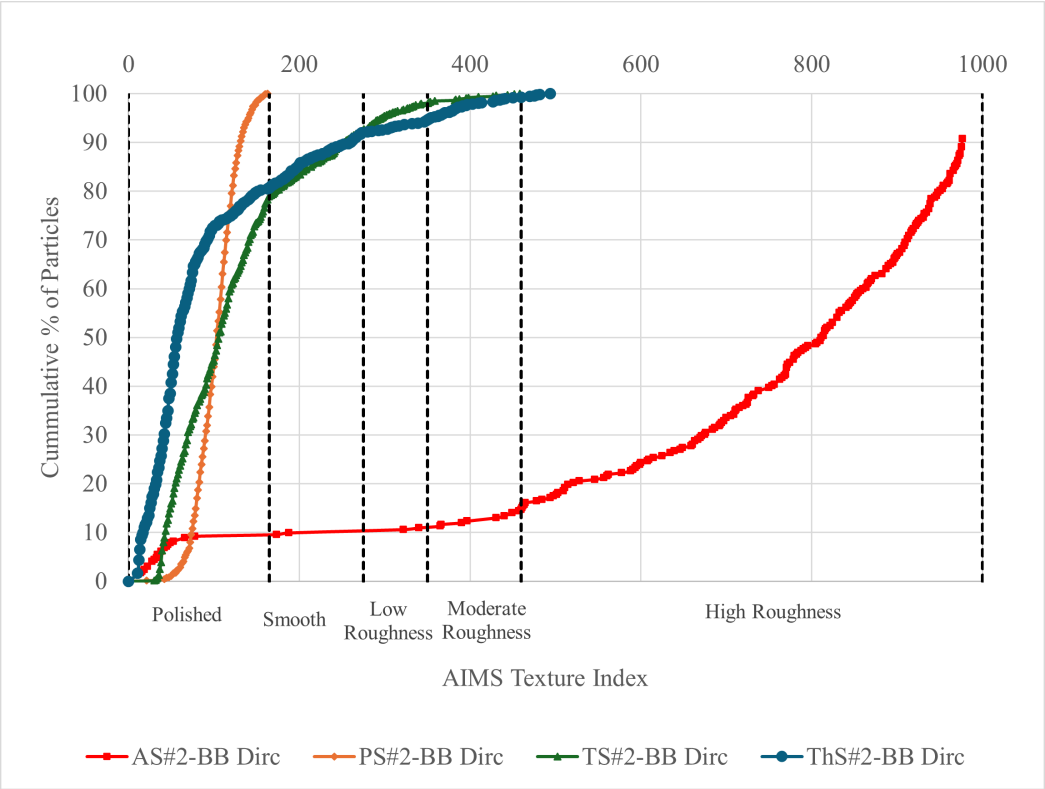

Figure 4.11: Texture index distribution across pavement markings (15.80× magnification).

Table 4.5: Percentage of Particles in Each Texture Group with Coefficient of Variation (CV%)

Marking	**Low ($\leq$ 260)**		**Medium (260–550)**		**High (550–1000)**	
	Avg (%)	CV%	Avg (%)	CV%	Avg (%)	CV%
AS#2	11.29	27.57	6.23	54.50	82.48	3.35
PS#2	65.53	0.46	4.77	10.99	0.00	N/A
TS#2	67.93	0.33	1.91	4.55	0.00	N/A
ThS#2	67.85	0.81	1.12	65.41	0.00	N/A

Note: Averages and coefficients of variation (CV%) are based on four scanning directions (AA, BB, CC, and DD).

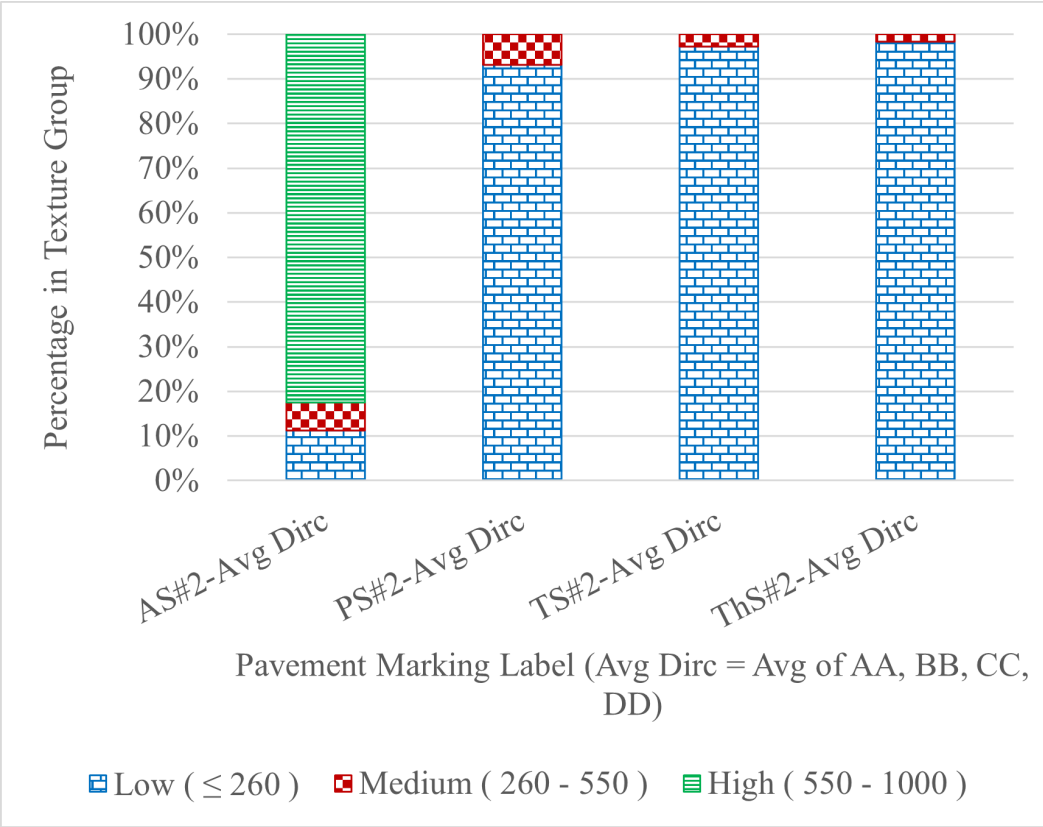

Figure 4.12: Texture group distribution by pavement marking (average of AA, BB, CC, DD directions).

4.11 Statistical Analysis

4.11.1 ANOVA, MANOVA, and Paired T-Test for Texture Comparisons

Statistical comparisons were performed to evaluate differences in surface texture between the four pavement marking materials using AIMS data in the BB scanning direction. As summarized in Table 4.6, Analysis of Variance (ANOVA), Multivariate Analysis of Variance (MANOVA), and paired t-tests were conducted to assess the significance of differences among Asphalt (A), Tape (T), Preformed Thermoplastic (P), and Thermoplastic (Th).

Table 4.6: Statistical Analysis Summary of Pavement Marking Texture — BB Direction

Test Type	Comparison	F-Value / T-Value	P-Value	No. Observations
ANOVA	A vs. T	661.7	3.38×10^{-65}	201
	A vs. P	574.1	2.63×10^{-39}	86
	A vs. Th	488.4	1.80×10^{-55}	201
	T vs. P	10510	5.04×10^{-90}	86
	T vs. Th	18500	2.75×10^{-198}	201
	P vs. Th	8802	8.23×10^{-87}	86
MANOVA	(P, T, Th) vs. A	1694.41	0.0000	86
Paired T-Test	A vs. T	39.19	8.46×10^{-96}	201
	A vs. P	15.95	2.72×10^{-27}	86
	A vs. Th	41.69	1.37×10^{-100}	201
	T vs. P	-41.96	1.36×10^{-58}	86
	T vs. Th	-1.37	0.174	201
	P vs. Th	-94.12	9.97×10^{-88}	86

Note: Texture values were obtained using AIMS in the BB scanning direction at 15.80× magnification. A = Asphalt, T = Tape, P = Preformed Thermoplastic, Th = Thermoplastic. ANOVA and paired t-tests were based on 201 or 86 paired data points, while MANOVA was applied to a multivariate matrix of 86 rows × 4 variables. The confidence level used was $\alpha = 0.05$ (95%).

ANOVA results confirm statistically significant differences among all surface types ($p < 0.05$), with the strongest difference observed between Tape and Thermoplastic ($F = 18500$). MANOVA results ($F = 1694.41$, $p < 0.05$) show that Asphalt significantly influences the multivariate texture profile across the other materials. Paired t-tests also reveal statistically significant differences in most comparisons, except for Tape vs. Thermoplastic ($p = 0.174$), indicating these two materials may share similar texture characteristics.

4.11.2 Correlation Between Texture Indices for Different Markings

As shown in Fig. 4.13, the texture index of asphalt (A) exhibits an exponential relationship with other marking types—T, Th, and P—in the BB scanning direction. Each exponential model

follows the format $Y = a \cdot \exp(b \cdot A)$, where Y is the corresponding dependent variable. A total of 201 observations were collected for A, T, and Th, and 86 for P, summing to 689 data points. Table 4.7 presents model parameters and fit statistics, confirming that all relationships are statistically significant ($p < 0.05$). Th demonstrated the strongest correlation with A ($R^2 = 0.942$) and the lowest RMSE (6.51), while P had the weakest fit ($R^2 = 0.884$). The slope confidence intervals confirmed positive exponential trends across all materials. None of the slope or intercept intervals included baseline values such as $b = 0$ or $a = 1$, suggesting consistent material-specific behavior rather than neutral trends. Fig. 4.14 further supports these results by illustrating strong correlations among all markings, with coefficients above 0.92.

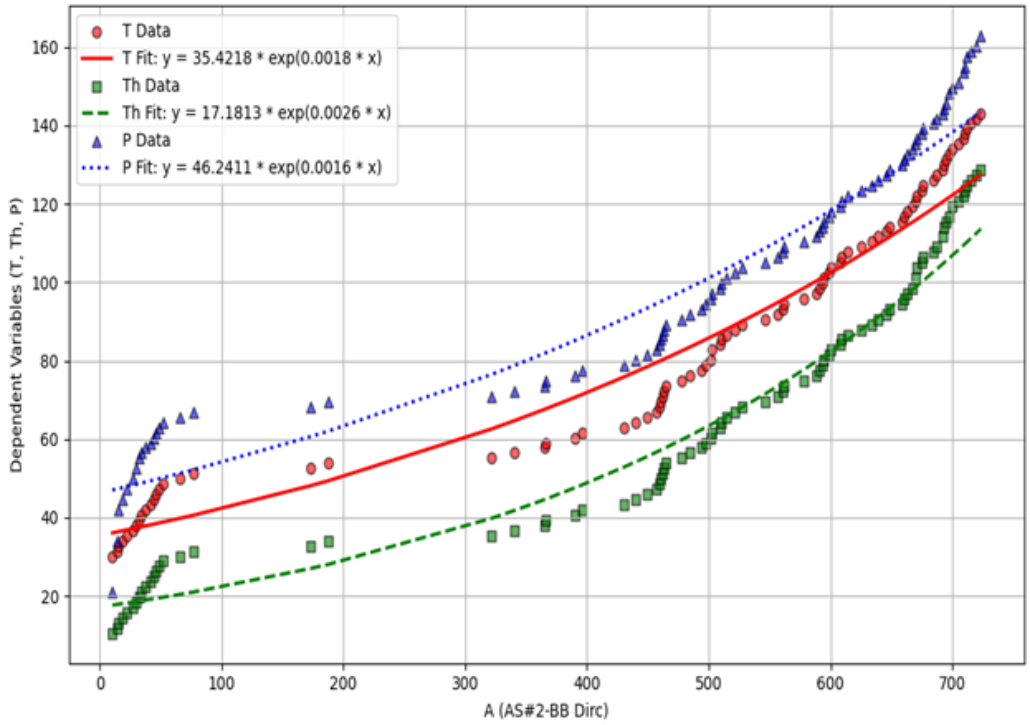

Figure 4.13: Exponential fits of texture index A vs. T, Th, and P in BB scanning direction

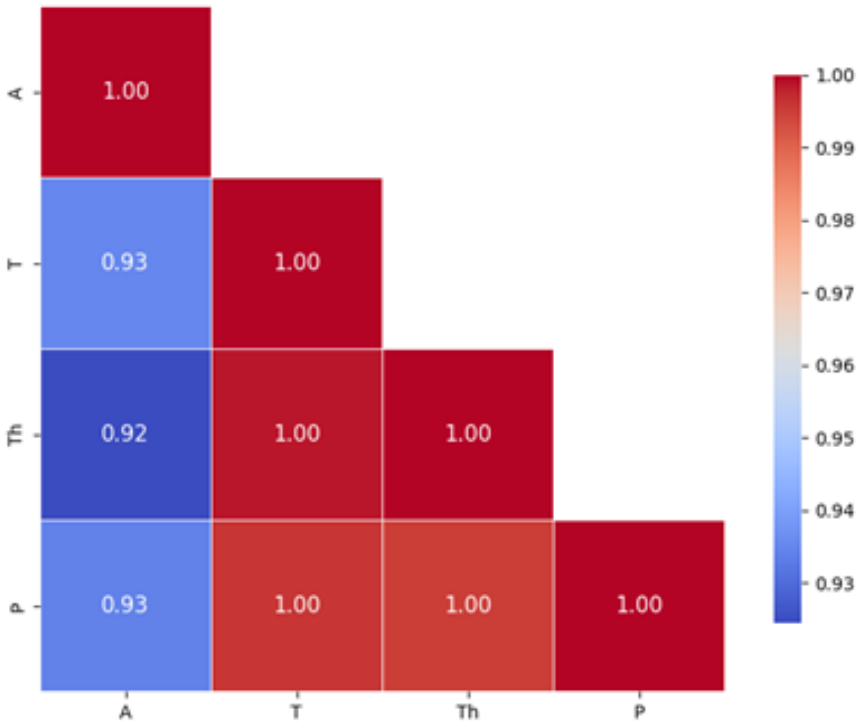

Figure 4.14: Correlation matrix of texture indices for A, T, Th, and P

Table 4.7: Exponential Model Results for Texture Analysis in BB Scanning Direction

Marking Type	**Exponential Equation**	**Slope CI**	**Intercept CI**	**p-Value**	**R^2**	**RMSE**
T	$T = 35.4218 \cdot e^{0.0018A}$	(0.0017, 0.0019)	(33.77, 37.16)	1.16×10^{-54}	0.945	7.489
Th	$Th = 17.1813 \cdot e^{0.0026A}$	(0.0025, 0.0028)	(15.98, 18.47)	1.06×10^{-53}	0.942	6.510
P	$P = 46.2411 \cdot e^{0.0016A}$	(0.0014, 0.0017)	(43.40, 49.27)	4.45×10^{-41}	0.884	8.646

4.12 Summary and Conclusion

This chapter evaluated the surface texture of four pavement markings (AS#2, TS#2, ThS#2, and PS#2) with AIMS. Texture was measured with RMS, MPD, and MTD in four radial scan

directions. AS#2 recorded the highest values in all measurements, followed by TS#2 and ThS#2. PS#2 recorded the lowest values. Directional variation occurred in AS#2 and ThS#2, while TS#2 and PS#2 recorded more uniform textures. RMS trends agreed with BPN results confirming texture and friction correlation.

Statistical analysis confirmed the presence of meaningful differences in markings. Exponential regression models delivered distinct correlations between AS texture and other materials and ThS#2 was the best fit. Quartile and distribution analysis indicated rougher surfaces for AS#2 and smoother profiles for PS#2. AIMS delivered reliable and coherent texture data aligned with friction measurements and distinctly differentiated marking types.

Chapter 5: Multimodel Assessment of Pavement Marking Friction Using Supervised Machine Learning Techniques

5.1 Overview

Pavement markings are a fundamental component of road infrastructure and serve to manage, warn, and direct drivers and pedestrians [118–120]. Particularly, visibility and friction performance of markings at crosswalks are of the highest significance to pedestrian and vehicular safety [33, 97, 98, 121]. Reduced skid or slip resistance of such surfaces causes vehicle accidents or pedestrian falls, especially during wet or icy conditions [6, 12, 122–124]. While retroreflectivity has typically been the focus for maintenance programs, the friction characteristics of retroreflective markings have received comparatively less focus, though they directly affect traction and safety performance [12, 125, 126].

Standard tests such as the British Pendulum Tester (BPT), are used extensively to measure surface friction by measuring the BPN, which is representative of a surface's microtexture-related slip/skid resistance [46, 99, 127, 128]. However, such measurements are generally limited to field measurements, which are costly, time-consuming, and susceptible to fluctuations in environmental conditions [28, 129–131]. In addition, current asset management practices cannot often predict friction deterioration or potentially hazardous markings before failure [132–135].

Latest developments in artificial intelligence (AI) and machine learning (ML) offer promising solutions to these challenges. ML techniques have been successfully applied to numerous

problems in pavement engineering, including performance prediction, surface texture evaluation, and the prediction of material behavior [136–142]. Tree-based models such as RF and XG are best suited for application in pavement engineering due to their competence in handling datasets with both numerical and categorical variables, and in identifying complex, nonlinear relationships among them [143–146]. Other methods, such as SVR, GPR, and MLP, have also been shown robust in predicting nonlinear trends in high-dimensional data [147–149]. For instance, Marcelino et al. [139] applied RF models in predicting pavement roughness from traffic and environmental data. Similarly, Koné et al. [150] employed SVR and Decision Trees to predict skid resistance from roadway surface data. They showed that nonlinear models like SVMs are capable of capturing complex relationships in frictional behavior accurately. Nevertheless, these works primarily take into account the usual pavement surfaces and do not consider the unique material and surface interaction of pavement markings.

In spite of all these developments, fewer studies have been conducted predicting pavement marking friction using ML. The majority of research work has typically examined pavement surface friction or asphalt texture analysis and not particularly modeled friction in pavement markings with different environmental and test conditions [147, 151]. This provides the potential to formulate predictive models incorporating marking type, test conditions, device, temperature, and surface characteristics into repeatable tools for use in pavement marking safety programs.

In an effort to address this gap, this research creates and assesses supervised machine learning models for the prediction of BPN (TSR), tire slip rubber friction, or pavement marking skid resistance. The study relies on a database comprising 1,092 observations obtained from laboratory and field experiments on four pavement marking materials: P, Th, Pt, and T. Laboratory tests had three types of surfaces: D, W, and I, while field tests had just D and W, since tests on an I

surface were not performed due to safety concerns. RF, XG, SVR, GPR, and MLP are the five models compared. Model training was performed using 5-fold cross-validation with hyperparameter tuning via `GridSearchCV`. Each of the models is tested using widely used regression error metrics (R^2, RMSE, MAE, and MAPE) and diagnostics of residual distribution such as Kolmogorov–Smirnov tests and empirical cumulative distribution functions (eCDFs).

5.2 Literature Review

5.2.1 Skid and Slip Resistance of Pavement Markings

Friction performance between the tire and pavement is an important aspect of road safety, particularly at pedestrian crossings where both pedestrian slip resistance and vehicle skid resistance are necessary [6, 12, 33]. Although pavement markings are usually evaluated based on their visibility, they can have quite different frictional properties compared to the surrounding pavement, especially under W or I conditions [6, 33, 126]. Th and Pt, for example, may reduce both available macrotexture and microtexture by smoothing the surface, which lowers tires' or shoes' ability to gain adequate grip [6, 33].

The BPT is one of the most commonly used instruments for measuring pavement friction. It gives the BPN, which indicates surface microtexture. This number helps evaluate tire skid resistance (TSR) or pedestrian slip resistance (PSR) based on the rubber slider used [46, 99, 127, 128]. While BPT testing usually takes place in controlled laboratory settings, field testing is also performed to check real-world performance [6, 33]. For instance, Bao et al. [99] found initial wet BPN values between 30.5 and 62.0 across different marking materials in Indiana. The results revealed that Th-markings had some of the lowest friction levels, while waterborne paints and

specific polyurea systems showed higher initial BPN values. This indicates significant differences based on the type of material and surface treatment.

Frictional behavior is influenced by many interconnected variables. These include surface characteristics, vehicle dynamics, tire properties, and environmental conditions. Table 5.1 summarizes the main factors affecting available skid resistance, according to the classification proposed by Kumar and Gupta [28]. The key factors are microtexture, braking action, tread design, contamination, and temperature.

Table 5.1: Influential Factors on Tire–Pavement Skid Resistance [28]

Surface Characteristics	**Vehicle Parameters**	**Tire Properties**	**Environmental Conditions**
Microtexture Macrotexture Surface type Aggregate properties Surface ageing	Vehicle speed Slip ratio Braking action Tire inclination	Tire footprint Tread pattern Inflation pressure Loading condition	Temperature Rain intensity Contamination

Various roadways and conditions demand varying levels of friction for safe vehicle and pedestrian movements. For example, as shown in Table 5.2, Australian specifications have a minimum of 0.55 skid resistance for traffic signal-controlled intersections and 0.50 for tight-radius curves. On the contrary, the United Kingdom suggests the range of 0.35 to 0.50 based on the road design and usage [124]. These thresholds state the greater accident likelihood in certain areas and emphasize the need to keep friction levels above critical safety limits.

Despite the significance of friction, most agencies prioritize retroreflectivity in performance measurements, with friction being tested occasionally or wholly ignored. Retroreflectivity assists in enabling drivers to see markings during nighttime but does not play a role in the mechanical

interaction of the vehicle tire and pavement marking surfaces [125]. As noted by Goulias and Aljarrah [33] and Nassiri et al. [6], the distinction becomes critical when W or I conditions reduce available grip. As noted by Maia [46], friction reduces over time due to wear, polishing, and exposure to the environment, and may not be apparent without direct measurement or prediction tools.

Table 5.2: Skid Resistance Standards in the UK and Australia [124]

Country	**Skid Resistance Threshold**	**Applicable Road Types**
United Kingdom	0.35 – 0.50	0.35 on motorways and dual carriageways (non-event); 0.40 on single carriageways (non-event) and dual carriageways (all purposes); 0.45 on bend–dual carriageways; 0.50 on bend–single carriageways
Australia	0.25 – 0.55	0.25 on divided carriageways (non-event); 0.35 at junctions, undivided carriageway (non-event), and free areas of divided road; 0.40 on undivided/free areas and curves $<$ 250 m; 0.50 on tight curves; 0.55 at signalized intersections

While both visibility and friction are critical for the performance of pavement markings, they are regulated by various factors. Visibility is determined by retroreflectivity, type of headlamps, marking geometry, environmental conditions, and driver factors. Conversely, friction is determined by surface texture, contamination, water film thickness, and tire–pavement contact. Table 5.3 presents the key factors influencing the visibility of pavement markings from the findings of Debaillon et al. [125].

Table 5.3: Key Factors Influencing Visibility of Pavement Markings [125]

Category	Factor	Impact on Visibility
Retroreflectivity & Contrast	Pavement Retroreflectivity Surface Material	Higher values improve detection distance Affects contrast under headlights
Lighting Conditions	Vehicle Headlamps Overhead Lighting	Newer systems enhance nighttime visibility Improves visibility at night
Marking Geometry	Edge Line Presence Marking Width	Aids lane guidance Wider lines are easier to detect
Driver Factors	Driver Age Preview Time	Older drivers need more retroreflectivity Longer preview improves detection
Environmental Conditions	Pavement Color Pavement Wear Weather Headlight Glare	Affects daytime contrast Decreases marking clarity Reduces visibility in rain, fog, or snow Lowers retroreflective visibility
Vehicle & Road Factors	Windshield Transmission Driver Workload	Impacts clarity through glass High workload limits marking awareness

5.2.2 Machine Learning Approaches for Pavement Friction Prediction

5.2.2.1 Random Forest (RF)

RF is a powerful ensemble machine learning algorithm known for its accuracy and resistance to overfitting on both classification and regression tasks. RF builds numerous trees such that every tree is trained using a random bootstrap sample of the data so that observations may be replicated across trees [143, 152]. For each decision node, the algorithm uses a random feature subset to determine the best split, and this introduces variation and minimizes prediction errors [143]. The output is obtained by averaging the predictions in the case of regression or majority vote for classification [143]. RF also eases the computation of feature importances, which is of interest for friction modeling in pavements because environmental, material, and test conditions might have complex interactions [153]. Of the most critical parameters, the number of

trees, the maximum tree depth, `mtry` (number of features to consider when splitting), and `min` (minimum number of samples for a node split) are the core characteristics [154]. The interested reader is referred to in-depth reviews by Jiang et al. [152] and Biau and Scornet [155] for a more complete theoretical understanding of Random Forests.

5.2.2.2 eXtreme Gradient Boosting (XGBoost)

Extreme Gradient Boosting, or XGBoost, is an efficient and scalable version of the gradient boosting decision tree algorithm. It creates a group of regression trees that reduces the residual error left by the previous trees. This process combines many weak learners to form a strong prediction model [154]. In each step, the model attempts to maximize a defined objective function that considers prediction error and regularization in order to improve generalization. As compared to Artificial Neural Networks (ANNs) and Support Vector Machines (SVMs), XGBoost is less sensitive to outliers, has simpler hyperparameter tuning accessibility, and is capable of performing both regression and classification tasks. In addition, its built-in mechanism for dealing with missing values makes it most suitable for infrastructure applications where missing data is common.

For each iteration, the model integrates the output of t regression trees as follows [143,154]:

$$\hat{y}_i = \sum_{k=1}^{t} f_k(x_i) \tag{5.1}$$

where $f_k(x_i)$ represents the prediction from the k-th regression tree and $\hat{y}_i$ is the cumulative prediction for instance i. The update at step t is computed by adding the newly fitted tree $f_t(x_i)$ to the previous prediction:

$$\hat{y}_i^{(t)} = \hat{y}_i^{(t-1)} + f_t(x_i) \tag{5.2}$$

In this expression, $\hat{y}_i^{(t)}$ is the updated prediction at iteration t, calculated as the previous prediction $\hat{y}_i^{(t-1)}$ plus the output of the newly added regression tree $f_t(x_i)$, which models the residual error based on the input x_i.

To optimize the model, XGBoost minimizes a regularized objective function that balances prediction accuracy and model complexity:

$$obj^{(t)} = l(y_i, \hat{y}_i^{(t)}) + \gamma T + \frac{1}{2}\lambda \sum_{j=1}^{T} w_j^2 \tag{5.3}$$

In this formulation, the first term $l(y_i, \hat{y}_i^{(t)})$ represents the loss function, which measures the discrepancy between predicted and actual values. The remaining terms constitute the regularization component: T denotes the number of leaf nodes in the tree, and $\sum_{j=1}^{T} w_j^2$ corresponds to the squared L_2 modulus of the leaf weights.

5.2.2.3 Support Vector Regression (SVR)

SVR comes from SVMs and is used for both regression and classification tasks. It is based on the Structural Risk Minimization Principle (SRMP). This principle provides strong generalization performance and overcomes some of the limitations of traditional neural networks [156].

Karballaeezadeh et al. [157] used SVR to predict pavement remaining service life, with an emphasis on enhancing parameter tuning. The SVR objective function is:

$$\min\left(\frac{1}{2}\mathbf{w}^T\mathbf{w} + C\sum_{i=1}^{N}(\delta_i^+ + \delta_i^-)\right) \tag{5.4}$$

where $\mathbf{w}$ is the weight vector, C controls the trade-off between model complexity and training error, and δ^+, δ^- are slack variables incorporated to handle constraints that would otherwise render the optimization problem unsolvable [158].

To enhance SVR performance, a particle filter was used for state estimation under uncertainty:

$$x_k = f_k(x_{k-1}, u_k, \omega_k), \quad y_k = h_k(x_k, u_k, v_k) \tag{5.5}$$

where x_k and y_k are system state and output, u_k is input, and ω_k, v_k are noise terms [159]. This combination improved SVR's predictive accuracy for pavement modeling.

5.2.2.4 Gaussian Process Regression (GPR)

GPR models the relationship between input variables and a target output using an arbitrary function $f(x)$, combined with additive Gaussian noise $\epsilon \sim \mathcal{N}(0, \sigma_n^2)$. This forms the regression model [160]:

$$y = f(x) + \epsilon \tag{5.6}$$

The function $f(x)$ is assumed to follow a Gaussian process defined by a mean function $m(x)$ and a covariance function (or kernel function) $k(x, x')$ [160]:

$$f(x) \sim \mathcal{GP}(m(x), k(x, x') + \sigma_n^2 I) \tag{5.7}$$

The predictive mean and variance for new inputs X_* are given by [160]:

$$\bar{y}_* = m(X_*) + k(X_*, X)\left[k(X, X) + \sigma_n^2 I\right]^{-1}(y - m(X)) \tag{5.8}$$

$$\text{var}(y_*) = k(X_*, X_*) - k(X_*, X)\left[k(X, X) + \sigma_n^2 I\right]^{-1} k(X, X_*) \tag{5.9}$$

where I is the identity matrix. The term $\bar{y}_*$ represents the predictive mean, and var(y_*) corresponds to the predictive variance.

The only known research on using GPR to predict road surface conditions is by Heyns et al. [161]. They introduced a speed calibration method that includes road condition data in the calibration process. In their approach, GPR helped create a dynamic calibration function that changes in real time as the vehicle moves over different surfaces. Their results showed that this method could provide a practical and cost-effective solution for real-time road monitoring [148].

5.2.2.5 Multilayer Perceptron Neural Networks (MLP)

MLP is a feedforward artificial neural network that has been used extensively on supervised learning tasks and does not have any assumption regarding the distribution and patterns of the input data [147]. An MLP consists of an input layer, hidden layers, and an output layer, and each neuron is fully linked to the next layer through weighted connections [162].

Each hidden neuron computes a weighted sum of its inputs and applies an activation func-

tion to introduce nonlinearity. In our study, MLP was used with three hidden layers comprising 64, 32, and 16 neurons, respectively. The Rectified Linear Unit (ReLU) activation function was also used since it is effective and can alleviate vanishing gradient problems in deep networks [163].

The final output Y' is computed as [147]:

$$Y' = \sum_{i=1}^{n} (\omega_i \cdot \text{ReLU}(\alpha_i)) + \vartheta \tag{5.10}$$

where ω_i are the connection weights, α_i is the net input to the neuron i, and ϑ is the output bias term. The model was trained with the Adam optimizer, which is a flexible version of stochastic gradient descent. It changes learning rates during training to speed up convergence and make it more reliable [164]. Backpropagation helped reduce prediction errors and update the model weights [147].

5.3 Methodology

5.3.1 Data Collection, Preparation, and Description

As discussed earlier, this paper used a 1,092 BPN measurements taken from lab and field testing of four pavement marking types: P, Th, Pt, and T. Markings testing was conducted in the lab under D, W, and I surface conditions, but only in D and W conditions in the field because of concerns related to safety. All the tests were carried out on asphalt and concrete samples in the laboratory and on corresponding field locations utilizing two BPT units, Unit A and Unit B.

As listed in Table 5.4, the dataset has 18 various laboratory samples (6 each of materials P,

T, and Th), all measured 6 times under 3 surface conditions mentioned earlier, with 2 different BPT units and totaling 648 BPN laboratory measurements. Field testing was conducted at 18 different locations on four materials (P, Th, Pt, and T), with 6 replicates each, 2 surface conditions, 1 BPT unit, and 2 or 3 test dates per material. To exemplify, P-markings were tested at 13 locations, each of which yielded 6 replicates × 2 conditions × 2 dates, for a total of 312 field measurements. With the other materials, the field data set yielded 444 measurements. The entire study has 1,092 BPN(TSR) readings, all taken under a standard protocol in accordance with ASTM E303-22 [128].

Table 5.4: Detailed Breakdown of Lab Samples and Field Test Locations Used

Type	**Material**	**Loc./ Samples**	**Rep.**	**Cond.**	**Dev.**	**Dates**	**Total (N)**	**Details**
L	P	6	6	3	2	1	216	4 Concrete, 2 Asphalt
	T	6	6	3	2	1	216	4 Concrete, 2 Asphalt
	Th	6	6	3	2	1	216	4 Concrete, 2 Asphalt
F	P	13	6	2	1	2	312	Tested twice per location
	Th	2	6	2	1	2	48	Two test dates per location
	Pt	2	6	2	1	2	48	Two test dates per location
	T	1	6	2	1	3	36	Three tests at one location

For modeling, the target variable was BPN(TSR), the British Pendulum Number measured with the Tire Slip Rubber slider. Seven predictor variables were used. Categorical variables were label-encoded so that each category was replaced with an integer (e.g., Unit A = 0, Unit B = 1). The numerical variable of ambient temperature remained in its original form. For feature scale-sensitive models—Support Vector Regression (SVR), Gaussian Process Regression (GPR), and Neural Network—all the variables were standardized using z-score normalization. Missing observations were removed, and a complete dataset was available for training. A detailed overview

of the input variables, i.e., types and encoded categories, is provided in Table 5.5.

Table 5.5: Description of Input Variables

Variable	**Description**	**Type**	**Categories / Range**
V1	Test unit	C	Unit A (0), Unit B (1)
V2	Surface condition	C	D (0), W (1), I (2)
V3	Marking material	C	P (0), T (1), Th (2), Pt (3)
V4	Pavement surface type	C	A (0), C2 (1)
V5	Test environment	C	L (0), F (1)
V6	Ambient temperature (°C)	N	6.0 to 30.0
V7	Surface debris presence	C	Cl (0), Di (1)

Figure 5.1 shows the methodological strategy followed during this study. Figure 5.2 shows the neural network architecture, and Figure 5.3 shows a simplified tree structure from the Random Forest model depicting how input features are being used to divide data and predict BPN(TSR).

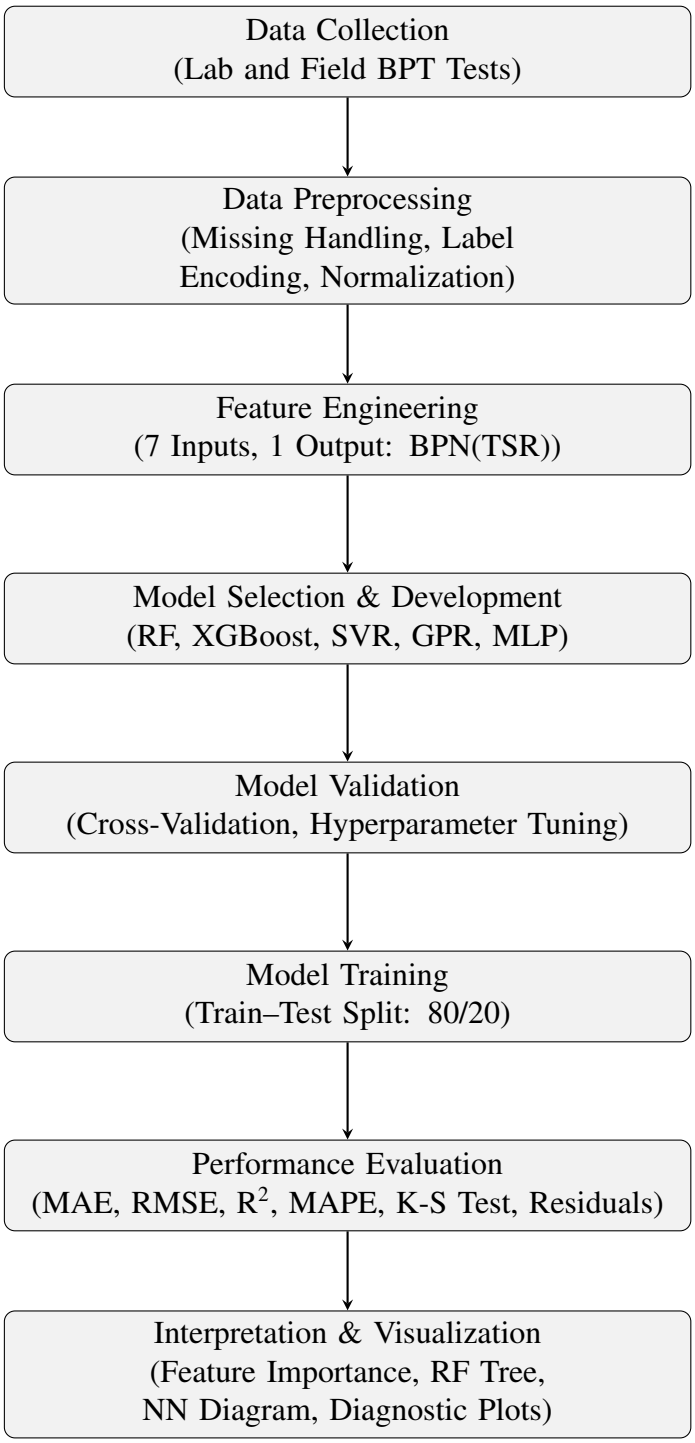

Figure 5.1: ML Methodology

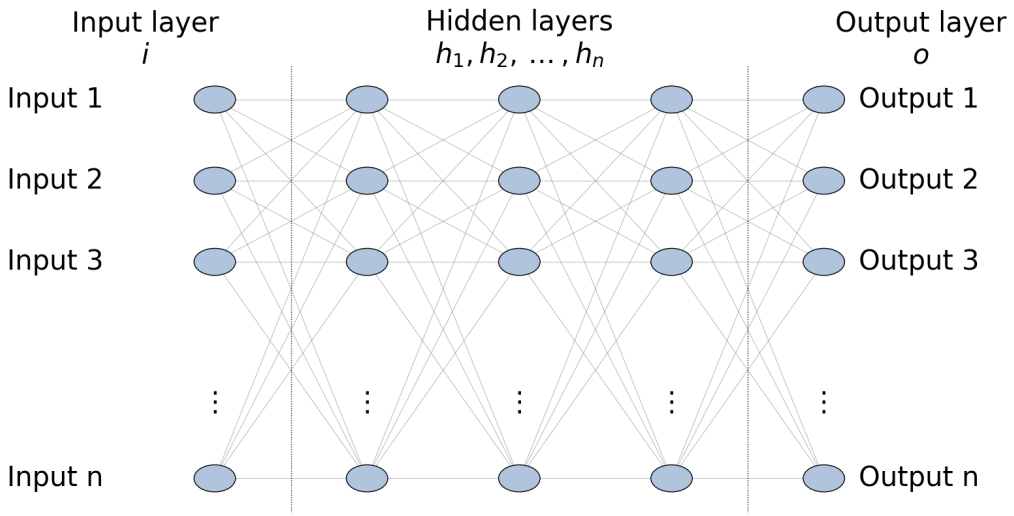

Figure 5.2: MLP Neural Network Architecture

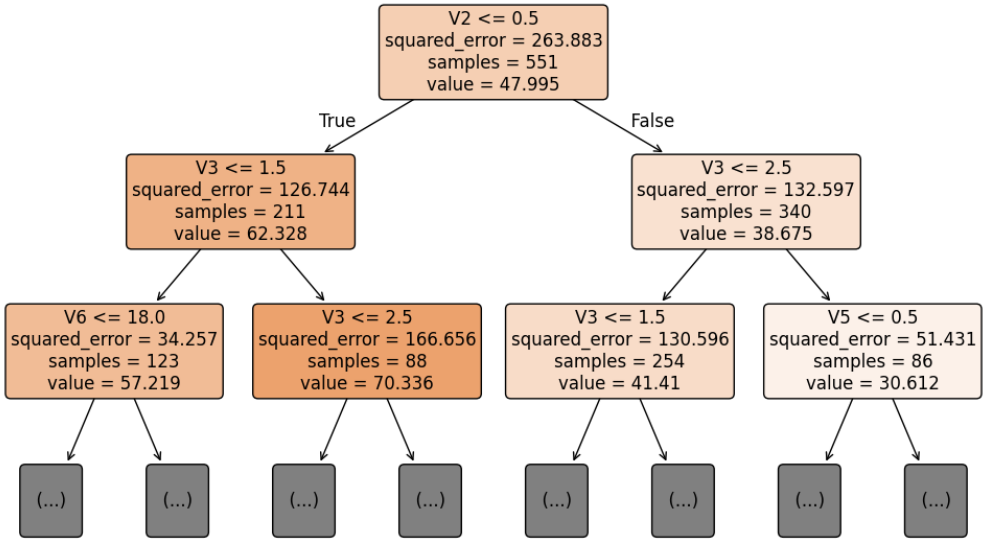

Figure 5.3: Simplified Random Forest Tree

5.3.2 Machine Learning Model Development and Setup

Five ML algorithms were selected for modeling: RF, XG, SVR (SVR), Gaussian Process GPR, and MLP, as described earlier. All models were implemented with optimal parameters selected by GridSearchCV-based hyperparameter optimization. Specifically, 100 estimators were

utilized in RF and XG, the SVR model was supplied with a radial basis function (RBF) kernel, and the MLP was a three-layer network (64, 32, 16 neurons) with ReLU activation and Adam optimizer (see Table 5.6).

The input dataset was split into 80% for training and 20% for testing. Label encoding was done on categorical features as described previously. Z-score normalization was applied to scaling-sensitive models, i.e., SVR, GPR, and MLP. Both RF and XG models operated on the original dataset without scaling.

To ensure the model's generalizability and to prevent overfitting, all models were validated using 5-fold cross-validation. GridSearchCV was also used to tune hyperparameters for each algorithm to find the best configurations. Table 5.6 summarizes the main settings, scaling needs, and ability of each model to capture nonlinear relationships.

Table 5.6: Comparison of Machine Learning Model Configurations and Requirements

Model	**Type**	**Scaling**	**Nonlinear**	**Key Parameters**	**Solver**
RF	Ensemble Tree-Based	No	Yes	n_estimators=100, min_samples_split=2, random_state=42	Greedy Tree Split
XGBoost	Gradient Boosting	No	Yes	learning_rate=0.05, max_depth=6, n_estimators=100, random_state=42, verbosity=0	Tree Boosting
SVR	Support Vector Regression	Yes	Yes	C=100, epsilon=0.2, kernel=rbf	QP Dual Solver
GPR	Gaussian Process Regression	Yes	Yes	alpha=0.01, kernel=RBF(1.0), normalize_y=True	L-BFGS
Neural Network	Multilayer Perceptron (MLP)	Yes	Yes	activation=relu, alpha=0.0001, hidden_layers=(64,32,16), solver=adam, max_iter=1000, random_state=42	Adam

Note: All models were tuned using GridSearchCV with 5-fold cross-validation.

5.3.3 Model Performance Evaluation

In an effort to examine the predictive ability of the five ML models, certain statistical measures of errors were computed using the test dataset. They include the coefficient of determination (R^2), root mean squared error (RMSE) and mean absolute error (MAE) that quantify the accuracy and robustness of each model. The metrics are presented as [143, 145, 149]:

$$R^2 = 1 - \frac{\sum_{i=1}^{n}(y_i - \hat{y}_i)^2}{\sum_{i=1}^{n}(y_i - \bar{y})^2} \tag{5.11}$$

$$RMSE = \sqrt{\frac{1}{n}\sum_{i=1}^{n}(y_i - \hat{y}_i)^2} \tag{5.12}$$

$$MAE = \frac{1}{n}\sum_{i=1}^{n}|y_i - \hat{y}_i| \tag{5.13}$$

where y_i is the actual value, $\hat{y}_i$ is the predicted value, $\bar{y}$ is the mean of the actual values, and n is the number of observations in the test set.

Additional metrics were used to complement the evaluation, including mean absolute percentage error (MAPE), maximum absolute residual difference (i.e., maximum error between predicted and actual values), the Kolmogorov–Smirnov (K-S) statistic, and the corresponding p-value. Adjusted R^2 was determined as well to account for the number of predictors used in each model. These are outlined in Table 5.7 and provide a description of performance across the models tested. Diagnostic plots such as residual histograms, Q-Q plots, and empirical cumulative distribution functions (eCDFs) were also used to make further assessments of model fit and

residual behavior.

Table 5.7: Performance Comparison of ML Models

Model	MAE	MSE	RMSE	R^2	Adj R^2	MAPE (%)	Max Dev	K–S Stat	K–S p-val
RF	2.67	14.3	3.78	0.950	0.949	6.41	12.3	0.109	0.0103
XG	2.69	14.2	3.77	0.951	0.949	6.47	12.1	0.101	0.0218
SVR	2.94	19.3	4.39	0.933	0.931	6.86	14.8	0.146	0.0001
GPR	2.67	14.3	3.78	0.950	0.949	6.41	12.2	0.105	0.0154
MLP	2.78	14.9	3.86	0.948	0.947	6.66	12.4	0.101	0.0222

Note: MAE = Mean Absolute Error; MSE = Mean Squared Error; RMSE = Root Mean Squared Error; R^2 = Coefficient of Determination; Adj R^2 = Adjusted R^2; MAPE = Mean Absolute Percentage Error; Max Dev = Maximum Deviation; K–S = Kolmogorov–Smirnov.

5.4 Results and Discussion

5.4.1 Model Prediction Results

Predictive performance of all five tuned ML models was evaluated on the holdout test set. As seen in Figure 5.4, predictions by RF and XG models followed the actual BPN(TSR) observations closely across the entire range. Predictions from most of these two models were clustered around the 45-degree equality line, showing minimal systematic bias. Predictions from the GPR and Neural Network models followed a similar trend but showed slightly wider dispersion. Conversely, the SVR model showed strong underprediction in the mid and low BPN ranges, which reflects a limited ability to generalize in these regions.

Quantitative performance measures are presented in Table 5.7 and depicted in Figure 5.5. The XG model attained the highest coefficient of determination ($R^2 = 0.951$) and the lowest RMSE of 3.77, followed by Random Forest and GPR (both with $R^2 = 0.950$), all with RMSE values under 3.8 and MAE around 2.67. These three models also possessed relatively low max-

imum deviation scores (around 12.2) and lower MAPE values (ranging from 6.41% to 6.47%) compared to MLP and SVR, which recorded 6.66% and 6.86% respectively, confirming their strong goodness of fit. The MLP performed comparably, although with a slightly higher RMSE (3.86). SVR, on the other hand, produced the lowest R^2 (0.933), the highest RMSE (4.39), and the highest residual error (14.8). RF and XG both performed visually and quantitatively as the most robust models to predict BPN(TSR).

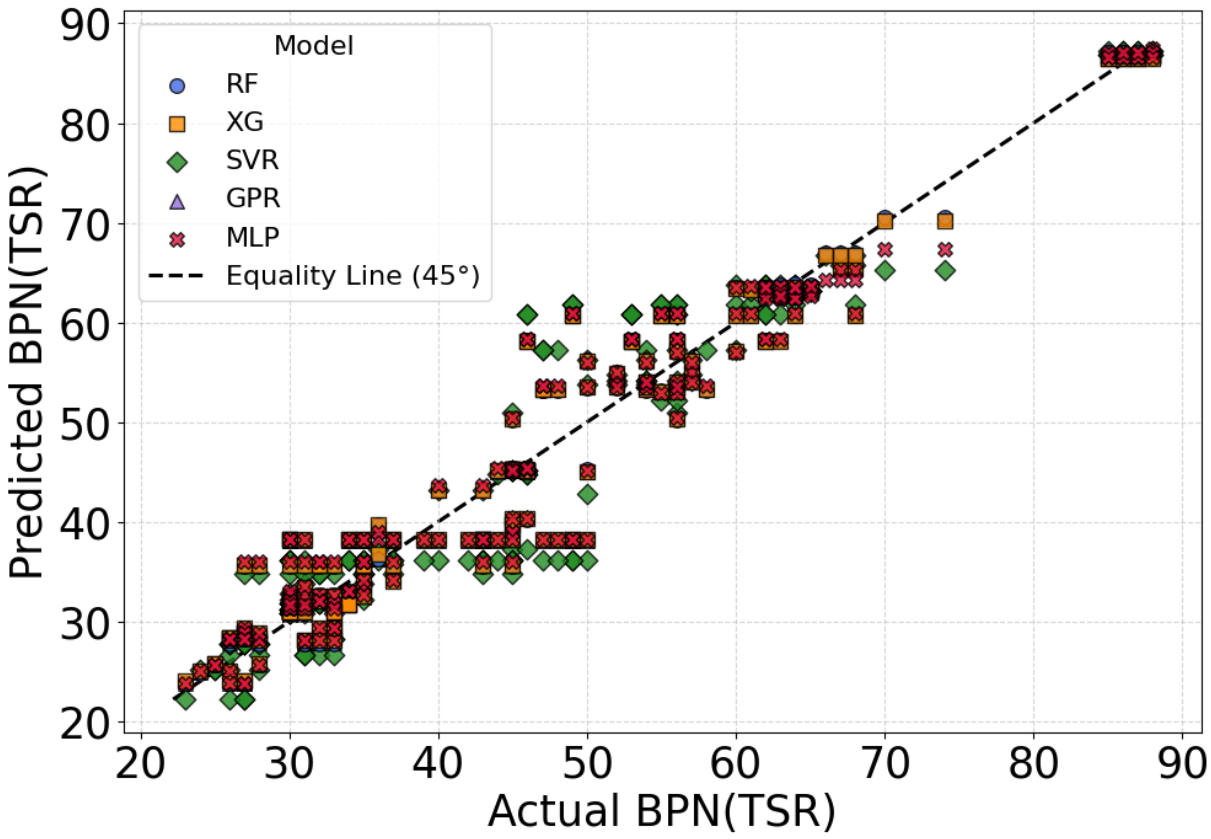

Figure 5.4: Predicted vs. Actual BPN(TSR) for all models

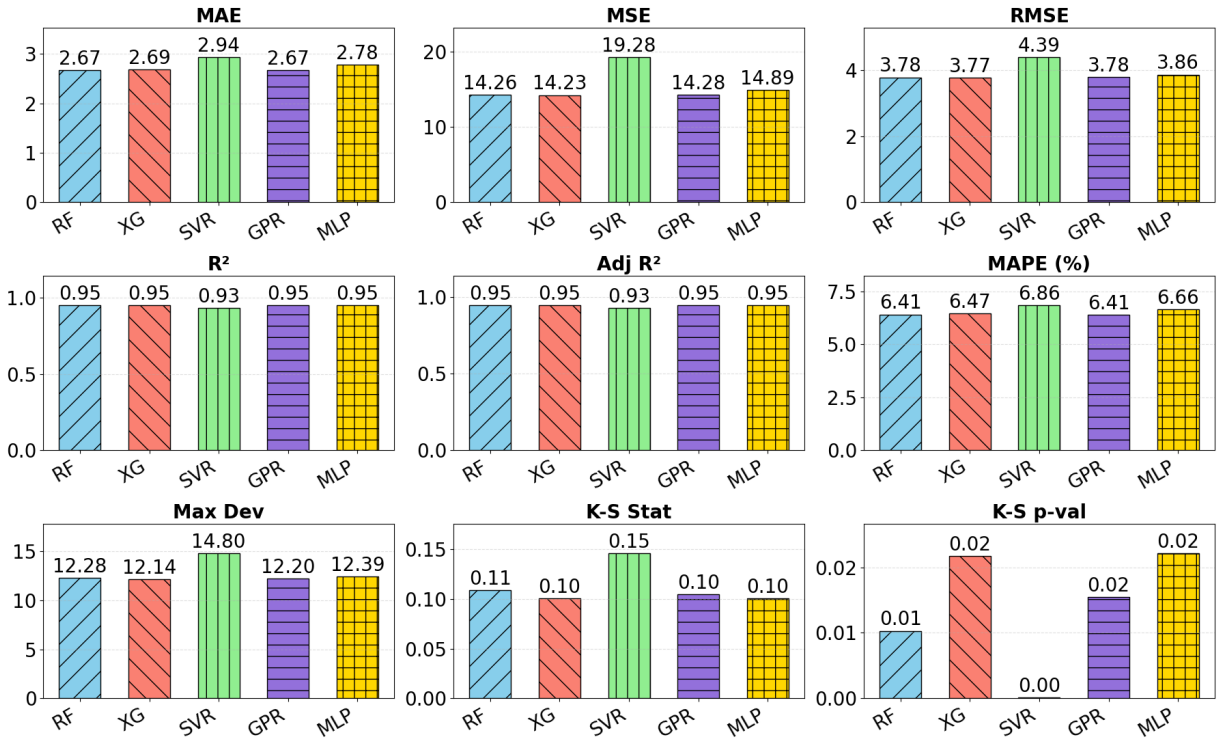

Figure 5.5: Performance Evaluation of Tuned Machine Learning Models

5.4.2 Residual Diagnostics and Distributional Assessment

Residual diagnostics were used to check consistency, bias, and distributional behavior of all models. RF, XG, GPR, and MLP's residuals vs. predicted BPN(TSR) plots in Figure 5.6 show a centered, homoscedastic spread. Residuals cluster tightly around zero with no visible trends or patterns, showing low bias over the entire range of predictions and consistent variance. On the contrary, SVR possesses a bit wider spread with certain asymmetry, particularly at intermediate predicted values, indicating higher residual variability than the other models.

Distributional characteristics are also investigated in Figures 5.7 to 5.9. In Figure 5.7, histograms and kernel density estimates (KDE) both possess bell-shaped curves for all models

with near-normal behavior. SVR possesses deviations in the tails, as can be seen from its KDE. Figure 5.8 confirms this, empirical cumulative distribution functions (eCDFs) for XG, RF, MLP, and GPR follow the normal reference curve closely, while SVR deviates noticeably from the reference. Figure 5.9 further demonstrates this difference more vividly: whereas all models except SVR align well along the 45-degree reference line, SVR displays curvature towards the center of the Q–Q plot that indicates central tendency bias. Collectively, these diagnostics confirm that the ensemble models, GPR, and the MLP provide us with almost normal residuals, whereas SVR provides weaker compliance, especially towards the middle range.

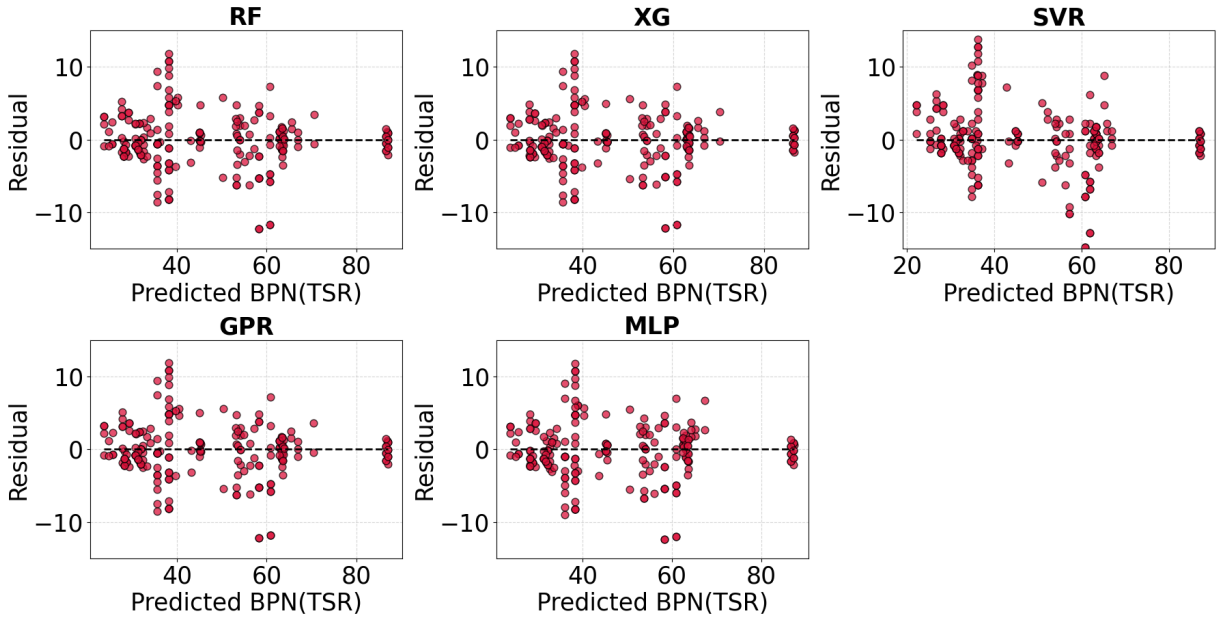

Figure 5.6: Residuals vs. Predicted BPN(TSR)

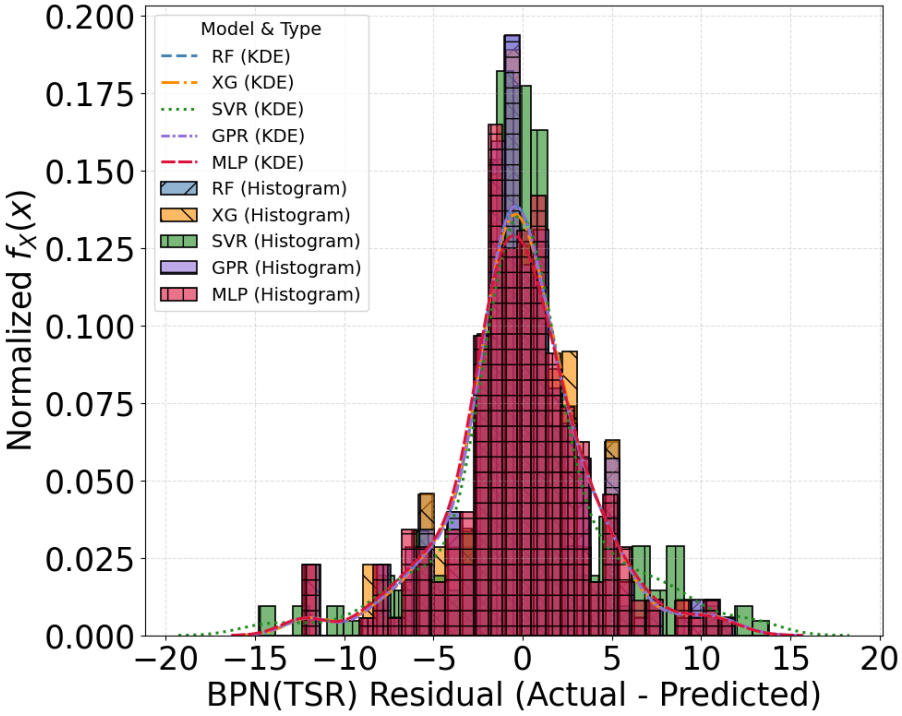

Figure 5.7: PDFs of Residuals with KDE

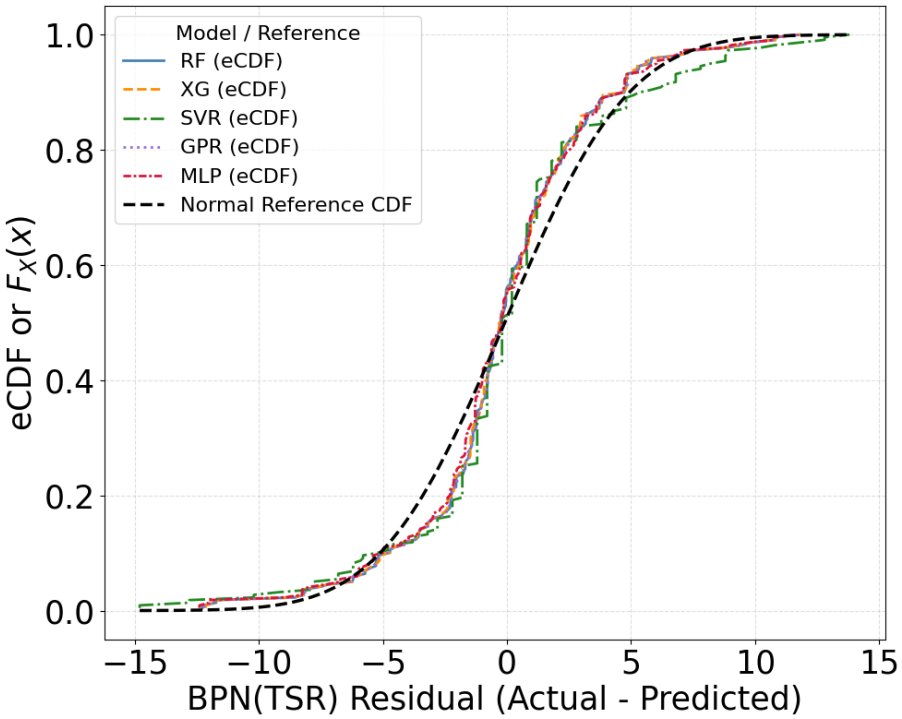

Figure 5.8: eCDFs of Residuals with Normal Reference

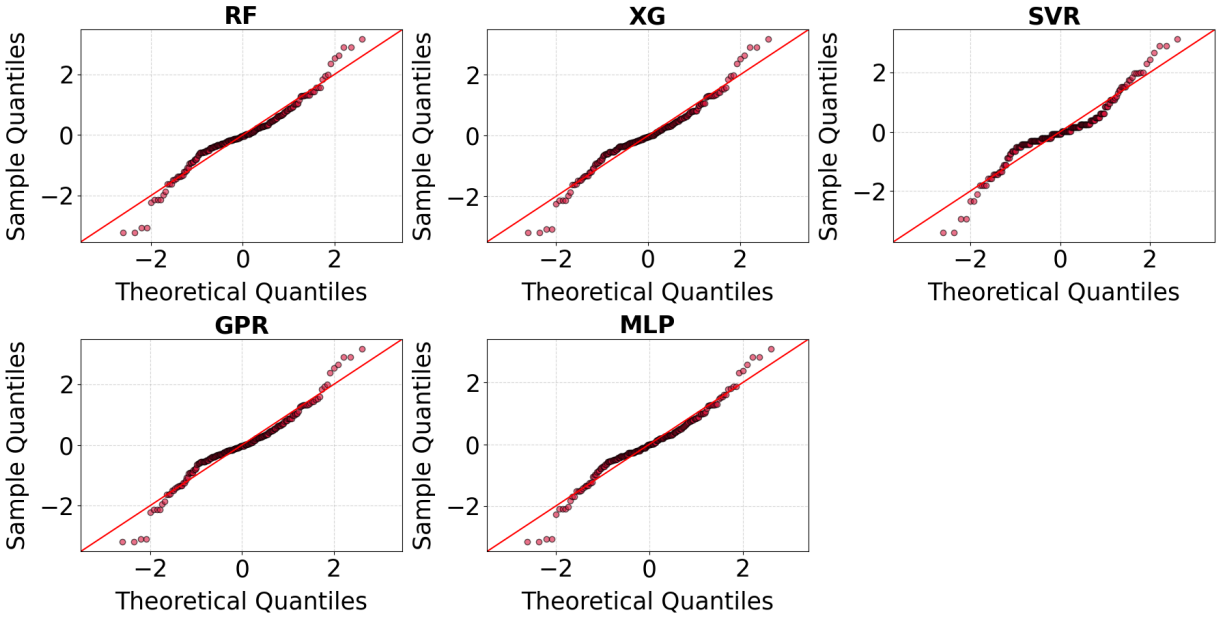

Figure 5.9: Q–Q Plots of Residuals

5.4.3 Distribution Fit and Feature Relevance Analysis

To further examine the residual behavior of the ML models, some probability density functions (PDFs) were employed to fit each model's residuals. As it is clear from Figure 5.10, five distributions have been placed over the empirical histograms—normal, lognormal, exponential, Rayleigh, and uniform. In all models, the normal and lognormal curves best visually fit the residual distributions. RF, XGBoost, GPR, and MLP all showed narrow, symmetric residual shapes that closely resembled the normal PDF. SVR also showed the same pattern, where normal and lognormal fits were very close to the residual spread.

Figure 5.11 presents cumulative distribution function (CDF) plots of empirical residual distributions versus theoretical fits. The empirical CDFs from all models closely followed both the normal and lognormal references. SVR had the largest deviation from these references, par-

ticularly in the tail and middle regions, but overall shape was fairly well aligned. These visual patterns were quantified in Table 5.8, where the maximum residual deviation, best-fitting distributions based on empirical CDFs and Kolmogorov–Smirnov (K-S) tests, and their test statistic and p-value are tabulated. For RF, XG, GPR, and MLP, the best overall fit was provided by the normal distribution. However, SVR displayed the best fit to the lognormal distribution in both the empirical and the K-S-based tests.

Table 5.8: Goodness-of-Fit Summary for Residual Distributions of Tuned ML Models

Model	**Max Dev**	**Best Fit (eCDF)**	**Max Dist to eCDF**	**Best Fit (K–S)**	**K–S Stat**	**K–S p-val**
RF	12.28	normal	0.104	normal	0.108	0.011
XG	12.14	normal	0.096	normal	0.100	0.023
SVR	14.80	lognormal	0.146	lognormal	0.146	0.000
GPR	12.20	normal	0.100	normal	0.104	0.016
MLP	12.40	normal	0.096	normal	0.100	0.023

Note: Max Dev = maximum absolute residual; eCDF = empirical cumulative distribution function; K–S = Kolmogorov–Smirnov; K–S Stat = test statistic; K–S p-val = p-value.

In addition, feature importance was assessed for the tree-based models. Figure 5.12 shows that RF and XG gave variables V2, V3, and V5 the highest ranking as the most influential predictors of BPN(TSR), contributing most of the model's predictiveness. The remaining variables were relatively insignificant, with a large proportion of feature relevance being confined to the three predictors mentioned earlier.

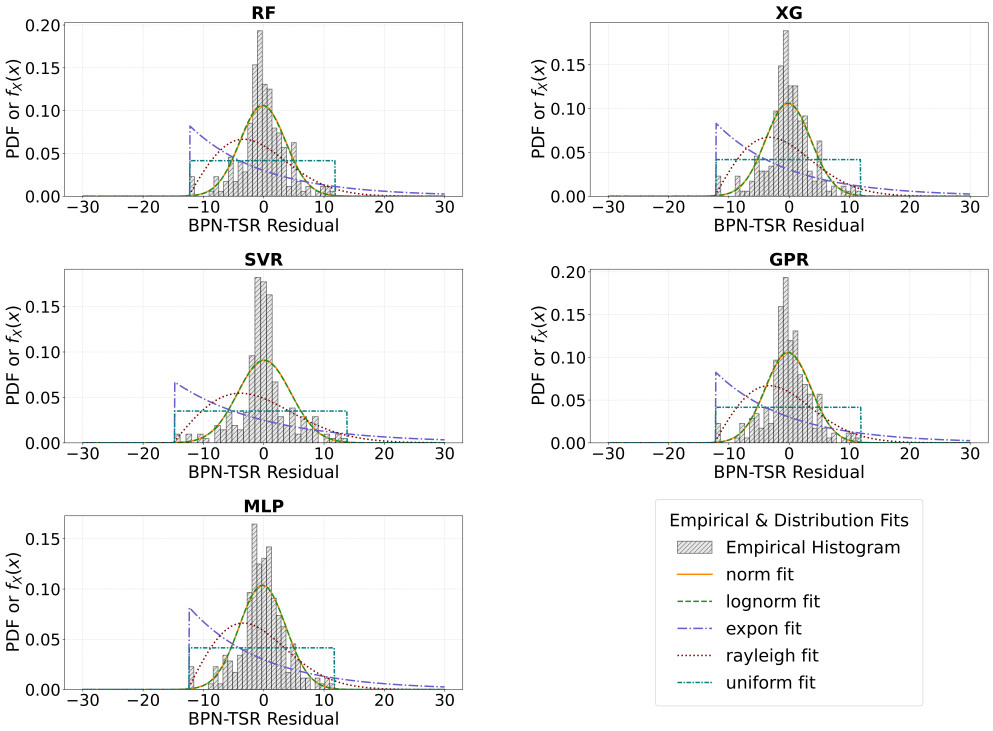

Figure 5.10: Fitted PDFs overlaid on empirical histograms of BPN(TSR) residuals for different ML models.

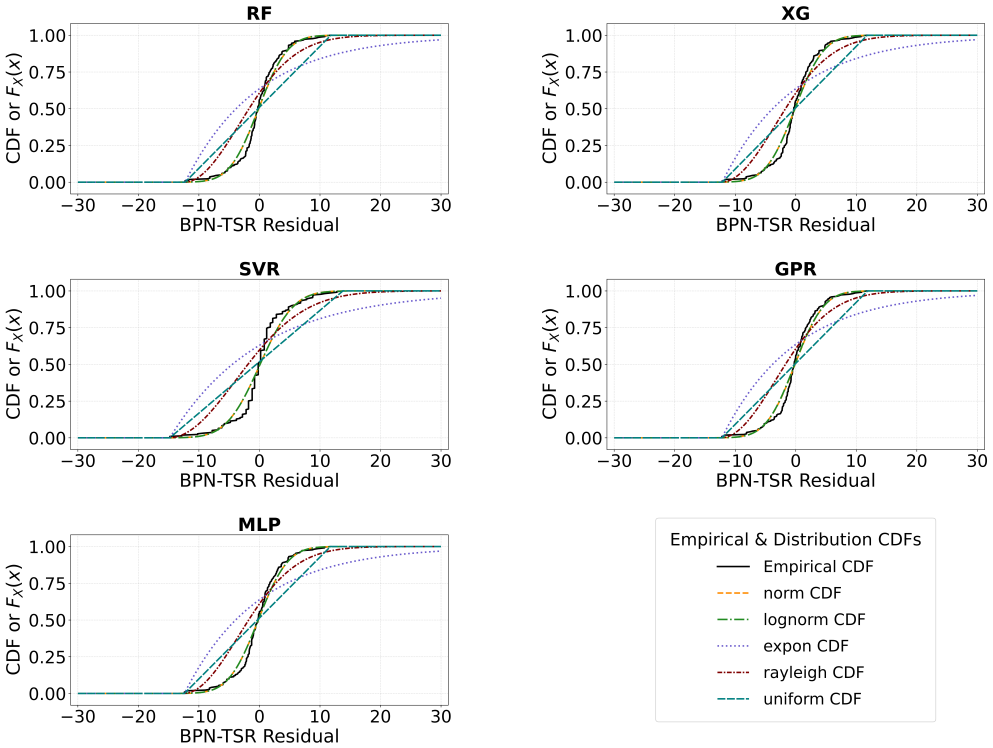

Figure 5.11: CDF Comparison of BPN(TSR) Residuals Across Tuned Machine Learning Models.

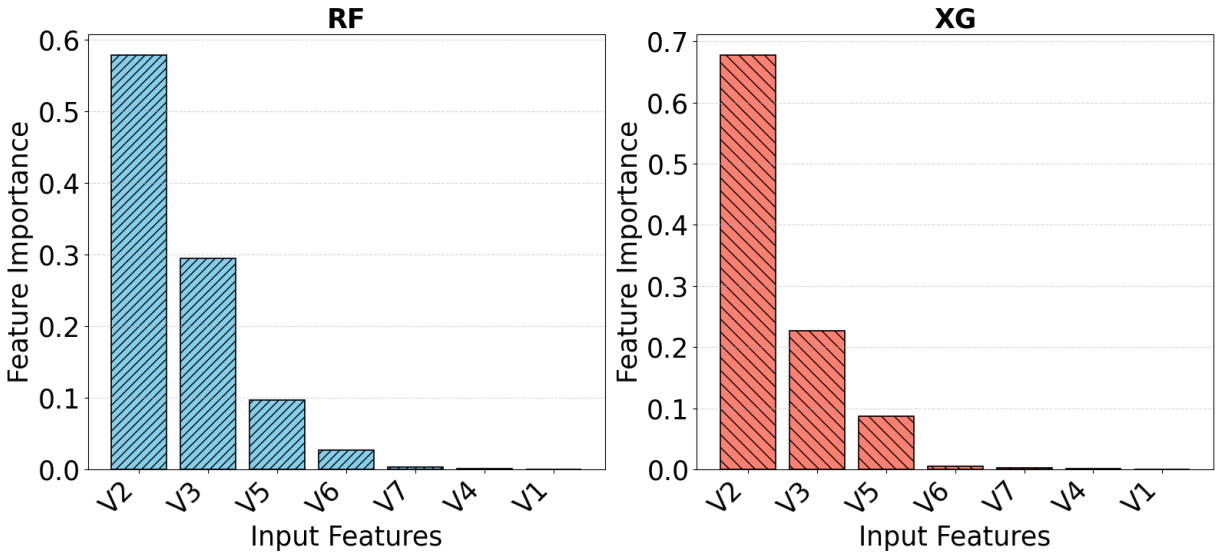

Figure 5.12: Feature Importance for Tree-Based ML Models.

5.5 Conclusions

Five machine learning algorithms were applied in this study to predict the BPN(TSR) using a large dataset that was collected from laboratory and field using the BPT on different pavement marking materials. Models examined were RF, XG, SVR, GPR, and a MLP, all trained and cross validated with hyperparameter tuning. Performance was assessed via common metrics such as R^2, RMSE, MAE, and MAPE, in addition to diagnostic residual analysis and goodness-of-fit testing.

Among the models, RF and XG produced the best, most accurate, and most consistent predictions with R^2 values approximating 0.95, the lowest RMSE, and stable, centered residuals. MLP and GPR also performed well, but with a slight degree of variability. SVR came with larger residual errors and manifested greater variability in residual patterns, particularly for mid-range predictions. However, distributional tests confirmed that residuals for all five models were

best represented by a normal distribution, with the only exception being SVR, for which fit was considerably better for the lognormal distribution based on Kolmogorov–Smirnov statistics and eCDF comparison.

Feature importance analysis revealed that three input features (V2, V3, and V5) accounted for the majority of predictability power in tree-based models, further improving model interpretability as well as usability. To sum up, ensemble learning models, RG, and XG, provide a reliable and accurate solution to modeling pavement markings friction behavior in terms of BPN(TSR). These findings illustrate the potential for using machine learning to enable friction performance assessment and safety evaluation on transportation infrastructure.

Chapter 6: Distress Based Performance Prediction of Pavements and the Master Curve Approach

6.1 Overview

Over the past decades, a number of models have been developed to predict pavement performance and distress evolution in flexible pavements. Early approaches were primarily deterministic and empirical and were developed from historical trends and regression-based equations such as the AASHTO 1993 design guide, which were widely used and based on standardized inputs, but had limited transferability [165]. Mechanistic-empirical (M-E) models were developed to combine structural mechanics and empirical damage calibration to enable more specific predictions with the use of traffic, climate, and material response [166]. The AASHTOWare Pavement ME Design is a common mechanistic-empirical tool; however, studies show that its nationally calibrated performance models often do not accurately predict regional pavement response, requiring local calibration for reliable prediction of distress and roughness [167]. Probabilistic models, such as Markov chain models, have been used in pavement management systems. For example, in Arizona were used to forecast pavement condition states under various scenarios [168]. Monte Carlo simulation was also used to evaluate flexible pavement performance considering the influence of traffic loads, material properties, and temperature variation on predicted pavement reliability [169].

Mechanistic-empirical models tend to be developed for design purposes and have been ap-

plied with limited use in pavement management systems. Their use often includes numerous input parameters such as pavement thickness, traffic loading, material strength, and climatic conditions, often thus limiting their transferability across regions with different characteristics [170]. Despite local calibration, significant differences were reported between predicted and observed pavement performance, especially in terms of roughness and longitudinal cracking, due to variability in input conditions and potential lack-of-fit in the prediction models [166]. This is especially concerning when models are applied between different climates and pavement structures (e.g., between Alabama's humid climate and Arizona's arid climate). Pavement studies have indicated that the application of national predictive models without regional calibration consistently yields large prediction errors, particularly for some distresses like rutting and fatigue cracking. For example, the AASHTO 1993 model was determined to significantly over-predict pavement performance in Alabama, especially for granular base sections [165]. Therefore, while these models provide useful frameworks, practical application involves robust datasets, local calibration, and sometimes probabilistic extensions to properly predict pavement distress.

Despite advances in pavement engineering, challenges persist with respect to the proper modelling of distresses. For example, [171] discussed the challenges in modelling the complex interaction between traffic and climate, and pavement materials interactions responsible for rutting and thermal cracking in flexible and composite pavements. Transverse cracks are essentially related to the thermal stress of HMAs due to their oxidation and aging. These effects are particularly important in cold climates with freeze-thaw cycles. Research using Bayesian Belief Networks (BBN) was directed towards probabilistic modelling of intricate inter-relationships among sparse data of various variables, which were of complex relationships as outlined by [172].

The LTPP program is one of the important components of the Strategic Highway Research

Program (SHRP), and it has provided an extensive set of data for better understanding materials and pavements with data derived from over 2,500 test sections across North America. With the release of the latest version, Standard Data Release 37, August 2023, the database aids in further research pertinent to distress and performance predictions, among others. Since becoming a Federal Highway Administration (FHWA)-led program in 1991, the focus of the LTPP has been on General Pavement Studies (GPS) and Specific Pavement Studies (SPS) with the objective of improving pavement durability and performance [173–175].

The objective of this study was to develop a systematic approach to using such data to predict future conditions. The suggested modelling considered the development of prediction functions (i.e., "master curves") for pavements of similar design and material. Among the various distresses, fatigue cracking and permanent deformation (i.e., rutting) of asphalt sections were explored. The shift functions for the "master curve" modelling need to be related to mixture and pavement properties, such as asphalt layer thickness, air voids, dynamic modulus of asphalt mixture, and other parameters. Since pavement distresses are material and section-specific, the objective of this modelling approach was to develop prediction functions for a group of asphalt mixtures with comparable properties and under similar climatic conditions.

This represents an advantage to more accurate predictions since distress models developed from broad and diverse datasets, covering various pavement structures, traffic levels, and climate conditions, often show reduced accuracy due to variability in input parameters, uncertainty in the influence of different factors, and sensitivity to local calibration requirements [165,166,170–172].

6.2 Master Curve Concept & Uses

The Master Curve concept has been successfully explored in a couple of alternative highway materials and pertinent prediction modelling phenomena [176–178]. Examples include:

- Use of the Time-Temperature Superposition Principle (TTSP) to describe the viscoelastic behaviour of polymers and bituminous materials [176, 177]. The TTSP facilitates the construction of a unified curve to represent material behavior over a wide range of temperatures and frequencies at a reference condition [179]. Contributions by Ferry [180] established the theoretical basis for TTSP, highlighting its applicability to polymer viscoelasticity and setting the stage for its adoption in asphalt pavement analysis.

- The Master Curve approach was also incorporated in pavement design analysis using the theory of viscoelastic continuum damage (VECD) to better describe the fatigue life of asphalt mixtures [181, 182]. The modelling approach, incorporating the rate dependency of both the growth of damage and reduction in material integrity, has enabled the intrinsic understanding of the response of asphalt to changing traffic loads and temperature variations. Emphasis is made that controlling mixture variables because of asphalt intrinsic heterogeneity results in a more accurate estimate for the prediction of pavement performance and durability [183].

- Zhao et al. [39] investigated the understanding of polyurethane mixtures in pavement design by constructing a dynamic modulus master curve. The viscoelastic properties of these mixtures are investigated by applying different models and methods that considerably deviate from traditional asphalt behavior. This research underlined the importance of model

selection for the accurate performance prediction and provides important insights into pavement engineering.

- Recent pavement engineering innovations have considered the expansion of the concept of the Master Curve to the geothermal effects of asphalt pavements and advanced asphalt mixture modelling. Works like Al-Atroush et al. [184] and Chen et al. [102] furthered the understanding of dynamic responses of pavement materials under various conditions and improved the Master Curve's usability in pavement performance predictions. These developments will ensure increased durability of the pavement, its resistance against extremes of climatic changes, and at the same time open avenues for future research in sustainable and accurate methodologies of performance prediction in pavement engineering. The development of master curves and pertinent shift factors was also examined by additional studies, either addressing their potential use in pavement performance modelling [170,185] or assessing the fatigue response through viscoelastic damage analysis for mixtures with recycled materials such as tire rubber [186].

- Saremi and Goulias [178] investigated the use of master curves in maturity modelling and strength predictions of concrete using both destructive and non-destructive testing. In that study, the hydration temperature–time history of concrete was explored in defining "master curves" for concrete maturity. The study findings indicated that the approach of "master curves" for the maturity of concrete can be defined and provides accurate predictions. The shift factors for each mixture's maturity function in relation to the master curve were successfully related to concrete properties.

6.3 Study Objectives

Thus, the objective of this study was to explore the applicability of the master curve principle in predicting pavement distress based on the LTPP data. In this regard, pavement distress data from Arizona and Alabama were utilized to simulate the arid southwestern and humid southeastern U.S. climates, respectively. Sections were screened to ensure structural and material property compatibility, including asphalt concrete (AC) layer thicknesses commonly ranging from 83.82 to 187.96 mm. One exception, Arizona Section 162, had an AC thickness of 228.6 mm but was retained due to the complete material and performance data. Base thickness ranges were from approximately 96.52 to 416.56 mm in both states. Only sections with repeated distress measurements over time and full property records, such as plasticity index (PI), percent passing No. 200 sieve (N200P%), and specific gravity (SG), were considered. This selection follows the guidelines given by Li et al. [187], which emphasize data completeness, structural uniformity, and material consistency to facilitate appropriate distress modeling.

The following study steps were thus undertaken:

1. **Analysis of LTPP Data:** Analyze the LTPP database with particular interest in data corresponding to the State of Alabama and the State of Arizona. This involves extraction, cleaning, and interpretation regarding pavement distress data types as earlier identified. This analysis was also focused on determining the variables influencing pavement performance, which may involve environmental factors, traffic loads, and material properties.

2. **Development of Master Curves for Pavement Distress Prediction:** Develop and refine the master curves on different types of pavement distresses, using the LTPP data. Identifi-

cation of a representative pavement section for centering the master curve development for each distress type.

3. **Explore Alternative Distress Predictive Forms:** Examine alternative model forms, such as linear, logarithmic, and exponential, that can better represent distress evolution under traffic and environmental conditions of the selected sections.

4. **Develop the Shift Functions in MC Modeling:** Define the shift functions for producing the "master curve" representing distress prediction for all pavement sections (i.e., shifting individual sections' distress functions into the master curve). The term "shift functions" is employed in the context of mathematical relationships between section-specific data and pavement characteristics to calculate shift factors. These shift factors would subsequently be used to shift individual distress curves to align with a unified master curve [178]. Furthermore, it was the aim of this study to relate and link material and pavement design parameters to such shift functions.

5. **Develop and Compare Distress Predictions for the Selected States:** Based on the analysis and models developed in this study, it was of interest to assess the master curves developed for each state. Alabama and Arizona were selected particularly to have diverse climatic conditions, i.e., humid subtropical and hot arid climates, respectively, and to ensure diversity in HMA mixture types, pavement configurations, and local construction practices. The latter differences, along with different levels of traffic loadings (ESALs), were expected to lead to distinctive pavement degradation patterns and to enable testing of master curve modeling under diverse conditions of environment and operation. Whereas Maryland was first considered, it was excluded because it had few test sections with limited

distress and material data not meeting the study's selection criteria.

6.4 Methodology

Figure 6.1 outlines the methodological framework for the study, dealing with data acquisition and refinement, statistical analysis, and modeling techniques in analyzing pavement distresses.

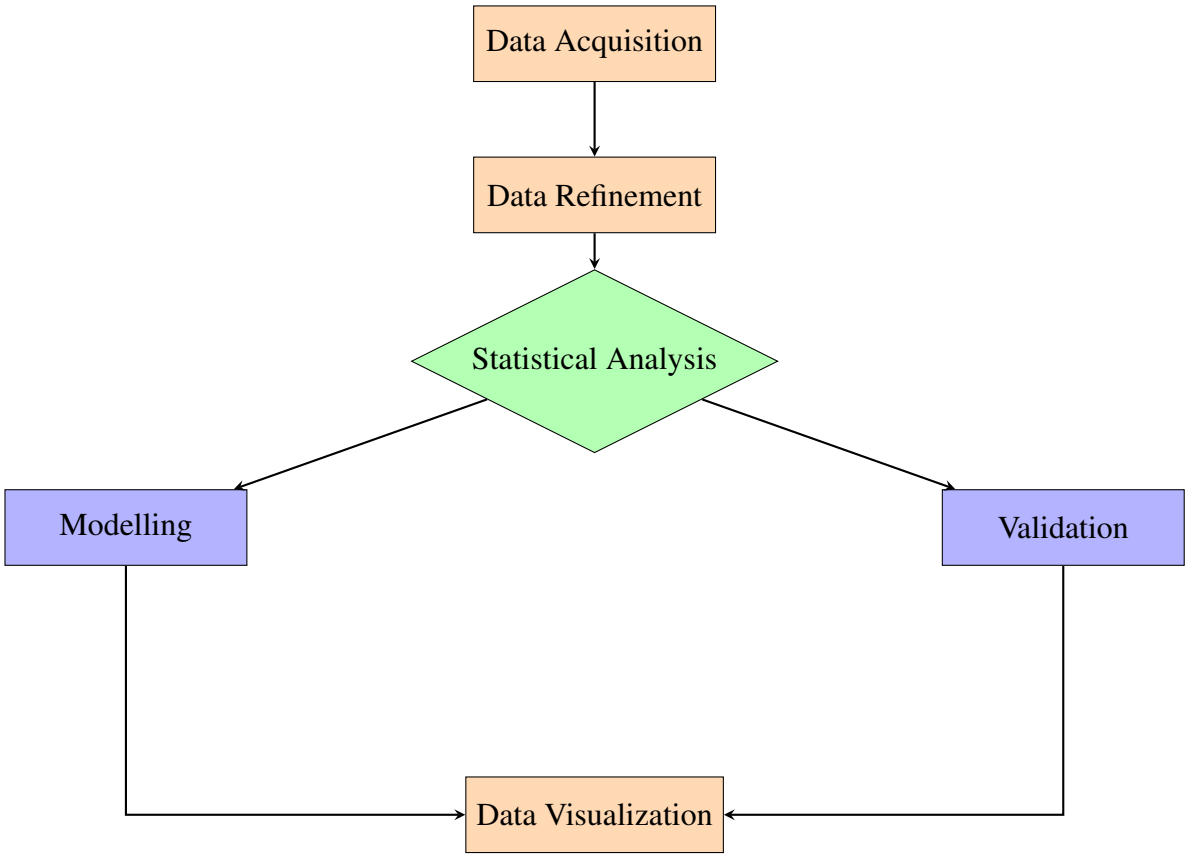

Figure 6.1: Overview of the Research Methodological Framework

The first step, Figure 6.1, was pertinent to data acquisition from the LTPP database for pavement sections from Alabama and Arizona. This dataset is a comprehensive one, covering a wide range of variables relevant to pavement performance assessment, including, but not limited to, fatigue cracking, rutting, transverse cracking, and wheel path length cracking. Environmental

and traffic loading conditions were quantified by means of ESALs, which were extracted along with the selection criteria in order to encapsulate the most diverse climatic exposures and traffic conditions [188].

An organizational scheme was defined and used to categorize data by type of distress. This aids in targeting in the analysis each pavement distress type, and smooths the analysis process for better efficiency. Data cleaning involved filtering techniques from Excel, that is, identification and correction of errors and inconsistencies, missing values, duplicated entries, and incorrect entries, outliers analysis, and careful detection and review of extreme values far from the mean or median of a data set.

The refined dataset provided an appropriate basis for statistical analysis, such as identifying data patterns, correlation determination, and identifying predictive models of pavement performance. Influence of environmental conditions, traffic loads, and pavement distresses was examined using Excel's statistical capabilities along with the use of Minitab software in conducting descriptive statistics, correlation analysis, and regression modelling. The analysis provided the type of influential factors, such as asphalt layer thickness, air voids, and resilient modulus, that are associated with the development of pavement distress.

One of the major goals of the data refinement process was to ensure the integrity of the dataset through several validation checks, including benchmark comparisons and consistency cross-referencing. Benchmark comparisons involved the comparison of LTPP section data, such as asphalt concrete (AC) thickness, base thickness, and distress values (e.g., fatigue cracking, rutting) with prescribed ranges and definitions provided in key FHWA resources, including the Distress Identification Manual for the LTPP Program [189], the LTPP IMS User Guide [190], and outcomes of structural evaluations such as the SPS-1 experiment [191]. Cross-correlation

of consistency was based on comparisons of whether similar distress patterns were occurring at equivalent levels of traffic loading (e.g., ESALs), pavement structure, and climate exposure, as identified in earlier study analyses of deterioration patterns [192]. These are essential validation protocols that will assert the reliability of the data, hence laying a good foundation for subsequent HMA master curves and predictive modeling efforts.

Central to the analysis is the use of a regression model form to represent the progression relationships of pavement distresses. Linear regression was used to capture the trends of pavement distresses and relate the factors influencing them. Calibration of the predictive models and influencing parameters involved fine-tuning the model fitting process by minimizing the residual sum of squares of the prediction errors, and thus improving the accuracy and predictive capability of the models. Validation of the predictive models' performance was assessed using a subset of the LTPP sections. Statistical metrics, such as R^2 and RMSE, were used, which yielded good fits $(R^2 > 0.9,\ p < 0.05)$ and therefore validated the master curve models developed.

The sensitivity analysis forms the basis for the methodology in quantifying the effect of traffic loads (represented by cumulative ESALs used as the independent variable in the regression models presented in Table 6.1) and other relevant factors on the severity and incidence of pavement distresses. Such analysis included the use of Pearson's correlation coefficients (Tables 6.2 and 6.3) and multivariate regression (Tables 6.4, 6.5, 6.6, and 6.7) to single out those key variables influencing pavement deterioration, hence providing insights for formulating pavement preservation.

Table 6.1: Example R^2 for Best Fit Logarithmic Deterioration Models for Various Distresses with Time and/or ESALs

Section	FC and ESALs	WP and ESALs	RD and ESALs	TC and ESALs
AL-101	0.93	0.84	0.88	0.64
AL-102	NA*	NA*	0.94	0.97
AL-103	0.97	0.98	0.92	0.93
AL-104	0.85	0.89	0.85	NA*
AL-105	0.88	0.89	0.96	NA*
AL-106	0.86	0.97	0.91	NA*
AL-108	0.94	0.92	0.99	0.96
AL-109 Ref.	0.98	0.93	0.88	0.92
AL-110	0.94	0.96	NA*	0.93
AL-111	0.91	0.92	0.99	0.98
AL-112	0.89	0.97	0.99	NA*
AL-161	0.89	0.84	0.99	0.81
AL-162	0.87	0.94	0.99	NA*
AL-163	0.90	0.91	0.98	0.95
AZ-113	0.86	0.97	0.90	0.90
AZ-114	0.84	0.91	0.98	0.78
AZ-115	0.94	0.94	0.99	0.97
AZ-116	0.85	0.96	NA*	0.98
AZ-117	0.92	0.90	0.98	0.84
AZ-118	0.88	0.95	NA*	0.91
AZ-119	0.91	0.96	0.99	0.97
AZ-120	0.77	0.95	0.99	0.85
AZ-121	0.90	0.99	NA*	0.83
AZ-122 Ref.	0.99	0.95	0.90	0.70
AZ-123	0.88	0.95	0.99	0.78
AZ-124	0.98	0.92	0.97	0.97
AZ-161	0.95	0.91	0.85	0.87
AZ-162	0.86	0.99	NA*	0.93

Note: * Limited data; $p < 0.05$ for all cases; Ref = Reference section for master curve fitting; AL = Alabama; AZ = Arizona.

Table 6.2: Pearson's Correlation Coefficient for Shift Factors Based on Section Properties in Alabama

Section Properties	**Shift Factor (FC)**	**Shift Factor (WP)**	**Shift Factor (RD)**	**Shift Factor (TC)**
AC	0.037	-0.308	-0.055	-0.331
BT	-0.156	0.074	0.675	-0.335
N200P%	-0.506	-0.195	-0.149	-0.049
PI%	-0.111	0.239	0.007	0.214
SG	0.291	0.433	0.140	-0.147
MDD	-0.027	0.160	0.252	-0.356
OTM%	-0.126	-0.267	-0.259	0.316
MR	0.202	-0.052	0.234	-0.265
HC	0.524	0.280	0.043	0.226
SN	-0.264	-0.291	0.170	-0.606
AV %	0.129	0.072	0.569	-0.026
E_{star}	-0.585	-0.426	-0.358	-0.329
DD	NA	NA	NA	NA
MC%	NA	NA	NA	NA

Table 6.3: Pearson's Correlation Coefficient for Shift Factors Based on Section Properties in Arizona

Section Properties	**Shift Factor (FC)**	**Shift Factor (WP)**	**Shift Factor (RD)**	**Shift Factor (TC)**
AC	0.220	-0.322	0.272	0.511
BT	-0.160	0.101	-0.071	-0.130
N200P%	0.064	0.059	-0.181	-0.481
PI%	-0.515	-0.418	-0.060	-0.646
SG	0.242	0.019	0.355	-0.184
MDD	0.461	0.153	0.415	0.672
OTM%	-0.153	-0.056	-0.180	-0.548
MR	-0.331	-0.220	0.019	-0.263
HC	-0.435	-0.234	-0.093	0.159
SN	0.081	-0.261	-0.014	0.385
AV %	0.236	-0.147	0.676	0.076
E_{star}	0.349	0.100	-0.050	0.187
DD	-0.053	-0.093	-0.131	0.007
MC%	-0.140	0.221	-0.106	-0.350

Table 6.4: Models for Predicting Shift Factors for Alabama (Part a)

Model	**Intercept (a_0)**	**AC (a_1)**	**BT (a_2)**	**PI% (a_3)**	**SG (a_4)**	**MDD (a_5)**	**OTM% (a_6)**
FC	-1410	0.008	0	-2.025	527	0	0
WP	-1004	-0.017	0	3.080	378	0	-1.885
RD	-264	-0.008	0.031	-0.894	103.3	-0.008	0
TC	-27.9	0.005	-0.007	0.1774	12.8	0	0

Note: The equations are in the form of $a_0 + a_1x_1 + a_2x_2 + \cdots + a_{11}x_{11}$.
95% significance level; RMSE = Root Mean Square Error.

Table 6.5: Models for Predicting Shift Factors for Alabama (Part b, continued)

Model	**MR (a_7)**	**HC (a_8)**	**AV% (a_9)**	**E_{star} (a_{10})**	**N200P% (a_{11})**	**R^2**	**RMSE**	**P-Value**
FC	0	1245635	-0.491	-1.24×10^{-3}	0	0.83	4.98	0.035
WP	-0.756	1846698	0	-8.52×10^{-4}	0	0.88	5.42	0.046
RD	0	0	0.085	1.30×10^{-4}	0	0.88	1.048	0.048
TC	0	0	-0.086	-5.44×10^{-4}	-0.056	0.93	0.4	0.494

Note: The equations are in the form of $a_0 + a_1x_1 + a_2x_2 + \cdots + a_{11}x_{11}$.
95% significance level; RMSE = Root Mean Square Error.

Table 6.6: Models for Predicting Shift Factors for Arizona (Part a)

Model	**Intercept (b_0)**	**AC (b_1)**	**BT (b_2)**	**SG (b_3)**	**MDD (b_4)**	**OTM% (b_5)**	**MR (b_6)**	**HC (b_7)**
FC	-3547	0.281	0.159	1599	0.227	0	-1.761	-484849
WP	-4083	-0.351	0.016	907	0.727	26.13	0.762	-123717
RD	2.4	-0.162	-0.057	0	0	0	-0.020	93239
TC	1421	0.170	0.039	-570	0	-2.72	-0.224	19442

Note: The equations are in the form of $b_0 + b_1x_1 + b_2x_2 + \cdots + b_{11}x_{11}$.
95% significance level; RMSE = Root Mean Square Error.

Table 6.7: Models for Predicting Shift Factors for Arizona (Part b, continued)

Model	DD (b_8)	MC% (b_9)	AV% (b_{10})	E_{star} (b_{11})	N200P% (b_{12})	R^2	RMSE	P-Value
FC	-0.603	-10.6	0	7.32×10^{-3}	3.16	0.89	26.11	0.24
WP	-0.032	10.78	-14.79	2.94×10^{-3}	-1.24	0.99	3.81	0.22
RD	0	-2.90	4.38	-2.90×10^{-4}	0.57	0.92	3.04	0.55
TC	0.040	2.98	0.40	3.67×10^{-3}	-0.19	0.81	8.60	0.68

Note: The equations are in the form of $b_0 + b_1x_1 + b_2x_2 + \cdots + b_{11}x_{11}$.
95% significance level; RMSE = Root Mean Square Error.

Data visualization strategies were employed to support the analytical methodology and aid in the clarity of the conclusions. Scatter plots, line graphs, and other visual aids were used to show the relationships between pavement distresses and the factors that influence them. These visual aids were helpful in improving and assessing the data's interpretability and facilitating a deeper comprehension of the underlying relationships. For example, FC vs WP cracking and cumulative ESALs with master curves for Alabama are presented in Figures 6.2 and 6.3, respectively. Observed vs predicted WP shift factors for Arizona, and residual for this model showing its unbiased predictive capability, are presented in Figures 6.4 and 6.5, respectively.

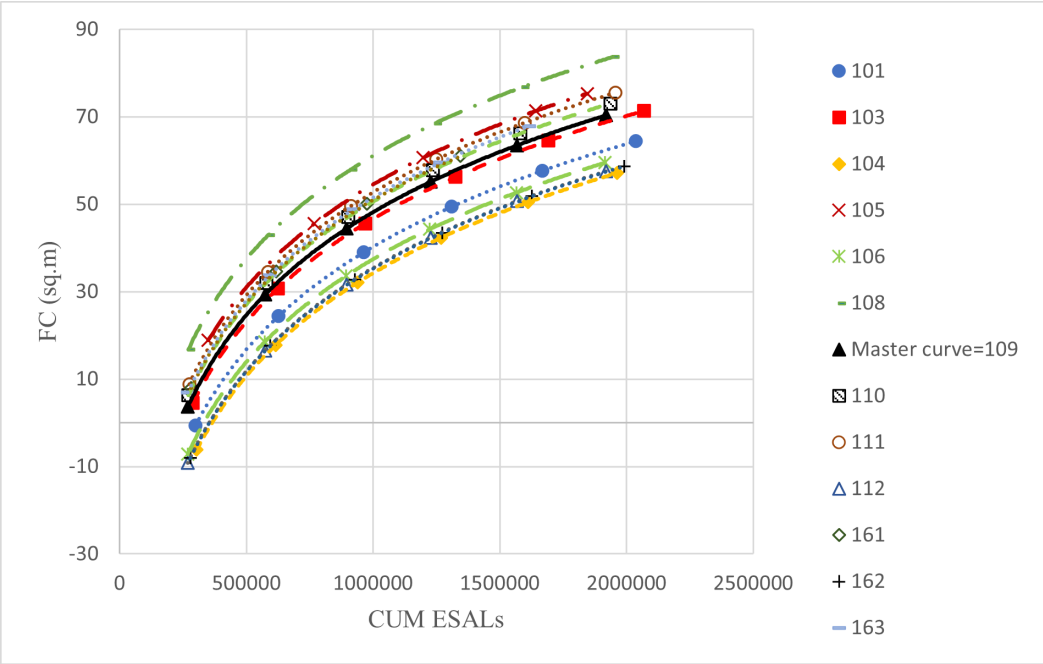

(a)

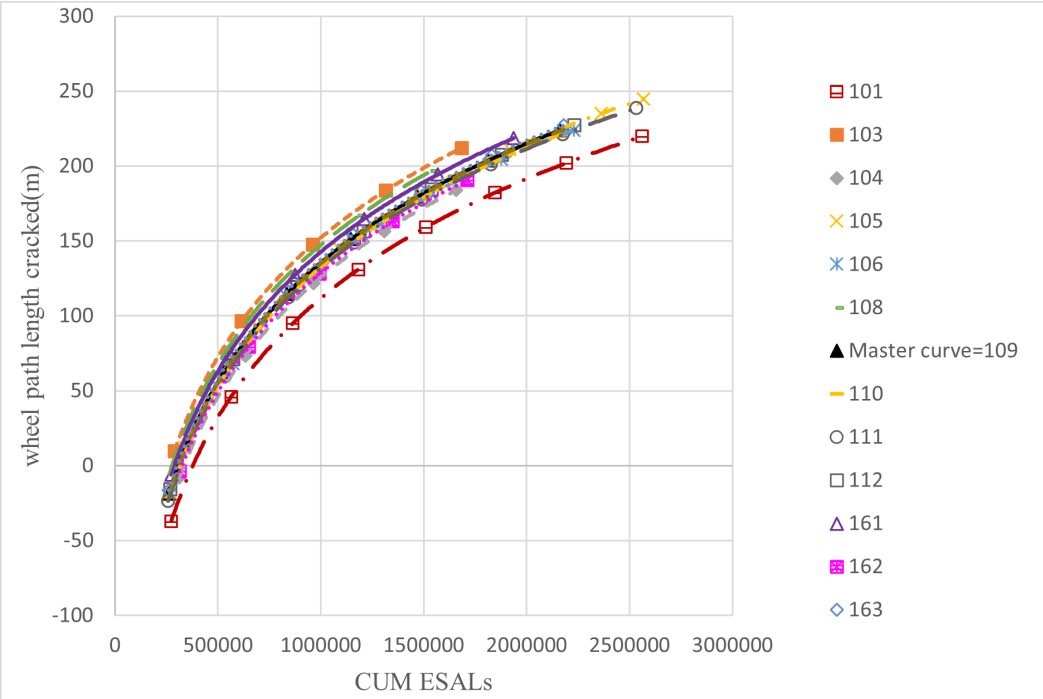

(b)

Figure 6.2: Relationship between (a) Fatigue Cracking (FC) and (b) Wheel Path Length Cracked (WP) with Cumulative ESALs with constant “a” for Alabama.

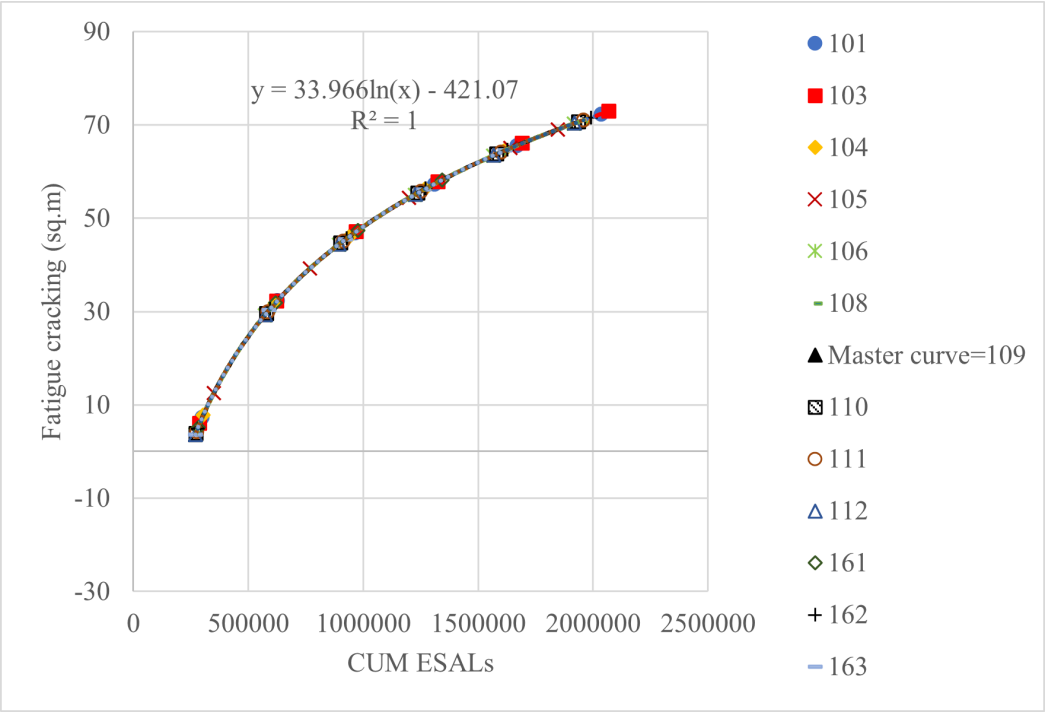

(a)

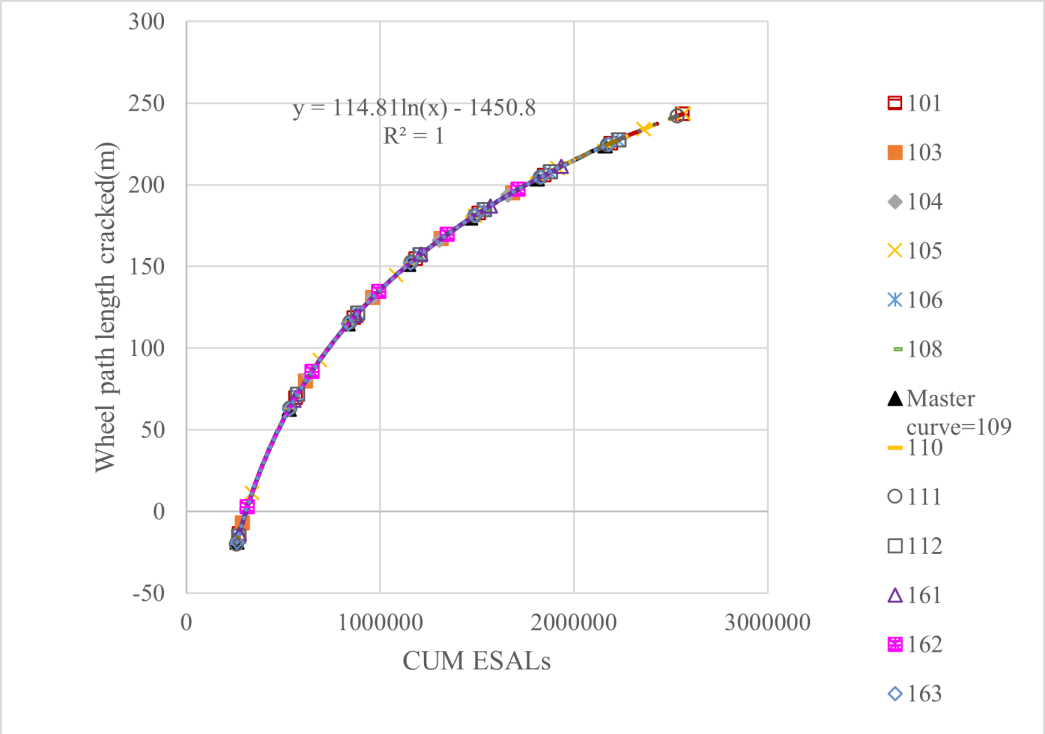

(b)

Figure 6.3: Master curves for (a) Fatigue Cracking (FC) and (b) Wheel Path Length Cracked in Alabama.

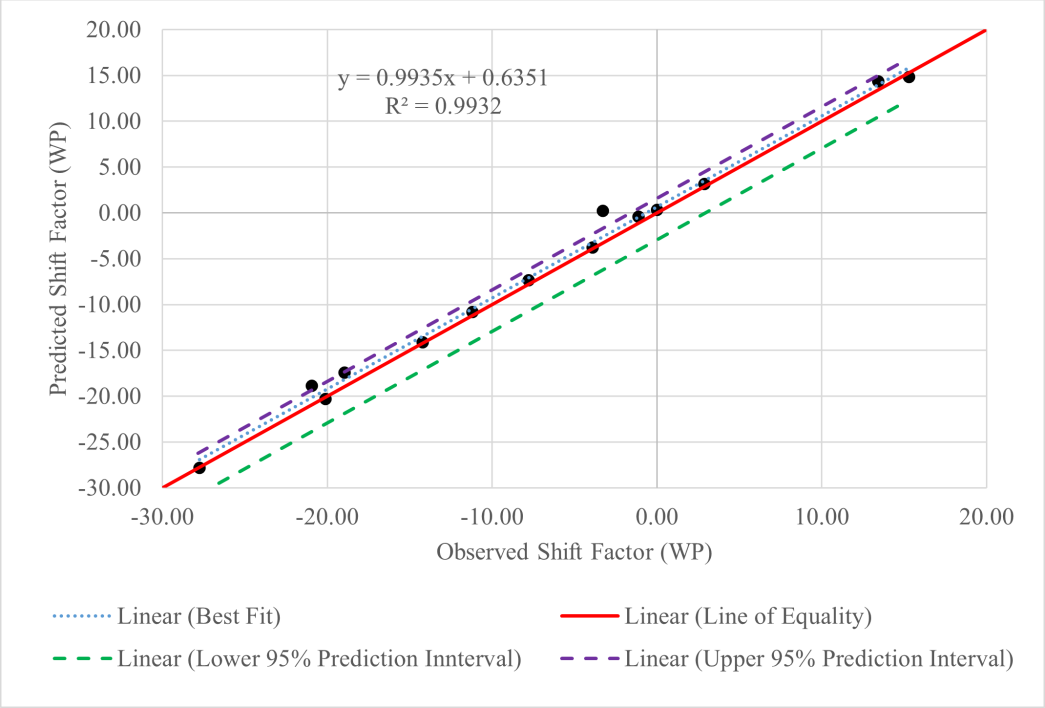

Figure 6.4: Example of comparison between observed and predicted WP shift factors for Arizona.

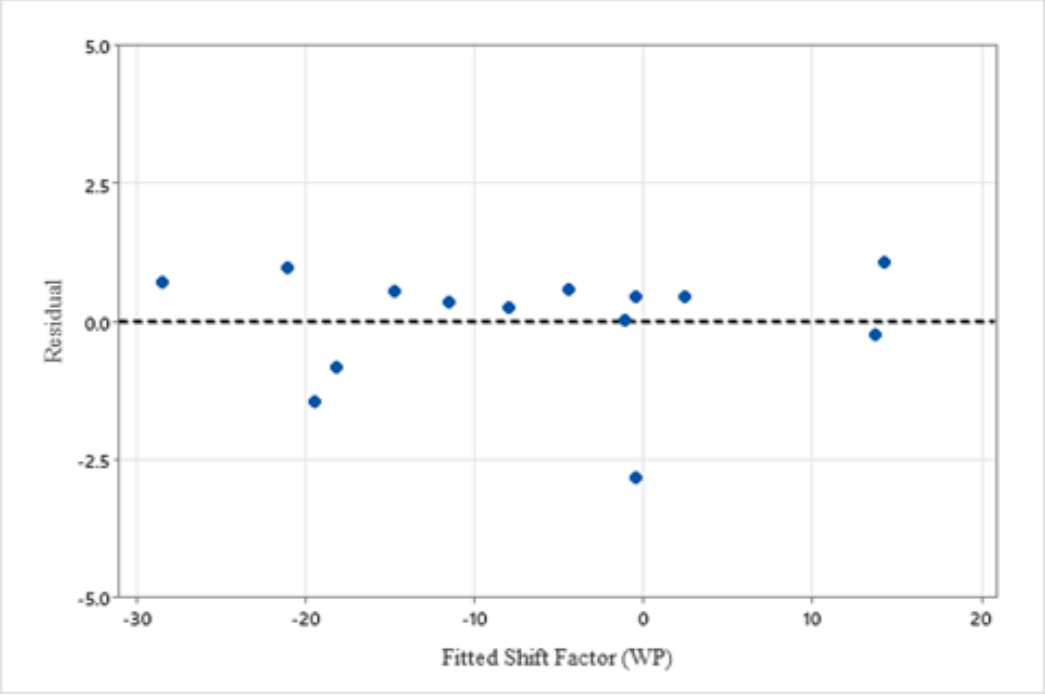

Figure 6.5: Example of comparison between WP model residuals for Arizona.

6.5 Modelling Approach and Results

In this study, four critical types of pavement distresses were considered: fatigue cracking, transverse cracking, rutting, and wheel path length cracking. Fatigue cracking and permanent deformation (rutting) have been identified by many states in the US as the key modes of asphalt mixture deterioration parameters [193]. In fact, several of the Balanced Mix Design (BMD) approaches developed in recent years for various states are based on mixture performance assessment primarily on these distress as well as durability [193–197].

As indicated earlier, several predictive relationship forms were reviewed to better fit the deterioration rate of such distresses over time and/or ESAL. These included linear, logarithmic, and exponential forms. Thus, it was concluded that a logarithmic regression model expressed as "$y = a\ln(x) + b$" well described the progression trends of such distresses. The R^2 values are presented in Table 6.1. The model consistently demonstrated strong predictive ability across multiple LTTP sections, as evidenced by the R^2 values, predominantly above 0.9 and p values less than 0.05, indicating (i) a strong relationship between distresses and cumulative ESALs and (ii) consistent model structure across all sections.

It is to be noted that the data for fatigue cracking and "wheel path length cracked" for some sections, like Section 102, were insufficient due to limited surveys reported in the LTPP database, and poor continuity over time in intervals among surveys did not permit computation of meaningful trends in deterioration. Nevertheless, uniformity in model form and fitting the observed distress deterioration rates, suggest that the "master curve" concept may apply more widely to similar asphalt sections with identical material and structural properties like asphalt concrete (AC) and base layer thicknesses, mix design parameters (like air voids, resilient mod-

ulus, and dynamic modulus), and subgrade properties like specific gravity and plasticity index. In addition, local construction practices, environmental exposure (i.e., climatic zone), and traffic loading in terms of ESALs were considered implicitly by selecting sections within each state for consistency. Accordingly, shift functions were developed between the same distress type deterioration curves of the various pavement sections that overlap, producing a consistent generalized master curve. These shift functions were quantified in terms of specific section attributes such as mixture stiffness, hydraulic conductivity, and asphalt air void content, as elaborated further in Tables 6.8, 6.9, 6.10, and 6.11.

Table 6.8: Shift Factors and Selected Material Properties for Alabama Sections

Section	**Shift Factor** (FC)	**Shift Factor** (WP)	**Shift Factor** (RD)	**Shift Factor** (TC)	**AC** (mm)	**BT** (mm)	**N200P** (%)	**PI** (%)
101	-7.93	-23.58	-1.18	-0.40	187.96	200.66	68.0	14
102	NA	NA	-0.43	-0.07	106.68	304.80	57.2	15
103	-1.53	16.77	-3.24	1.13	106.68	187.96	68.0	18
104	-13.96	-9.62	-1.92	NA	160.02	309.88	71.6	17
105	6.31	0.99	-1.56	NA	104.14	205.74	64.3	17
106	-10.76	-3.40	1.33	NA	175.26	416.56	72.3	17
108	12.88	11.96	0.21	-0.02	182.88	309.88	66.4	14
109*	0.00	0.00	0.00	0.00	180.34	414.02	64.3	21
110	2.40	-2.80	NA	0.91	187.96	195.58	61.0	15
111	4.53	-3.53	0.00	0.14	91.44	299.72	70.9	18
112	-12.78	-0.48	-0.26	NA	83.82	401.32	71.6	17
161	2.75	7.31	0.37	1.05	104.14	297.18	64.3	17
162	-12.92	-6.65	0.35	NA	99.06	251.46	64.3	17
163	3.35	2.13	4.87	0.28	106.68	414.02	64.3	17

Table 6.9: Additional Material Properties for Alabama Sections

Section	**SG** (-)	**MDD** (kg/m^3)	**OTM** (%)	**MR** (MPa)	**HC** (cm/s)	**SN** (-)	**AV** (%)	**Estar** (MPa)
101	2.731	1665.92	20	68.26	4.30E-06	5.152	6.95	9460.88
102	2.744	2018.33	12	92.39	1.95E-05	4.728	5.28	8360.54
103	2.748	1633.88	20	61.36	8.90E-06	3.624	8.59	7159.05
104	2.734	1858.14	16	70.33	4.30E-06	5.700	1.58	16172.02
105	2.748	1778.05	17	77.22	8.90E-06	3.428	4.43	12189.62
106	2.734	2050.36	12	68.95	4.30E-06	6.332	1.88	12189.62
108	2.748	2050.36	10	70.33	8.90E-06	5.456	4.32	7834.92
109*	2.757	1778.05	17	99.97	8.90E-06	6.076	1.56	9778.12
110	2.710	1729.99	18	80.67	1.95E-05	4.689	4.46	7800.75
111	2.739	1681.94	19	71.71	8.90E-06	3.771	2.41	7796.28
112	2.729	1858.14	16	70.33	4.30E-06	4.375	2.45	7796.28
161	2.748	1778.05	17	77.22	8.90E-06	4.132	1.26	7800.75
162	2.748	1778.05	17	77.22	8.90E-06	4.092	8.96	16663.21
163	2.748	1778.05	17	77.22	8.90E-06	4.431	22.06	3972.03

Table 6.10: Shift Factors and Selected Material Properties for Arizona Sections

Section	**Shift Factor** (FC)	**Shift Factor** (WP)	**Shift Factor** (RD)	**Shift Factor** (TC)	**AC** (mm)	**BT** (mm)	**N200P** (%)	**PI** (%)	**SG** (-)
113	-10.79	-11.19	0.03	-4.19	124.46	190.50	8.8	NA	2.731
114	-8.94	-20.10	5.75	-0.26	185.42	304.80	18.3	7	2.740
115	68.64	15.29	-0.95	2.39	167.64	215.90	24.7	2	2.740
116	-1.47	-1.12	NA	2.24	114.30	307.34	16.3	NA	2.740
117	65.11	-14.20	2.08	15.87	187.96	208.28	17.2	NA	2.740
118	-2.66	-20.94	NA	-21.45	111.76	299.72	30.8	13	2.749
119	109.64	2.89	8.47	4.02	160.02	220.98	13.2	NA	2.740
120	-3.50	-7.78	-0.86	-3.38	114.30	302.26	24.4	14	2.731
121	-3.78	13.42	NA	-2.72	116.84	406.40	15.8	10	2.745
122*	0.00	0.00	0.00	0.00	119.38	358.14	18.6	NA	2.740
123	-5.92	-3.28	-4.92	-0.16	172.72	297.18	14.0	NA	2.731
124	-4.79	-27.75	2.33	5.30	170.18	401.32	14.6	NA	2.740
161	-6.10	-3.91	1.15	0.06	157.48	96.52	15.3	2	2.717
162	-6.70	-18.95	NA	0.51	228.60	0.00	9.4	NA	2.731

Table 6.11: Additional Material Properties for Arizona Sections

Section	MDD (kg/m^3)	OTM (%)	MR (MPa)	HC (cm/s)	SN (-)	AV (%)	Estar (MPa)	DD (kg/m^3)	MC (%)
113	2018.33	10	52.40	2.70E-05	2.996	7.61	11421.65	2212.76	2.90
114	2130.46	8	115.14	1.10E-05	4.556	11.86	11533.39	2235.90	2.70
115	2114.44	9	62.05	1.10E-05	4.278	7.53	11861.51	2255.70	2.70
116	2162.49	8	59.98	6.90E-05	4.206	11.04	11533.39	2275.84	3.40
117	2146.47	8	62.05	1.10E-05	4.646	10.70	13176.16	2229.69	4.00
118	2018.33	10	78.60	7.70E-06	3.812	10.54	10949.40	2257.00	4.80
119	2210.55	8	38.61	5.40E-06	4.277	11.39	10439.18	2204.63	3.10
120	2066.38	8	82.74	2.70E-05	3.622	8.43	10658.89	2175.09	5.20
121	2114.44	8	76.53	6.35E-05	4.118	10.15	10439.18	2203.72	5.10
122*	2114.44	8	62.05	1.00E-05	4.090	9.10	10111.20	2288.19	4.00
123	2162.49	8	66.19	2.70E-05	5.508	9.32	11113.22	2239.68	2.60
124	2146.47	8	62.05	1.10E-04	6.393	9.66	9174.05	2274.31	2.50
161	2082.40	10	35.16	4.30E-05	3.154	7.49	7536.00	2190.44	4.60
162	2162.49	8	46.88	6.35E-05	3.960	7.55	9397.78	2201.79	2.40

6.5.1 Developing Master Curves for FC, WP, RD, and TC

For the development of the master curves for each one of the pavement distress types, the following steps were used:

1. **Logarithmic Modeling:** The general form of the logarithmic function was used, $y = a\ln(\text{Cumulative ESALs}) + b$, in which the shift coefficients of $\ln(\text{Cumulative ESALs})$, "$a$", "$a'$", "$a''$", and "$a'''$", were fixed to a constant slope value (i.e., a = average of all "a" coefficients for FC; a' = average of all "a'" coefficients for WP; a'' = average of all "a''" coefficients for RD; and a''' = average of all "a'''" coefficients for TC, respectively). The new coefficients, "b", "b'", "b''", and "b'''", for each distress were then calculated using the fixed slope for the corresponding distress types, in order to vertically shift each section's curve to ensure that all section curves remain parallel to the master curve without intersects,

allowing consistent visual and analytical comparison across sections. An example of such function coefficients and corresponding R^2 values is provided in Table 6.12 for FC and WP for Alabama. The results are graphically presented in Figure 6.2. A similar approach and results were used for the remaining distressed and the second state data.

Table 6.12: Modified Equations of Best Fit for FC and WP in Alabama

Section	**Shift Factor (FC) vs ESALs** $y = \beta_1 \cdot \ln(x) + \alpha_1$	α_1 (FC) R^2	**Shift Factor (WP) vs ESALs** $y = \beta_2 \cdot \ln(x) + \alpha_2$	α_2 (WP) R^2
AL-101	$33.966 \cdot \ln(x) - 429$	1	$114.81 \cdot \ln(x) - 1474.3$	1
AL-103	$33.966 \cdot \ln(x) - 422.6$	1	$114.81 \cdot \ln(x) - 1434$	1
AL-104	$33.966 \cdot \ln(x) - 435.03$	1	$114.81 \cdot \ln(x) - 1460.4$	1
AL-105	$33.966 \cdot \ln(x) - 414.76$	1	$114.81 \cdot \ln(x) - 1449.8$	1
AL-106	$33.966 \cdot \ln(x) - 431.83$	1	$114.81 \cdot \ln(x) - 1454.2$	1
AL-108	$33.966 \cdot \ln(x) - 408.19$	1	$114.81 \cdot \ln(x) - 1438.8$	1
AL-109*	$33.966 \cdot \ln(x) - 421.07$	1	$114.81 \cdot \ln(x) - 1450.8$	1
AL-110	$33.966 \cdot \ln(x) - 418.67$	1	$114.81 \cdot \ln(x) - 1453.6$	1
AL-111	$33.966 \cdot \ln(x) - 416.54$	1	$114.81 \cdot \ln(x) - 1454.3$	1
AL-112	$33.966 \cdot \ln(x) - 433.85$	1	$114.81 \cdot \ln(x) - 1451.2$	1
AL-161	$33.966 \cdot \ln(x) - 418.32$	1	$114.81 \cdot \ln(x) - 1443.5$	1
AL-162	$33.966 \cdot \ln(x) - 433.99$	1	$114.81 \cdot \ln(x) - 1457.4$	1
AL-163	$33.966 \cdot \ln(x) - 417.72$	1	$114.81 \cdot \ln(x) - 1448.6$	1

Note: α_1: Intercept (values are relative to the master curve intercept, $\alpha_{\text{master}} = -421.07$).
α_2: Intercept (relative to the master curve intercept, $\alpha_{\text{master}} = -1450.8$).
AL-109* denotes the master curve section.
β_1 (slope) for all equations is constant at 33.966.
β_2 (slope) for all equations is constant at 114.81.

2. **Selection of the Reference Section:** The reference section for which to develop the "master curve," representative of the general deterioration trend for distresses and states, was then selected. For example, section 109 was selected for Alabama, Table 6.12. Thus, by following this approach, the specific distress deterioration functions for all pavement sections overlap onto the selected pavement section for defining the master curve. This pavement section can be chosen so that its deterioration curve is centered on the remain-

ing sections. An example of such an approach is depicted in Figure 6.2 with Section 109 chosen at the center of all pavement sections' functions.

3. **Computation of Shift Factors:** The shift factors are then derived by the vertical difference of each curve from the reference master curve function, in the example reported here, Section 109. This permitted to development of the master curves examples shown for both Fatigue Cracking, FC, and Wheel Path Length Cracked, WP, in Figure 6.3.

4. **Relating Shift Function to Mixture Properties:** The shift functions for each pavement section were then related to the specific mixture properties. In other words, the difference in distress deterioration progress for each pavement section is related to the material and pertinent pavement design considerations. Environmental factors may be of importance as well; however, since all sections and materials were within a specific state, these were not relevant in such an analysis since they were all the same for all sections. A Pearson correlation analysis was performed to determine which asphalt section properties better represent the effect of shift functions between sections. The results of the analysis, along with the shift factors for each section, are included in Tables 6.8, 6.9, 6.10, and 6.11. A summary of Pearson's correlation coefficients is included in Tables 6.2 and 6.3. Next, a multivariate linear regression was used to develop a predictive equation for the shift factors, given by Equation (6.1):

$$y = b_0 + x_1\beta_1 + x_2\beta_2 + x_3\beta_3 + \varepsilon \tag{6.1}$$

Where, y is the dependent variable, X_i is the predictor, β_i is the coefficient to be optimized,

and ε is the residual error, which aims to be minimized for increasing the predictive power of a model. This model's derivation is discussed further in referenced literature [198].

Bivariate analysis on the shift factors and each one of these selected variables indicated that the best relationships are linear. To describe the shift factors, linear relationships for each one (FC, WP, RD, and TC) are presented in Tables 6.4, 6.5, 6.6, and 6.7. In selecting the best models, R^2, p-value, residual standard error, and simplicity of the model are considered (i.e., highest R^2 and $p < 0.05$). Root-mean-squared error (RMSE) is a metric that quantifies the standard deviation of the residuals, reflecting the average difference between the predicted values and the actual values in a statistical model. The lower the RMSE, the better the model. The resulting models are presented in Tables 6.4, 6.5, 6.6, and 6.7, and the following equations:

$$\begin{aligned}\text{(FC, WP, RD, TC)}_{\text{AL}} = a_0 &+ a_1\text{AC} + a_2\text{BT} + a_3\text{PI\%} + a_4\text{SG} + a_5\text{MDD} \\ &+ a_6\text{OTM\%} + a_7\text{MR} + a_8\text{HC} + a_9\text{AV\%} + a_{10}E^* + a_{11}\text{N200P\%}\end{aligned} \tag{6.2}$$

$$\begin{aligned}\text{(FC, WP, RD, TC)}_{\text{AZ}} = b_0 &+ b_1\text{AC} + b_2\text{BT} + b_3\text{SG} + b_4\text{MDD} + b_5\text{OTM\%} \\ &+ b_6\text{MR} + b_7\text{HC} + b_8\text{DD} + b_9\text{MC\%} + b_{10}\text{AV\%} + b_{11}E^* + b_{12}\text{N200P\%}\end{aligned} \tag{6.3}$$

where Fatigue Cracking (FC) is measured in square meters (m^2) and Wheel Path Length Cracked (WP) in meters (m); Average Rut Depth (RD) and Transverse Cracking Length (TC)

are measured in millimeters (mm) and meters (m), respectively, indicating surface deformations. Asphalt and Base Thicknesses (AC and BT) are reported in inches (mm). Subgrade characteristics include No. 200 Sieve Passing (N200P%) and Plasticity Index (PI%) expressed as percentages (%), Specific Gravity (SG) as a unitless ratio, Maximum Laboratory Dry Density (MDD) in kilograms per cubic meter (kg/m^3), Optimum Laboratory Moisture (OTM%) in percent (%), Hydraulic Conductivity (HC) in centimeters per second (cm/s), and Resilient Modulus (MR) in mega pascals (MPa). Additionally, Structural Number (SN) is unitless, Asphalt Air Voids (AV%) and Moisture Content (MC%) are expressed in percent (%); Dynamic Modulus of Asphalt (Estar) is in mega pascals (MPa), Aggregate Dry Density (DD) is reported in kilograms per cubic meter (kg/m^3).

An example of the predicted versus observed shift factors of WP in Arizona is plotted in Figure 6.4. Due to variability in mixture properties data from several sections for defining the shift functions, differences between "predicted" (i.e., calculated from mixture properties) and the "observed" (i.e., estimated for the deterioration curves shifting) values were expected. Such deviations from the equality line, $y = x$, are shown in Figure 6.4. Overall, for wheel path (WP) distress in Arizona, the predicted values show a strong agreement with the observed data ($R^2 = 0.99$), with most of the predictions within the 95% interval. An example of model validation summarizing observed and predicted shift factors for three types of distress (FC, WP, TC) for the selected Arizona sections is presented in Table 6.13. The other types of distress and states follow similar predictive behaviour, omitted herein for manuscript length limitations.

Figure 6.5 presents the residuals for the WP shift function predictions in Arizona. The residual plot shows a random variation (i.e., no clear pattern or trend) in relation to the shift factor scale and thus indicates unbiased predictions from smaller to larger values.

Table 6.13: Model validation for shift factors in Arizona sections.

Section	Distress	Observed Shift Factor	Predicted Shift Factor	Error	% Error
117.00	FC	65.11	56.74	8.37	12.86
	WP	-14.20	-14.14	-0.06	0.42
	TC	15.87	14.31	1.56	9.83
119.00	FC	109.64	101.42	8.22	7.50
	WP	2.89	3.12	-0.23	-7.96
	TC	4.02	2.50	1.52	37.81
121.00	FC	-3.78	-2.44	-1.34	35.45
	WP	13.42	14.34	-0.92	-6.86
	TC	-2.72	-2.89	0.17	-6.25

Note: Error = Observed $-$ Predicted; % Error = |Error| / |Observed| $\times$ 100

6.6 Summary and Conclusions

The analysis and results of this study provided an alternative approach for modelling pavement distress predictions based on the "master curves" concept. Among the various distresses, fatigue cracking, transverse cracking, permanent deformation (i.e., rutting), and wheel path length cracked (WP) of asphalt sections were explored. Based on the suggested approach, asphalt pavement distress deterioration functions were proposed using "master curves." Using the historical distress data in the LTPP database for asphalt pavements in two states, the following findings were observed:

- Based on the pavement distress data reported in the database, a logarithmic model represents well the distress deterioration functions over time, and/or ESALs, with a high value of coefficients of determination (i.e., above 0.9, with a p-value < 0.05). This indicated that this model form well fits the distress data reported and used in this study. Consequently,

this led to the development of "master curves" for these distresses.

- The shift factors for the "master curve" modeling approach were successfully related to the specific asphalt section properties. Pearson's correlation analysis provided an initial assessment of which mixture properties were more critical in defining such shift functions. For example, alternative model fitting led to the inclusion of factors such as asphalt layer thickness, plasticity index, specific gravity, hydraulic conductivity, asphalt air voids, and dynamic modulus of asphalt for fatigue cracking (FC) in Alabama. The prediction accuracy of the selected models ranged from 83% to 93% for Alabama and 81% to 99% for Arizona (Tables 6.4, 6.5, 6.6, and 6.7).

- The shift factor equations were defined using multivariate linear regression analysis. The resulting "master curves" for distresses provided an excellent fit ($R^2 = 1$, Figure 6.3).

Since pavement distresses are section-specific, this modeling approach has the advantage of developing prediction functions for a group of asphalt mixtures with comparable properties and under similar climatic conditions. This represents an advantage to more accurate predictions since distress predictions based on a vast set of distress data representing a wide range of pavement structures often produce lower accuracy predictions due to the large variability in input data. Thus, the proposed approach of "master curves" development for distress data in this study is an effective direction for accurate predictions in regards to distresses, such as fatigue cracking, permanent deformation (i.e., rutting).

Highway agencies can use the proposed approach for developing their own distress prediction models using their own distress data and representing the materials and pavement construction practices in their state.

Chapter 7: Conclusions and Recommendations

This dissertation presented an extensive evaluation and assessment of pavement markings friction at pedestrian crosswalks in regards the two critical elements of pedestrian slip resistance and vehicle skid friction. Recognizing the importance of pavement markings to public safety, especially across various environmental conditions, the research focused on the need for a robust evaluation measures that leverage laboratory testing, field verification, texture analysis, and predictive modeling. The primary motivation stemmed from the absence of supporting vehicular friction over pedestrian safety, and the shortfall of the specifications and acceptance testing neglected the latter. To address these, it was the objective of this research to consider integrating experimental testing, imaging, statistical and machine learning modeling for analyzing and predicting the friction performance of pavement markings.

The study assessed the friction performance of various Maryland-used pavement marking materials with the British Pendulum Tester (BPT) for dry, wet, and icy road conditions. BPT was used for both tire skid friction and pedestrian slip resistance. Laboratory test results were in agreement with field conditions, linking well the use of controlled laboratory testing for predicting actual-world field performance. Traffic wear (i.e., wheel path vs. non-wheel path) and environmental conditions had notable impacts, affirming the necessity for friction specifications that account for these. The findings contribute to national dialogue on how to improve pedestrian safety at crosswalks and reinforce recommendations to revise state-level acceptance specifications.

To validate the field and QA process reliably, reproducibility and repeatability of BPT units was assessed with a controlled round robin study. Two units were tested under identical conditions on various materials, surface conditions and environments, providing a satisfactory and consistent results. Paired t-tests and MANOVA were used to ensure that measurements from the two units were statistically equivalent. These findings enable contractors and agencies to apply different BPT units with confidence while having consistent standardization for acceptance testing and quality control.

The study was further extended through measurements of the micro- and macro-texture pavement marking characteristics using the Aggregate Image Measurement System (AIMS). Differences in surface texture among the tested materials were assessed using the RMS, MPD, and MTD indices. Asphalt surfacing with no markings had the highest texture values, and preformed thermoplastic markings had the lowest surface profiles. The RMS measure showed great agreement with BPN measurements and illustrated its value as a predictive measure of friction performance. This imaging-based assessment enabled a link to the "ground-truth" surface conditions and providing insights into the contribution of texture to slip and skid resistance. This also provides the possibility of using AIMS as a potential laboratory-based assessment tool for friction assessment.

The supervised machine learning models were trained to predict BPN (TSR) from an extensive set of 1,092 laboratory and field measurements. Five models, (i.e., Random Forest, XGBoost, Support Vector Regression, Gaussian Process Regression, and Multilayer Perceptron), were trained on categorical and numerical features such as material type, surface condition, test environment, temperature, and device type. Among them, ensemble models (XG and RF) performed best in prediction accuracy with almost 0.95 R^2 values and the lowest RMSE. Tests of

residuals, like K–S tests, and empirical cumulative distribution functions also confirmed that the residuals of all models except SVR were normally distributed. Feature importance evaluation identified surface condition, material type, and environment as the most significant predictors. These findings demonstrate the potential of machine learning to complement physical testing and support data-based decision-making in pavement marking assessment.

The master curve-based method to predict asphalt pavement distresses utilizing Long-Term Pavement Performance (LTPP) program data provided good results. Alabama and Arizona historical distress data were predicted using logarithmic deterioration functions for fatigue cracking and rutting. The resulting master curves had a very good fit to the observed data with R^2 greater than 0.9 for all the cases. Shift functions were created so that distress progression could be modeled using section-specific parameters such as asphalt thickness, air voids, plasticity index, and dynamic modulus. This approach offers agencies a modeling solution for developing prediction models based on their historical records enhancing accuracy of predictions, reducing need for time consuming and costly field surveys, and enable them to integrate such models in their PMS for better pavement management planning.

Future research can consider incorporating long-term friction degradation trends into the machine learning algorithm, investigating other surface variables such as retroreflectivity, and validating predictive models over broader climatic and geographic regions. Further research into footwear, tire material and pavement surface contaminants can also help clarify mechanisms of friction under crosswalks and expand the transferability of the results and models. Lastly, this dissertation lays a good foundation for improving the safety of pedestrians and vehicles at critical road interfaces by combining engineering rigor, innovative modeling and practical relevance.

Bibliography

[1] Mosbock, H., and Burghardt, T. E. (2016, October). *The importance of road markings for road safety and modern traffic management*. Presented at the 1st European Road Infrastructure Congress, Leeds, United Kingdom. https://www.researchgate.net/publication/326735862_The_Importance_of_Road_Markings_for_Road_Safety_and_Modern_Traffic_Management.

[2] Park, E. S., Andersen, C. K., and Leader, R. T. (2008). *The benefits of pavement markings: A renewed perspective based on recent and ongoing research*. U.S. Federal Highway Administration. https://highways.dot.gov/sites/fhwa.dot.gov/files/2022-09/no090488.pdf.

[3] Dougald, L., Cottrell, B., Kweon, Y.-J., and Lim, I.-K. (2014). *Investigation of the safety effects of edge and centerline markings on narrow, low-volume roads*. Virginia Department of Transportation. Report No. VTRC 14-R3. http://www.virginiadot.org/vtrc/main/online_reports/pdf/14-r3.pdf.

[4] Harlow, A. (2005, May). *Skid resistance and pavement marking materials*. In *International Surface Friction Conference: Roads and Runways—Improving Safety Through Assessment and Design*, Christchurch, New Zealand. https://nzta.govt.nz/assets/resources/surface-friction-conference-2005/8/docs/skid-resistance-pavement-marking-materials.pdf.

[5] Zaid, N. B. M., Hainin, M. R., Idham, M. K., Warid, M. N. M., and Naqibah, S. N. (2019). *Evaluation of skid resistance performance using British pendulum and grip tester*. In *IOP Conference Series: Earth and Environmental Science*, 220(1), 012016. IOP Publishing. https://doi.org/10.1088/1755-1315/220/1/012016.

[6] Nassiri, S. (2018). *Evaluation of motorcyclists' and bikers' safety on wet pavement markings* (Master's thesis, University of Washington). http://hdl.handle.net/1773/43493.

[7] Asi, I. M. (2007). Evaluating skid resistance of different asphalt concrete mixes. *Building and Environment*, 42(1), 325–329. https://doi.org/10.1016/j.buildenv.2005.08.020.

[8] Sharafeldin, M., Albatayneh, O., Farid, A., and Ksaibati, K. (2022). A Bayesian approach to examine the impact of pavement friction on intersection safety. *Sustainability*, 14(19), 12495. https://doi.org/10.3390/su141912495.

[9] Goulias, D. G., and Awoke, G. S. (2020). Novel approach to pavement friction analysis with advanced statistical methods using structural equation modelling. *International Journal of Pavement Engineering*, 21(2), 236–245. https://doi.org/10.1080/10298436.2018.1454922.

[10] Bao, J., Zhao, H., Jiang, Y., and Li, S. (2025). International perspectives on skid resistance requirements for pavement markings: A comprehensive synthesis and analysis. *Lubricants*, 13(1), 29. https://doi.org/10.3390/lubricants13010029.

[11] Domínguez, J. L., Sanguino, T. M., Gonzalez, M. R., and Martin, J. D. (2024). Improving road safety through a novel crosswalk: Comprehensive material study with photoluminescent resin. *Engineering Science and Technology, an International Journal*, 57, 101793. https://doi.org/10.1016/j.jestch.2024.101793.

[12] Burghardt, T. E., Chistov, O., Reiter, T., Popp, R., Helmreich, B., and Wiesinger, F. (2023). Visibility of flat line and structured road markings for machine vision. *Case Studies in Construction Materials*, 18, e02048. https://doi.org/10.1016/j.cscm.2023.e02048.

[13] Rasol, M., Schmidt, F., Ientile, S., Adelaide, L., Nedjar, B., Kane, M., and Chevalier, C. (2021). Progress and monitoring opportunities of skid resistance in road transport: A critical review and road sensors. *Remote Sensing*, 13(18), 3729. https://doi.org/10.3390/rs13183729.

[14] Dehnad, M. H., and Yazdi, A. (2024). A review of numerical and experimental studies on hydroplaning of vehicles in motion on road surfaces. *Results in Engineering*, 23, 102438. https://doi.org/10.1016/j.rineng.2024.102438.

[15] Chu, L., Guo, W., and Fwa, T. F. (2022). Theoretical and practical engineering significance of British pendulum test. *International Journal of Pavement Engineering*, 23(1), 1–8. https://doi.org/10.1080/10298436.2020.1726351.

[16] Luo, H., Zheng, Y., Yan, J., Wu, X., and Huang, X. (2023). Prediction of pavement friction coefficient based on dynamic fraction test simulation. *Tribology International*, 189, 108999. https://doi.org/10.1016/j.triboint.2023.108999.

[17] Zhang, X., Chang, R., Xu, Z., Wang, J., and Tan, Z. (2024). Research on the influencing factors of anti-skid performance evaluation of asphalt pavement based on lateral force testing system. *Frontiers in Materials*, 11, 1410542. https://doi.org/10.3389/fmats.2024.1410542.

[18] Kohout, T., Vrtal, P., Hoffmann, A., and Blodek, T. (2023). The possibilities of utilising the skiddometer T2GO for forensic engineering. *Acta Polytechnica CTU Proceedings*, 42, 37–45. https://doi.org/10.14311/APP.2023.42.0037.

[19] Chen, W., Zhang, Z., Wei, J., Zhang, X., Wu, W., Sun, Y., and Wang, G. (2025). Study on skid resistance of asphalt pavements under macroscopic and microscopic texture features: A review of the state of the art. *Applied Sciences*, 15(12), 6819. https://doi.org/10.3390/app15126819.

[20] Guo, W., Chu, L., and Fwa, T. F. (2021). Mechanistic harmonization of British pendulum test measurements. *Measurement*, 182, 109618. https://doi.org/10.1016/j.measurement.2021.109618.

[21] Purohit, K., Rahman, M., Price, A., and Woodside, A. (2020). Assessment of preformed 3D-thermoplastic road markings for long-term durability, skid resistance and texture functionality. In *Proceedings of the 9th International Conference on Maintenance and Rehabilitation of Pavements—Mairepav9* (pp. 965–974). Springer International Publishing. https://doi.org/10.1007/978-3-030-48679-2_90.

[22] Cui, X., Guo, W., Fwa, T. F., and Chu, L. (2022). Improved interpretation of British pendulum test measurements for evaluation of floor slip resistance. *Journal of Testing and Evaluation*, 50(3), 1403–1414. https://doi.org/10.1520/JTE20210695.

[23] Chimich, D. D., Al-Salehi, L., Elkin, B. S., and Siegmund, G. P. (2022). Contaminant film thickness affects walkway friction measurements. *Frontiers in Public Health*, 10, 915140. https://doi.org/10.3389/fpubh.2022.915140.

[24] Fan, T. (2023). Research status of anti-slip characteristics of asphalt pavement for vehicle turning and braking stability. *International Core Journal of Engineering*, 9(7), 339–344. https://www.icj-e.org/download/ICJE-9-7-339-344.pdf.

[25] Kumar, A., Tang, T., Gupta, A., and Anupam, K. (2023). A state-of-the-art review of measurement and modelling of skid resistance: The perspective of developing nation. *Case Studies in Construction Materials*, 18, e02126. https://doi.org/10.1016/j.cscm.2023.e02126.

[26] Biswas, B. P., Hossain, M. S., and Tarefder, R. A. (2025). Correlation of wet and dry skid resistance: British pendulum tester versus locked wheel skid trailer. *Airfield and Highway Pavements 2025*, 20–34. https://doi.org/10.1061/9780784486214.003.

[27] Brassard, J. D., Beaulieu, A., Tremblay, M. M., and Momen, G. (2022). Assessment of runway surface conditions by British pendulum testing under the global reporting format winter conditions. *Applied Sciences*, 12(19), 9646. https://doi.org/10.3390/app12199646.

[28] Kumar, A., and Gupta, A. (2021). Review of factors controlling skid resistance at tire-pavement interface. *Advances in Civil Engineering*, 2021, 1–16. https://doi.org/10.1155/2021/2733054.

[29] Mazlan, R., Mohd Lazi, M. K. A., Mohd Jakarni, F., Kamarudin, S. N. N., Shahrin, M. I., Zolkepli, M. F., Hassan, S. A., and Mohd Warid, M. N. (2025). Skid resistance measuring techniques using portable testing tools for road application. *Recent Trends in Civil Engineering and Built Environment*, 6(1), 284–297. https://penerbit.uthm.edu.my/periodicals/index.php/rtcebe/article/view/17945.

[30] Muralidharan, K., Vignesh, V., Vignesh, R. V., Govindaraju, M., Baghad, A., Narassima, M. S., and Siengchin, S. (2024). Comprehensive overview of nano, micro, and macro tribometers in practice. *Journal of Bio-and Tribo-Corrosion*, 10(3), 44. https://doi.org/10.1007/s40735-024-00849-x.

[31] Gao, L., Din, Z., Kim, K., and Senouci, A. (2025). Modeling the deterioration of pavement skid resistance and surface texture after preventive maintenance. *arXiv preprint*, arXiv:2507.01842. https://doi.org/10.48550/arXiv.2507.01842.

[32] Maryland Department of Transportation State Highway Administration (MDOT-SHA). (2024). *Standard specifications for construction and materials*. https://rb.gy/j0rby8.

[33] Goulias, D., and Aljarrah, O. (2024). *Evaluating the correlation between slip resistance and skid resistance of pavement markings at crosswalks (No. MD-23-SHA/UM/6-23)*. Maryland Department of Transportation. https://rosap.ntl.bts.gov/view/dot/83470.

[34] New York State Department of Transportation (NYSDOT). (2023). *Highway safety improvement program procedures and techniques (Red Book)*. https://www.dot.ny.gov/divisions/operating/osss/highway-repository/RedBook.pdf.

[35] Sudoł, E., Szewczak, E., and Małek, M. (2021). Comparative analysis of slip resistance test methods for granite floors. *Materials*, 14(5), 1108. https://doi.org/10.3390/ma14051108.

[36] Marletta, A. J. (2023). *Walkway surface evaluation: An analysis of floor surface microroughness and its impact on available friction, human slip potential and walkway surface slipperiness perception* (Order No. 30418973). ProQuest Dissertations & Theses Global. https://www.proquest.com/dissertations-theses/walkway-surface-evaluation-analysis-floor/docview/2804866323/se-2.

[37] Beschorner, K. E., Chanda, A., Moyer, B. E., Reasinger, A., Griffin, S. C., and Johnston, I. M. (2023). Validating the ability of a portable shoe-floor friction testing device, NextSTEPS, to predict human slips. *Applied Ergonomics*, 106, 103854. https://doi.org/10.1016/j.apergo.2022.103854.

[38] Qiao, F., Kazimi, S. A., Ekezie, E., and Du, J. (2023). *Synthesis of best application and verification practices for long-life pavement markings (No. FHWA/TX-22/0-7135-1)*. Texas Southern University. https://rosap.ntl.bts.gov/view/dot/67270.

[39] Zhao, L., Ding, H., Sun, J., Wu, G., Xing, H., Wang, W., and Song, J. (2023). Prediction of service life of thermoplastic road markings on expressways. *Sustainability*, 15(21), 15237. https://doi.org/10.3390/su152115237.

[40] Pike, A. M., and Speidel, D. (2022). *Airfield pavement markings: Effective techniques for removal and temporary applications*. Transportation Research Board. https://dx.doi.org/10.17226/26797.

[41] City of Springfield. (2021). *Preformed thermoplastic (High Banks & Thurston, P21152)*. https://www.springfield-or.gov/wp-content/uploads/2021/03/P21152-High-Banks-Thurston-Q-A.pdf.

[42] North Dakota Department of Transportation (NDDOT). (2022). *Standard specifications for road and bridge construction*. https://www.dot.nd.gov/sites/www/files/documents/Standard%20Specifications/2022%20Standard%20Specifications%20for%20Road%20and%20Bridge%20Construction.pdf.

[43] Jo, H., Son, H., Rencheck, M., Gohl, J., Madigan, D., Grennan, H., ... and Erk, K. A. (2021). *Mechanical properties of durable pavement marking materials and adhesion on asphalt surfaces*. https://docs.lib.purdue.edu/jtrp/1773/.

[44] Sheng, W. (2025). *Functions and durability of manufactured concrete pavement textures* (Doctoral dissertation, The Hong Kong Polytechnic University). Pao Yue-kong Library Institutional Repository. https://theses.lib.polyu.edu.hk/handle/200/13638.

[45] AASHTO. (2022). *Guide for pavement friction* (2nd ed.). American Association of State Highway and Transportation Officials. https://store.transportation.org/Item/CollectionDetail?ID=239.

[46] Maia, R. S. (2020). *Contributions to the tire-pavement friction characterization from the traffic safety perspective* (Master's thesis). Universidade Federal do Ceará. http://repositorio.ufc.br/handle/riufc/55714.

[47] Cui, X., Chu, L., and Fwa, T. F. (2024). Determination of dynamic coefficient of friction of pedestrian pavement using British Pendulum Test. In *International Conference on Road and Airfield Pavement Technology 2023* (pp. 464–473). https://doi.org/10.1061/9780784485255.038.

[48] BSI. (2011). *BS EN 13036-4: Road and airfield surface characteristics — Test methods for measurement of slip/skid resistance of a surface: The Pendulum Test*. https://knowledge.bsigroup.com/products/road-and-airfield-surface-characteristics-test-methods-method-for-meas

[49] ISO. (2017). *ISO 4662:2017(en), Rubber, vulcanized or thermoplastic — Determination of rebound resilience*. https://www.iso.org/standard/68111.html.

[50] ISO. (2018). *ISO 48-1:2018(en), Rubber, vulcanized or thermoplastic — Determination of hardness — Part 1: Introduction and guidance*. https://www.iso.org/standard/74966.html.

[51] Chu, Q., Tian, X., Bian, H., and Wang, C. (2025). Optimization of mechanical and dynamic properties of tread rubber using fumed silica and hydration processing. *Polymers*, 17(6), 714. https://doi.org/10.3390/polym17060714.

[52] Dimulescu, S. C., Nioaţă, A., and Wetternek, M. (2024). Analysis of the determination of the hardness of composite materials with rubber matrices with additions of Fa and PVC. *Fiability & Durability / Fiabilitate Si Durabilitate*, 33(1), 286–295. https://research.ebsco.com/c/jbv2fl/search/details/rynye2rkkz?db=asn.

[53] Martin, A. (2006). *Factors influencing pedestrian safety: a literature review* (No. PPR241). Wokingham, UK: TRL. https://content.tfl.gov.uk/factors-influencing-pedestrian-safety-literature-review.pdf.

[54] Plati, C., and Georgouli, K. (2014). Field investigation of factors affecting skid resistance variations in asphalt pavements. *The Baltic Journal of Road and Bridge Engineering*, 9(2), 108–114. https://doi.org/10.3846/bjrbe.2014.14.

[55] Fwa, T. F. (2017). Skid resistance determination for pavement management and wet-weather road safety. *International Journal of Transportation Science and Technology*, 6(3), 217–227. https://doi.org/10.1016/j.ijtst.2017.08.001.

[56] Lu, J., Pan, B., Liu, Q., Sun, M., Liu, P., and Oeser, M. (2022). A novel noncontact method for the pavement skid resistance evaluation based on surface texture. *Tribology International*, 165, 107311. https://doi.org/10.1016/j.triboint.2021.107311.

[57] Musey, K., and Park, S. (2016). Pavement skid number and horizontal curve safety. *Procedia Engineering*, 145, 828–835. https://doi.org/10.1016/j.proeng.2016.04.108.

[58] Saito, K., Horiguchi, T., Kasahara, A., Abe, H., and Henry, J. J. (1996). Development of portable tester for measuring skid resistance and its speed dependency on pavement

surfaces. *Transportation Research Record*, 1536(1), 45–51. https://doi.org/10.1177/03611981961536001.

[59] Pomoni, M., and Plati, C. (2022). Skid resistance performance of asphalt mixtures containing recycled pavement materials under simulated weather conditions. *Recycling*, 7(4), 47. https://doi.org/10.3390/recycling7040047.

[60] Rodin III, H., Nassiri, S., AlShareedah, O., Yekkalar, M., and Haselbach, L. (2021). Evaluation of skid resistance of pervious concrete slabs under various winter conditions for driver and pedestrian users. *Road Materials and Pavement Design*, 22(6), 1350–1368. https://doi.org/10.1080/14680629.2019.1688175.

[61] Kulakowski, B. T., Henry, J. J., and Lin, C. (1990). "A closed-loop calibration procedure for a British Pendulum Tester." In *Surface Characteristics of Roadways: International Research and Technologies*, ASTM International, 103–112. https://store.astm.org/stp23356s.html

[62] Strautins, C. (2020). "Pendulum calibration, metrological traceability and reference material." *International Slips, Trips and Falls Conference*. https://www.researchgate.net/publication/341883428

[63] Mataei, B., Zakeri, H., Zahedi, M., and Nejad, F. M. (2016). "Pavement friction and skid resistance measurement methods: A literature review." *Open Journal of Civil Engineering*, 6(4), 537–556. https://www.scirp.org/html/4-1880608_70357.htm

[64] Wallman, C. G., and Åström, H. (2001). "Friction measurement methods and the correlation between road friction and traffic safety: A literature review." Swedish National Road and Transport Research Institute (VTI). https://www.diva-portal.org/smash/record.jsf?pid=diva2:673366

[65] Kummer, H. W. (1966). "Unified theory of rubber and tire friction." Engineering Research Bulletin B-94, Pennsylvania State University. https://trid.trb.org/View/1150653

[66] Sandberg, U. (1998). "Influence of road surface texture on traffic characteristics related to environment, economy and safety." VTI Notat 53A-1997, Statens Väg- och Transportforskningsinstitut. https://www.diva-portal.org/smash/record.jsf?pid=diva2:669806

[67] Abaza, O. A., Chowdhury, T. D., and Arafat, M. (2017). "Comparative analysis of skid resistance for different roadway surface treatments." *American Journal of Engineering and Applied Sciences*, 10(4), 890–899. https://d1wqtxts1xzle7.cloudfront.net/66339931/ajeassp.2017.890-libre.pdf

[68] Guo, F., Pei, J., Zhang, J., Li, R., Zhou, B., and Chen, Z. (2021). "Study on the skid resistance of asphalt pavement: A state-of-the-art review and future prospective." *Construction and Building Materials*, 303, 124411. https://doi.org/10.1016/j.conbuildmat.2021.124411

[69] Jagadeesh, A., and Ong, G. P. (2021). "Skid resistance evaluation of pervious pavement mixtures using XRCT-based modelling." *Asian Transport Studies*, 7, 100041. https://doi.org/10.1016/j.eastsj.2021.100041

[70] HSE UK. (2012). "Assessing the slip resistance of flooring: A technical information sheet (British Standard 7976)." Health and Safety Executive. https://www.hse.gov.uk/pubns/geis2.htm

[71] National Floor Safety Institute (NFSI). (2012). *B101.3 Test Method for Measuring Wet DCOF of Common Hard-Surface Floor Materials (ANSI/NFSI B101.3-2012)*. Southlake, TX. https://webstore.ansi.org/preview-pages/NFSI/preview_ANSI+NFSI+B101.3-2012.pdf

[72] AS/NZS 4586. (2013). *Slip resistance classification of new pedestrian surface materials*. Australian Standards. https://drive.google.com/file/d/1ddxu9Gcv70qV0zZmFXfhgHGaZV6kOoh2/view?pli=1

[73] British Standards Institution (BSI). (2008). *BS 8204-6: Screeds, bases and in situ floorings – Part 6: Synthetic resin floorings. Code of practice*. European Committee for Standardization, Brussels. https://knowledge.bsigroup.com/products/screeds-bases-and-in-situ-floorings-synthetic-resin-floorings-code-of-

[74] Eriskin, E., Karahancer, S., Terzi, S., and Saltan, M. (2017). "Examination of the effect of superhydrophobic coated pavement under wet conditions." *Procedia Engineering*, 187, 532–537. https://doi.org/10.1016/j.proeng.2017.04.411

[75] Houle, K. M. (2008). *Winter performance assessment of permeable pavements: A comparative study of porous asphalt, pervious concrete, and conventional asphalt in a northern climate*. University of New Hampshire. https://www.proquest.com/dissertations-theses/winter-performance-assessment-permeable-pavements/docview/304525272/se-2?accountid=14696

[76] Sajid, H. U., Naik, D. L., and Kiran, R. (2021). "Improving the ice-melting capacity of traditional deicers." *Construction and Building Materials*, 271, 121527. https://doi.org/10.1016/j.conbuildmat.2020.121527

[77] Andriejauskas, T., Vorobjovas, V., and Mielonas, V. (2014). "Evaluation of skid resistance characteristics and measurement methods." In *Environmental Engineering. Proceedings

of the International Conference on Environmental Engineering. ICEE* (Vol. 9, p. 1). Vilnius Gediminas Technical University, Department of Construction Economics & Property. http://enviro2014.vgtu.lt/Articles/4/141_Andriejauskas.pdf

[78] Chang, W. R. (1999). "The effect of surface roughness on the measurement of slip resistance." *International Journal of Industrial Ergonomics*, **24**(3), 299–313. https://doi.org/10.1016/S0169-8141(98)00038-9.

[79] Babić, D., Fiolić, M., Babić, D., and Gates, T. (2020). "Road markings and their impact on driver behaviour and road safety: A systematic review of current findings." *Journal of Advanced Transportation*, 2020(1), 7843743. https://doi.org/10.1155/2020/7843743

[80] Garilli, E., Autelitano, F., Freddi, F., and Giuliani, F. (2022). "Urban pedestrian stone pavements: Measuring functional and safety requirements." *International Journal of Pavement Engineering*, 23(13), 4748–4759. https://doi.org/10.1080/10298436.2021.1975195

[81] Neaylon, K., and Choi, Y. (2011, May). "Austroads developments in skid resistance." In *International Surface Friction Conference, 3rd, 2011*. http://saferroadsconference.com/conference-papers-2011/

[82] Çoşkun, G., Sarıışık, G., and Sarıışık, A. (2016). "Classification of parameters affecting slip safety of limestones." *Cogent Engineering*, 3(1), 1217821. https://doi.org/10.1080/23311916.2016.1217821

[83] Cairney, P. (1997). "Skid resistance and crashes: a review of the literature." (No. ARR 311). https://trid.trb.org/View/539297.

[84] AASHTO. (2008). *Guide for pavement friction*. American Association of State Highway and Transportation Officials, Washington, DC. http://rhvpi.ca/od/Documents/HAM/HAM0028606_0001.pdf.

[85] Choubane, B., Holzschuher, C. R., and Gokhale, S. (2004). "Precision of locked-wheel testers for measurement of roadway surface friction characteristics." *Transportation Research Record*, **1869**(1), 145–151. https://doi.org/10.3141/1869-17.

[86] Zimmer, R. A., Choubane, B., and Holzschuher, C. R. (2003). "Friction testing method for open-grated steel bridge decks." *Transportation Research Record*, **1860**(1), 137–143. https://doi.org/10.3141/1860-15.

[87] Smith, R. H. (2008). *Analyzing friction in the design of rubber products and their paired surfaces*. CRC Press. https://doi.org/10.1201/9780849381379.

[88] Smith, R. H. (2011). "Measuring individual rubber friction forces." *Rubber World*, **243**(4), 20–23. https://scholar.google.com/scholar?hl=en&as_sdt=0%2C21&q=Smith%2C+R.+H.+%282011%29.+Measuring+rubber+friction+forces+individually.+Rubber+World%2C+243%284%29%2C+20%E2%80%9323.&btnG=.

[89] Kogbara, R. B., Masad, E. A., Kassem, E., Scarpas, A. T., and Anupam, K. (2016). "A state-of-the-art review of parameters influencing measurement and modeling of skid resistance of asphalt pavements." *Construction and Building Materials*, **114**, 602–617. https://doi.org/10.1016/j.conbuildmat.2016.04.002.

[90] Giles, C. G., Sabey, B. E., and Cardew, K. H. F. (1965). "Development and performance of the portable skid resistance tester." *Rubber Chemistry and Technology*, **38**(4), 840–862. https://store.astm.org/stp44406s.html.

[91] Hsu, H. P. (1995). *Theory and Problems of Signals and Systems*. https://electrobian.wordpress.com/wp-content/uploads/2016/07/signals_and_systems__schaum_.pdf

[92] Oppenheim, A. V., Willsky, A. S., and Nawab, S. H. (1997). *Signals & Systems*. Pearson Educación. https://books.google.com/books?hl=en&lr=&id=g2750K3PxRYC&oi=fnd&pg=PR17&dq=Oppenheim,+A.+V.,+Willsky,+A.+S.,+%26+Nawab,+S.+H.+(1998).+Signals+%26+Systems+(2nd+ed.).+Pearson+Educaci%C3%B3n.+&ots=f2NEghoo5K&sig=e5zrpxJFyguYkF0wRWikbSh7DYQ#v=onepage&q&f=false

[93] Kouchaki, S., Roshani, H., Prozzi, J. A., and Hernandez, J. B. (2017). "Evaluation of aggregates surface micro-texture using spectral analysis." *Construction and Building Materials*, **156**, 944–955. https://doi.org/10.1016/j.conbuildmat.2017.08.174

[94] Karrenberg, U. (2013). *Signals, Processes, and Systems: An Interactive Multimedia Introduction to Signal Processing* (3rd ed.). Springer Berlin, Heidelberg. https://doi.org/10.1007/978-3-642-38053-2

[95] Putman, J. A. (2007). "Signal processing techniques." Report No., EEG Info, Woodland Hills, CA. https://www.eeginfo.com/research/researchpapers/Signal_Processing.pdf

[96] Moreno-Ríos, M., Gallardo-Hernández, E. A., Vite-Torres, M., and Peña-Bautista, A. (2016). "Field and laboratory assessments of the friction coefficient at a railhead." *Proceedings of the Institution of Mechanical Engineers, Part F: Journal of Rail and Rapid Transit*, **230**(1), 313–320. https://doi.org/10.1177/0954409714536383

[97] Tajnin, M. R. (2023). *Developing a Pavement Marking Management Plan for Wyoming*. University of Wyoming. https://www.proquest.com/dissertations-theses/developing-pavement-marking-management-plan/docview/2854305762/se-2

[98] Xu, L., Chen, Z., Li, X., and Xiao, F. (2021). "Performance, environmental impact and cost analysis of marking materials in pavement engineering, the-state-of-art." *Journal of Cleaner Production*, 294, 126302. https://doi.org/10.1016/j.jclepro.2021.126302

[99] Bao, J., Hu, X., Peng, C., Duan, J., Lin, Y., Tao, C., ... Li, S. (2024). *Advancing INDOT's Friction Test Program for Seamless Coverage of System: Pavement Markings, Typical Aggregates, Color Surface Treatment, and Horizontal Curves*. Joint Transportation Research Program, Purdue University. https://doi.org/10.5703/1288284317734

[100] Sightline. (n.d.). "Glass bead specifications." https://www.sightline.us/estimator/beadspecs.pdf

[101] Bertocci, U., Huet, F., Nogueira, R., and Rousseau, P. (2001, March). "Drift removal procedures for PSD calculation." In *CORROSION 2001* (pp. 1–16). Association for Materials Protection and Performance. https://doi.org/10.5006/C2001-01291

[102] Chen, S., Liu, X., Luo, H., Yu, J., Chen, F., Zhang, Y., ... and Huang, X. (2022). "A state-of-the-art review of asphalt pavement surface texture and its measurement techniques." *Journal of Road Engineering*, 2(2), 156–180. https://doi.org/10.1016/j.jreng.2022.05.003

[103] Masad, E., and Fletcher, T. (2005). "Aggregate imaging system (AIMS): Basics and applications (No. FHAWA/TX-05/5-1707-01-1)." College Station, TX: Texas Transportation Institute, Texas A & M University System. https://static.tti.tamu.edu/tti.tamu.edu/documents/5-1707-01-1.pdf.

[104] Masad, E., Gates, L., Pyle, R., and Bushee, D. (2011). "Aggregate imaging measurement system 2 (AIMS2) (No. FHWA-HIF-11-030)." Federal Highway Administration (US). https://rosap.ntl.bts.gov/view/dot/54171.

[105] Rezaei, A., Hoyt, D., and Martin, A. E. (2011). "Simple laboratory method for measuring pavement macrotexture: pavement cores and aggregate image measurement system." *Transportation Research Record*, 2227(1), 146–152. https://doi.org/10.3141/2227-16.

[106] Mallat, S. G. (1989). "A theory for multiresolution signal decomposition: the wavelet representation." *IEEE Transactions on Pattern Analysis and Machine Intelligence*, 11(7), 674–693. https://doi.org/10.1109/34.192463.

[107] Mahmoud, E., and Ortiz, E. (2014). "Implementation of AIMS in measuring aggregate resistance to polishing, abrasion, and breakage." FHWA-ICT-14-014. http://hdl.handle.net/2142/49941.

[108] Aldagari, S. (2017). "Development of prediction models for skid resistance of asphalt pavements." Ph.D. Dissertation, University of Idaho. https://www.proquest.com/dissertations-theses/development-prediction-models-skid-resistance/docview/1873066849/se-2.

[109] Ran, M., Xiao, S., Li, M., Jiang, R., Zhou, X., and Tan, Y. (2024). "Exploring the relationship between pavement mean texture depth and mean profile depth: From theoretical derivation to field results." *Surface Topography: Metrology and Properties*, 12(2), 025028. https://doi.org/10.1088/2051-672X/ad54dc.

[110] Anderson, D. A., and Henry, J. J. (1980). "Wet-pavement friction of pavement-marking materials." *Transportation Research Record*, 777, 58–62. https://www.safetylit.org/citations/index.php?fuseaction=citations.viewdetails&citationIds[]=citjournalarticle_484447_38.

[111] Henry, J. J., Anderson, D. A., and Hayhoe, G. F. (1981). "Skid Resistance of Pavement Marking Materials Volume 1 (No. FHWA-RD-80-199)." U.S. Department of Transportation, Federal Highway Administration. https://rosap.ntl.bts.gov/view/dot/67630.

[112] Federal Highway Administration. (n.d.). "Chapter 5: Wet pavement marking retroreflectivity." In *Synthesis of pavement marking research*. U.S. Department of Transportation. https://highways.dot.gov/safety/other/visibility/synthesis-pavement-marking-research/chapter-5-wet-pavement-marking.

[113] Park, E. S., Carlson, P. J., and Pike, A. (2019). "Safety effects of wet-weather pavement markings." *Accident Analysis & Prevention*, 133, 105271. https://doi.org/10.1016/j.aap.2019.105271.

[114] Kouchaki, S. (2019). "Improving Pavement Surface Texture Using Laser Scanning and Numerical Analysis." Ph.D. Dissertation, The University of Texas at Austin. https://www.proquest.com/docview/2478955476?pq-origsite=gscholar&fromopenview=true&sourcetype=Dissertations%20&%20Theses.

[115] Kováč, M., and Čelko, J. (2004). "Evaluation of pavement friction according to European standards." *Komunikácie – Vedecké Listy Žilinskej Univerzity v Žiline*, 6(3), 28–30. https://www.ceeol.com/search/article-detail?id=1126441.

[116] Masad, E., Luce, A., & Mahmoud, E. (2006). *Implementation of AIMS in measuring aggregate resistance to polishing, abrasion and breakage* [Report]. Texas Transportation Institute. https://static.tti.tamu.edu/tti.tamu.edu/documents/5-1707-03-1.pdf

[117] Masad, E., Al-Rousan, T., Button, J., Little, D., & Tutumluer, E. (2007). *Test methods for characterizing aggregate shape, texture, and angularity* (NCHRP Report 555). Transportation Research Board. https://www.trb.org/publications/nchrp/nchrp_rpt_555.pdf

[118] Federal Highway Administration (FHWA). (2023, December 1). "Manual on uniform traffic control devices for streets and highways" (11th ed.). https://rosap.ntl.bts.gov/view/dot/73253

[119] Migletz, J., and Graham, J. L. (2002). "Long-term pavement marking practices: A synthesis of highway practice" (Vol. 306). Transportation Research Board. https://books.google.com/books?hl=en&lr=&id=yDRw0p7fG7wC&oi=fnd&pg=PP1&ots=1Ww3kjWXTu&sig=o6fZEKN76l4KeqXHve3oF84CaJo#v=onepage&q&f=false

[120] Zwahlen, H. T., and Schnell, T. (1999). "Visibility of road markings as a function of age, retroreflectivity under low-beam and high-beam illumination at night." *Transportation Research Record*, 1692(1), 152–163. https://doi.org/10.3141/1692-16

[121] Montella, A., Mauriello, F., and Eng, P. (2010, June). "Pedestrian crosswalks safety inspections: safety assessment procedure." In *4th International Symposium on Highway Geometric Design, TRB* (pp. 1–17). https://trid.trb.org/View/1098926

[122] Piyatrapoomi, N., Weligamage, J., Kumar, A., and Bunker, J. (2008). "Identifying relationship between skid resistance and road crashes using probability-based approach." In *Proceedings of the 2nd International Safer Roads Conference* (pp. 1–12). Safe Roads Organisation. https://eprints.qut.edu.au/41248/

[123] Ivan, J. N., Ravishanker, N., Jackson, E., Aronov, B., and Guo, S. (2012). "A statistical analysis of the effect of wet-pavement friction on highway traffic safety." *Journal of Transportation Safety & Security*, 4(2), 116–136. https://doi.org/10.1080/19439962.2011.620218

[124] Pitaksringkarn, J., Tanwanichkul, L., and Yamthale, K. (2018). "A correlation between pavement skid resistance and wet-pavement related accidents in Thailand." In *MATEC Web*

of Conferences (Vol. 192, p. 02049). EDP Sciences. https://doi.org/10.1051/matecconf/201819202049

[125] Debaillon, C., Carlson, P. J., He, Y., Schnell, T., and Aktan, F. (2007). "Updates to research on recommended minimum levels for pavement marking retroreflectivity to meet driver night visibility needs" (No. FHWA-HRT-07-059). Turner-Fairbank Highway Research Center. https://rosap.ntl.bts.gov/view/dot/841

[126] Pasetto, M., and Barbati, S. D. (2011, May). "Definition and validation of a new methodical approach for friction evaluations of dropped-on products for road markings." In *International Surface Friction Conference, 3rd, 2011*. https://trid.trb.org/View/1106450

[127] Henry, J. J. (2000). "Evaluation of pavement friction characteristics" (Vol. 291). Transportation Research Board. https://books.google.com/books?hl=en&lr=&id=qBmbZHesnHIC&oi=fnd&pg=PA1&ots=vl2belIgTF&sig=cKHmnLBy213saIa_icCYGLk8zXM#v=onepage&q&f=false

[128] ASTM. (2022). "ASTM E303-22: Standard test method for measuring surface frictional properties using the British pendulum tester." https://doi.org/10.1520/E0303-22

[129] Rosta, S., and Gáspár, L. (2023). "Skid resistance of asphalt pavements." *Eng*, 4(2), 1597–1615. https://doi.org/10.3390/eng4020091

[130] Andriejauskas, T., and Wang, Z. (2022). "Investigation of the impacts of climatic conditions on skid resistance variation" (No. PPR2001). https://trid.trb.org/View/2051216

[131] Fwa, T. F. (2021). "Determination and prediction of pavement skid resistance–connecting research and practice." *Journal of Road Engineering*, 1, 43–62. https://doi.org/10.1016/j.jreng.2021.12.001

[132] Susanna, A., Crispino, M., Giustozzi, F., and Toraldo, E. (2017). "Deterioration trends of asphalt pavement friction and roughness from medium-term surveys on major Italian roads." *International Journal of Pavement Research and Technology*, 10(5), 421–433. https://doi.org/10.1016/j.ijprt.2017.07.002

[133] Giummarra, G. J., Martin, T., Hoque, Z., and Roper, R. (2007). "Establishing deterioration models for local roads in Australia." *Transportation Research Record*, 1989(1), 270–276. https://doi.org/10.3141/1989-73

[134] Xiao, F., Shi, B., Gao, J., Chen, H., and Yang, D. (2025). "Enhanced probabilistic prediction of pavement deterioration using Bayesian neural networks and cuckoo search optimization." *Scientific Reports*, 15(1), 8665. https://doi.org/10.1038/s41598-025-92469-9

[135] Elkhazindar, A., Hafez, M., and Ksaibati, K. (2022). "Incorporating pavement friction management into pavement asset management systems: State department of transportation experience." *CivilEng*, 3(2), 541–561. https://doi.org/10.3390/civileng3020032

[136] Kang, J. (2022). "Pavement performance prediction using machine learning and instrumentation in smart pavement" (Master's thesis, University of Waterloo). http://hdl.handle.net/10012/18752

[137] Dan, H. C., Lu, B., and Li, M. (2024). "Evaluation of asphalt pavement texture using multiview stereo reconstruction based on deep learning." *Construction and Building Materials*, 412, 134837. https://doi.org/10.1016/j.conbuildmat.2023.134837

[138] Gopalakrishnan, K. (2018). "Deep learning in data-driven pavement image analysis and automated distress detection: A review." *Data*, 3(3), 28. https://doi.org/10.3390/data3030028

[139] Marcelino, P., de Lurdes Antunes, M., Fortunato, E., and Gomes, M. C. (2021). "Machine learning approach for pavement performance prediction." *International Journal of Pavement Engineering*, 22(3), 341–354. https://doi.org/10.1080/10298436.2019.1609673

[140] Mikels, N., Kassem, E., Muftah, A., Sufian, A. A., and Pacific Northwest Transportation Consortium. (2023). "The Use of Artificial Intelligence in Pavement Engineering" (No. 2021-M-UAF-2). Pacific Northwest Transportation Consortium (PacTrans)(UTC). https://rosap.ntl.bts.gov/view/dot/73100

[141] Lu, B., Dan, H. C., Zhang, Y., and Huang, Z. (2025). "Journey into Automation: Image-Derived Pavement Texture Extraction and Evaluation." *arXiv preprint* arXiv:2501.02414. https://doi.org/10.48550/arXiv.2501.02414

[142] Fahad, M., and Bektas, N. (2025). "Data-Driven Pavement Performance: Machine Learning-Based Predictive Models." *Applied Sciences*, 15(7), 3889. https://doi.org/10.3390/app15073889

[143] Ahmed, N. S. (2024). "Machine Learning Models for Pavement Structural Condition Prediction: A Comparative Study of Random Forest (RF) and eXtreme Gradient Boosting (XGBoost)." *Open Journal of Civil Engineering*, 14(4), 570–586. https://doi.org/10.4236/ojce.2024.144031

[144] Hu, Y., Sun, Z., Han, Y., Li, W., and Pei, L. (2022). "Evaluate pavement skid resistance performance based on Bayesian-LightGBM using 3D surface macrotexture data." *Materials*, 15(15), 5275. https://doi.org/10.3390/ma15155275

[145] Hu, Y., Sun, Z., Pei, L., Han, Y., and Li, W. (2024). "Evaluate asphalt pavement frictional characteristics based on IGWO-NGBoost using 3D macro-texture data." *Expert Systems with Applications*, 242, 122786. https://doi.org/10.1016/j.eswa.2023.122786

[146] Zhan, Y., Li, J. Q., Liu, C., Wang, K. C., Pittenger, D. M., and Musharraf, Z. (2021). "Effect of aggregate properties on asphalt pavement friction based on random forest analysis." *Construction and Building Materials*, 292, 123467. https://doi.org/10.1016/j.conbuildmat.2021.123467

[147] Khasawneh, M. A., Alsheyab, M. A., and Al Akhrass, H. I. (2023). "Modeling Asphalt Pavement Frictional Properties using Different Machine Learning Algorithms." https://doi.org/10.29117/cic.2023.0075

[148] Wang, J., Comert, G., Begashaw, N., Huynh, N., Kouyate, A., Mullen, R., *et al.* (2024). "Comparative Analysis of Three Modeling Approaches for Predicting Pavement Conditions." *Transportation Research Record*, 2678(10), 547–560. https://doi.org/10.1177/03611981241234924

[149] Yang, E., Yang, Q., Li, J., Zhang, H., Di, H., and Qiu, Y. (2022). "Establishment of icing prediction model of asphalt pavement based on support vector regression algorithm and Bayesian optimization." *Construction and Building Materials*, 351, 128955. https://doi.org/10.1016/j.conbuildmat.2022.128955

[150] Koné, A., Es-Sabar, A., and Do, M. T. (2023). "Application of Machine Learning Models to the Analysis of Skid Resistance Data." *Lubricants*, 11(8), 328. https://doi.org/10.3390/lubricants11080328

[151] Idris, I. I., Mousa, M., and Hassan, M. M. (2024). "Machine Learning–Based Framework for Prediction of Retroreflectivity Degradation of Pavement Markings across the US." *Journal of Transportation Engineering, Part B: Pavements*, 150(2), 04024011. https://doi.org/10.1061/JPEODX.PVENG-1382

[152] Jiang, X., Abdel-Aty, M., Hu, J., and Lee, J. (2016). "Investigating macro-level hotzone identification and variable importance using big data: A random forest models approach." *Neurocomputing*, 181, 53–63. https://doi.org/10.1016/j.neucom.2015.08.097

[153] Damirchilo, F., Hosseini, A., Mellat Parast, M., and Fini, E. H. (2021). "Machine learning approach to predict international roughness index using long-term pavement perfor-

mance data." *Journal of Transportation Engineering, Part B: Pavements*, 147(4), 04021058. https://doi.org/10.1061/JPEODX.0000312

[154] Ahmed, N. S., Huynh, N., Gassman, S., Mullen, R., Pierce, C., and Chen, Y. (2022). "Predicting pavement structural condition using machine learning methods." *Sustainability*, 14(14), 8627. https://doi.org/10.3390/su14148627

[155] Biau, G., and Scornet, E. (2016). "A random forest guided tour." *Test*, 25(2), 197–227. https://doi.org/10.1007/s11749-016-0481-7

[156] Faizollahzadeh Ardabili, S., Najafi, B., Shamshirband, S., Minaei Bidgoli, B., Deo, R. C., and Chau, K. W. (2018). "Computational intelligence approach for modeling hydrogen production: A review." *Engineering Applications of Computational Fluid Mechanics*, 12(1), 438–458. https://doi.org/10.1080/19942060.2018.1452296

[157] Karballaeezadeh, N., Mohammadzadeh S, D., Shamshirband, S., Hajikhodaverdikhan, P., Mosavi, A., and Chau, K. W. (2019). "Prediction of remaining service life of pavement using an optimized support vector machine (case study of Semnan–Firuzkuh road)." *Engineering Applications of Computational Fluid Mechanics*, 13(1), 188–198. https://doi.org/10.1080/19942060.2018.1563829

[158] Smola, A. J., and Schölkopf, B. (2004). "A tutorial on support vector regression." *Statistics and Computing*, 14, 199–222. https://doi.org/10.1023/B:STCO.0000035301.49549.88

[159] Carpenter, J., Clifford, P., and Fearnhead, P. (1999). "Improved particle filter for nonlinear problems." *IEE Proceedings-Radar, Sonar and Navigation*, 146(1), 2–7. https://doi.org/10.1049/ip-rsn:19990255

[160] Momeni, E., Dowlatshahi, M. B., Omidinasab, F., Maizir, H., and Armaghani, D. J. (2020). "Gaussian process regression technique to estimate the pile bearing capacity." *Arabian Journal for Science and Engineering*, 45, 8255–8267. https://doi.org/10.1007/s13369-020-04683-4

[161] Heyns, T., de Villiers, J. P., and Heyns, P. S. (2012). "Consistent haul road condition monitoring by means of vehicle response normalisation with Gaussian processes." *Engineering Applications of Artificial Intelligence*, 25(8), 1752–1760. https://doi.org/10.1016/j.engappai.2012.01.009

[162] Gardner, M. W., and Dorling, S. R. (1998). "Artificial neural networks (the multilayer perceptron)—a review of applications in the atmospheric sciences." *Atmospheric Environment*, 32(14–15), 2627–2636. https://doi.org/10.1016/S1352-2310(97)00447-0

[163] Lau, M. M., and Lim, K. H. (2018, December). "Review of adaptive activation function in deep neural network." In *2018 IEEE-EMBS Conference on Biomedical Engineering and Sciences (IECBES)* (pp. 686–690). IEEE. http://doi.org/10.1109/IECBES.2018.8626714

[164] Kingma, D. P., and Ba, J. (2014). "Adam: A method for stochastic optimization." *arXiv preprint* arXiv:1412.6980. https://doi.org/10.48550/arXiv.1412.6980

[165] Parker, F., & Song, J. (2002). *Evaluation of flexible pavement performance using LTPP data* (No. 930-419). Alabama Department of Transportation. https://rosap.ntl.bts.gov/view/dot/5779

[166] Williams, R. C., & Shaidur, R. (2013). *Mechanistic-empirical pavement design guide calibration for pavement rehabilitation* (No. SPR 718). Oregon Department of Transportation, Research Section. https://rosap.ntl.bts.gov/view/dot/25790

[167] Bayomy, F., Muftah, A., Kassem, E., Williams, C., & Hasnat, M. (2019). *Calibration of the AASHTOWare Pavement ME Design Software for PCC Pavements in Idaho* (No. FHWA-ID-19-268). Idaho Transportation Department. https://rosap.ntl.bts.gov/view/dot/55848

[168] Amin, M. S. R. (2014). The pavement performance modeling: Deterministic vs. stochastic approaches. In *Numerical methods for reliability and safety assessment: Multiscale and multiphysics systems* (pp. 179–196). Cham: Springer International Publishing. https://doi.org/10.1007/978-3-319-07167-1_5

[169] Abd-elfattah, S. S., Abu-Elmaaty, A. I., & Hashim, I. H. (2022). Reliability analysis of flexible pavement using crude Monte Carlo simulation. *Engineering Research Journal*, 45(3), 447–456. https://doi.org/10.21608/erjm.2022.117611.1143

[170] Radwan, M., Abo-hashema, M., Hashem, M., & Faheem, H. (2020). Modeling pavement performance based on LTPP database for flexible pavements. *Teknik Dergi*, 31(4), 10127–10146. https://doi.org/10.18400/tekderg.476606

[171] Raffaniello, A., Bauer, M., Safiuddin, M., & El-Hakim, M. (2022). Traffic and climate impacts on rutting and thermal cracking in flexible and composite pavements. *Infrastructures*, 7(8), 100. https://doi.org/10.3390/infrastructures7080100

[172] Philip, B., & Jassmi, H. A. (2022). A Bayesian approach towards modelling the interrelationships of pavement deterioration factors. *Buildings*, 12(7), 1039. https://doi.org/10.3390/buildings12071039

[173] Federal Highway Administration (FHWA). (2002). *Long-Term Pavement Performance Program*. https://www.fhwa.dot.gov/research/tfhrc/programs/infrastructure/pavements/ltpp/

[174] Federal Highway Administration (FHWA). (2017). *Long-Term Pavement Performance*. https://infopave.fhwa.dot.gov/

[175] Abo-Hashema, M. A., & Sharaf, E. A. (2009). Development of maintenance decision model for flexible pavements. *International Journal of Pavement Engineering*, 10(3), 173–187. https://doi.org/10.1080/10298430802169457

[176] Ahmed, J. (2023). Time-temperature superposition principles: applicability in food and biopolymer rheology. In *Advances in food rheology and its applications* (pp. 221–260). Woodhead Publishing. https://doi.org/10.1016/B978-0-12-823983-4.00024-8

[177] Nguyen, M. L., Sauzéat, C., Di Benedetto, H., & Tapsoba, N. (2013). Validation of the time–temperature superposition principle for crack propagation in bituminous mixtures. *Materials and Structures*, 46, 1075–1087. https://doi.org/10.1617/s11527-012-9954-7

[178] Saremi, S., & Goulias, D. (2023). Non-destructive testing in concrete maturity modeling and master curve development. *Applied Sciences*, 13(13), 7770. https://doi.org/10.3390/app13137770

[179] Sakai, T., Hirai, Y., & Somiya, S. (2018). Estimating the creep behavior of glass-fiber-reinforced polyamide considering the effects of crystallinity and fiber volume fraction. *Mechanics of Advanced Materials and Modern Processes*, 4, 1–9. https://doi.org/10.1186/s40759-018-0038-4

[180] Ferry, J. D. (1980). *Viscoelastic properties of polymers* (3rd ed.). New York: John Wiley & Sons. https://scholar.google.com/scholar?&q=J.%20D.%20FerryViscoelastic%20Properties%20of%20Polymers%203rd%20ed.%2C%20John%20Wiley%20%26%20Sons%2C%201980

[181] Zhang, Y., Zhang, J., Ma, T., Qi, H., & Chen, C. (2023). Predicting asphalt mixture fatigue life via four-point bending tests based on viscoelastic continuum damage mechanics. *Case Studies in Construction Materials*, 19, e02671. https://doi.org/10.1016/j.cscm.2023.e02671

[182] Sadek, H., Sadeq, M., Masad, E., Al-Khalid, H., & Sirin, O. (2019). Probabilistic viscoelastic continuum damage analysis of fatigue life of warm-mix asphalt. *Journal of Transportation Engineering, Part B: Pavements*, 145(3), 04019024. https://doi.org/10.1061/JPEODX.0000128

[183] Klug, A., Ng, A., & Faxina, A. (2022). Application of the viscoelastic continuum damage theory to study the fatigue performance of asphalt mixtures—A literature review. *Sustainability*, 14(9), 4973. https://doi.org/10.3390/su14094973

[184] Al-Atroush, M. E., Marouf, A., Aloufi, M., Marouf, M., Sebaey, T. A., & Ibrahim, Y. E. (2022). Structural performance assessment of geothermal asphalt pavements: A comparative experimental study. *Sustainability*, 14(19), 12855. https://doi.org/10.3390/su141912855

[185] Ercisli, S. (2015). *Development of enhanced pavement deterioration curves* (Master's thesis). Virginia Polytechnic Institute and State University, Blacksburg, Virginia. http://hdl.handle.net/10919/56599

[186] Kocak, S., & Kutay, M. E. (2020). Fatigue performance assessment of recycled tire rubber modified asphalt mixtures using viscoelastic continuum damage analysis and AASHTOWare pavement ME design. *Construction and Building Materials*, 248, 118658. https://doi.org/10.1016/j.conbuildmat.2020.118658

[187] Li, H., Jiang, J., & Ni, F. (2020). Factors affecting maintenance probability and resurfacing thickness based on the pavement management system. *Advances in Civil Engineering*, 2020, 8817081. https://doi.org/10.1155/2020/8817081

[188] Federal Highway Administration (FHWA). (n.d.). *LTPP InfoPave*. https://infopave.fhwa.dot.gov

[189] Miller, J. S. and Bellinger, W. Y. (2003). *Distress identification manual for the long-term pavement performance program* (No. FHWA-RD-03-031). United States. Federal Highway Administration. Office of Infrastructure Research and Development. https://rosap.ntl.bts.gov/view/dot/40882

[190] Elkins, G. E. and Ostrom, B. (2021). *Long-term pavement performance information management system user guide* (No. FHWA-HRT-21-038). United States. Federal Highway Administration. Office of Infrastructure Research and Development. https://rosap.ntl.bts.gov/view/dot/55790

[191] Von Quintus, H. L. and Simpson, A. L. (2003). *Structural Factors for Flexible Pavements: Initial Evaluation of the SPS-1 Experiment Final Report* (No. FHWA-RD-01-166). United States. Federal Highway Administration. https://rosap.ntl.bts.gov/view/dot/41562

[192] Federal Highway Administration. (2003). *Key findings from LTPP analysis 2000–2003* (FHWA-HRT-04-032). U.S. Department of Transportation. https://www.fhwa.dot.gov/publications/research/infrastructure/pavements/ltpp/reports/04032/features.cfm

[193] FHWA. *Balanced Mix Design (BMD) Case Studies Virtual Workshop: Moving Forward with Implementation*. Online Workshop, 14–15 February 2022. https://www.fhwa.dot.gov/pavement/asphalt/pubs/20210722_bmd_workshop_flyer_508c_finalv3.pdf

[194] Akhter, A.A. and Goulias, D., 2024. Development of mix design approach for mixtures with reclaimed asphalt pavement, RAP, materials. *Sustainability*, 17(1), p.38. https://www.mdpi.com/2071-1050/17/1/38

[195] Hajj, E.Y. and Aschenbrener, T.B., 2021. Case studies on the implementation of balanced mix design and performance tests for asphalt mixtures: New Jersey Department of Transportation (NJDOT). *UNR Pavement Engineering & Science Program*. https://www.researchgate.net/publication/355130953

[196] Diefenderfer, S.D. and Bowers, B.F., 2019. Initial approach to performance (balanced) mix design: The Virginia experience. *Transportation Research Record*, 2673(2), pp.335–345. https://doi.org/10.1177/03611981188237

[197] Zhou, F., Steger, R. and Mogawer, W., 2021. Development of a coherent framework for balanced mix design and production quality control and quality acceptance. *Construction and Building Materials*, 287, p.123020. https://doi.org/10.1016/j.conbuildmat.2021.123020

[198] Faraway, J. J. (2004). *Linear Models with R*. 1st ed. New York: Chapman and Hall/CRC. https://doi.org/10.4324/9780203507278.